Energie & Umwelt
Energy & Environment

392

µc-SiC:H(n) for Silicon Heterojunction Solar Cells

Manuel Bernhard Pomaska

Member of the Helmholtz Association

JÜLICH FORSCHUNGSZENTRUM

Energie & Umwelt /
Energy & Environment
Band / Volume 392
ISBN 978-3-95806-267-2

JÜLICH
FORSCHUNGSZENTRUM

Microcrystalline Silicon Carbide for Silicon Heterojunction Solar Cells

Manuel Bernhard Pomaska

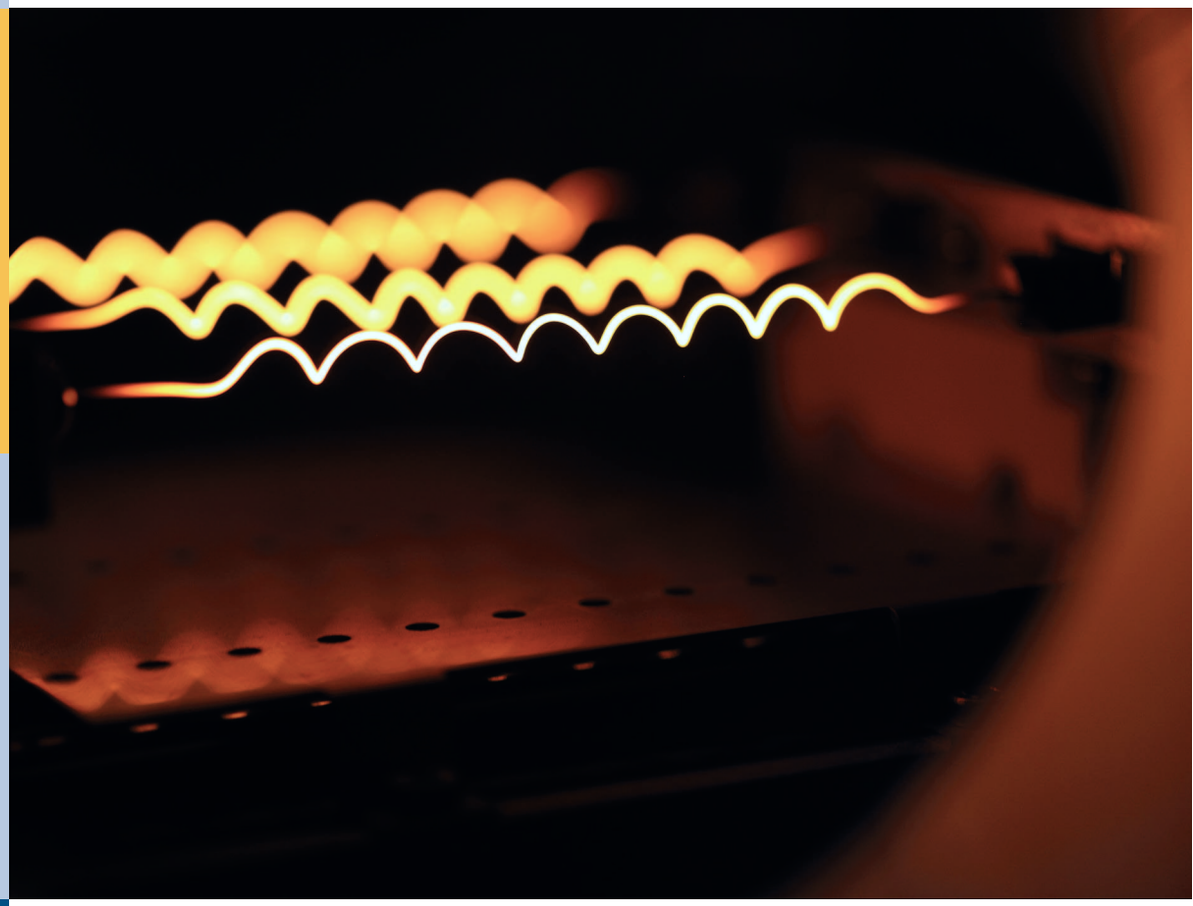

Energie & Umwelt /
Energy & Environment
Band / Volume 392
ISBN 978-3-95806-267-2

JÜLICH
FORSCHUNGSZENTRUM

Schriften des Forschungszentrums Jülich
Reihe Energie & Umwelt / Energy & Environment Band / Volume 392

Forschungszentrum Jülich GmbH
Institute of Energy and Climate Research
IEK-5 Photovoltaics

Microcrystalline Silicon Carbide for Silicon Heterojunction Solar Cells

Manuel Bernhard Pomaska

Schriften des Forschungszentrums Jülich
Reihe Energie & Umwelt / Energy & Environment Band / Volume 392

ISSN 1866-1793 ISBN 978-3-95806-267-2

Bibliographic information published by the Deutsche Nationalbibliothek.
The Deutsche Nationalbibliothek lists this publication in the Deutsche Nationalbibliografie; detailed bibliographic data are available in the Internet at http://dnb.d-nb.de.

Publisher and Distributor: Forschungszentrum Jülich GmbH
Zentralbibliothek
52425 Jülich
Tel: +49 2461 61-5368
Fax: +49 2461 61-6103
Email: zb-publikation@fz-juelich.de
www.fz-juelich.de/zb

Cover Design: Grafische Medien, Forschungszentrum Jülich GmbH

Printer: Grafische Medien, Forschungszentrum Jülich GmbH

Schriften des Forschungszentrums Jülich
Reihe Energie & Umwelt / Energy & Environment, Band / Volume 392

D 82 (Diss. RWTH Aachen University, 2017)

ISSN 1866-1793
ISBN 978-3-95806-267-2

The complete volume is freely available on the Internet on the Jülicher Open Access Server (JuSER) at www.fz-juelich.de/zb/openaccess.

Die einfachste Vorstellung ist die, daß ein Lichtquant seine ganze Energie an ein einziges Elektron abgibt; wir wollen annehmen, daß dies vorkomme. Es soll jedoch nicht ausgeschlossen sein, daß Elektronen die Energie von Lichtquanten nur teilweise aufnehmen. Ein im Innern des Körpers mit kinetischer Energie versehenes Elektron wird, wenn es die Oberfläche erreicht hat, einen Teil seiner kinetischen Energie eingebüßt haben. Außerdem wird anzunehmen sein, daß jedes Elektron beim Verlassen des Körpers eine (für den Körper charkteristische) Arbeit P zu leisten hat, wenn es den Körper verläßt. Mit der größten Normalgeschwindigkeit werden die unmittelbar an der Oberfläche normal zu dieser erregten Elektronen den Körper verlassen. Die kinetische Energie solcher Elektronen ist

$$\frac{R}{N}\beta\nu - P$$

Albert Einstein,
Annalen der Physik 17, 132 (1905)

Contents

Abstract

N-type microcrystalline silicon carbide (μc-SiC:H(n)) is a promising material for the doped layer on the illuminated side of silicon heterojunction (SHJ) solar cells, because it offers a combination of large bandgap for high optical transparency and suitable refractive index for low reflection. Moreover, both optical properties can be provided at sufficiently high electrical conductivity in order to minimize electrical resistance losses. However, two issues needed to be overcome for a successful implementation of μc-SiC:H(n) in SHJ solar cells. First, the opto-electrical properties of the μc-SiC:H(n) films were suffering from reproducibility problems in the past. A deeper understanding of the relation between microstructure, electrical conductivity and optical transparency was necessary. Second, it was still unclear, if the required growth conditions for the high quality μc-SiC:H(n) are compatible with maintaining high passivation quality of the silicon wafer surfaces. A high hydrogen dilution during the film growth is necessary to provide the promising opto-electrical properties, but the common passivation layers of intrinsic amorphous silicon suffer from severe deterioration due to hydrogen etching. A systematic adaptation of the μc-SiC:H(n) growth conditions and the development of a suitable passivation layer were missing so far.

The material properties and process parameters of μc-SiC:H(n) films were studied in detail in this thesis. The μc-SiC:H(n) films were grown by *hot wire chemical vapor deposition* (HWCVD) as well as by *plasma enhanced chemical vapor deposition* (PECVD). The relations of crystalline grain size in μc-SiC:H(n) with deposition rate, electrical conductivity, hydrogen content, carbon fraction, and optical absorption coefficient were investigated. The impact of oxygen and nitrogen doping on optical and electrical properties were investigated separately. In particular, their influence on

electrical conductivity, charge carrier density and mobility, as well as on grain size, hydrogen content, and optical absorption coefficient were studied in detail. The new insights into the effects of grain size, oxygen and nitrogen doping were used to propose a model for the electrical transport mechanisms in μc-SiC:H(n). Based on the deeper understanding of the material properties of HWCVD and PECVD grown μc-SiC:H(n), the electrical conductivity was improved to 10^1 S/cm which is the highest value reported so far for this type of material. In addition, the optical transparency of μc-SiC:H(n) was increased while maintaining a sufficiently high electrical conductivity. Thus, when μc-SiC:H(n) is used as doped layer on the illuminated side of SHJ solar cells, the photo-carrier generation rate can be increased.

The main focus in this thesis was on the implementation of highly transparent μc-SiC:H(n) without deteriorating the passivation layer of the SHJ solar cell. A first concept consisted of a PECVD grown intrinsic amorphous silicon oxide (a-SiO_x:H(i)) layer to passivate the silicon wafer surfaces where the a-SiO_x:H(i) layer was protected by an n-doped microcrystalline silicon oxide (μc-SiO_x:H(n)) layer against the hydrogen etching during the HWCVD growth of μc-SiC:H(n). However, the HWCVD growth conditions of μc-SiC:H(n) have a strong influence on the final passivation quality where the in-diffusion of hydrogen atoms from the gas phase can deteriorate the wafer surface passivation severely. Moreover, the crystalline volume fraction and the oxygen content of the μc-SiO_x:H(n) protection layer need to be adapted with respect to the HWCVD growth condition for the μc-SiC:H(n) layer. A maximum active area efficiency of 18.9 % was achieved with an open circuit voltage (V_{oc}) of 677 mV, a short circuit current density (J_{sc}) of 37.6 mA/cm^2, and a fillfactor (FF) of 74.2 %. A second concept consisted of an ultra-thin silicon dioxide (SiO_2) that passivated the wafer surfaces and which was grown wet-chemically. No additional protection layer was required, but also in this case the passivation quality strongly depends on the HWCVD conditions of the μc-SiC:H(n) growth. With μc-SiC:H(n) as window layer in two-side contacted SHJ solar cells a maximum active area efficiency of 17.6 % was achieved with V_{oc} of 665 mV, J_{sc} of 40.3 mA/cm^2, and FF of 65.8 %. For interdigitated back contact solar cell design the optical losses on the illuminated side were reduced to only 0.5 mA/cm^2 with the help of μc-SiC:H(n), which is an excellent result that can compete with the currently best single-junction,

non-concentrator SHJ solar cells.

Zusammenfassung

N-Typ mikrokristallines Siliziumkarbid (μc-SiC:H(n)) ist ein vielversprechendes Material um es als dotierte Schicht auf der beleuchteten Seite von Solarzellen mit Silizium-Heteroübergang (SHJ) zu verwenden. Es bietet eine Kombination aus breiter Bandlücke für eine hohe optische Transparenz und passendem Brechungsindex für eine geringe Reflektion. Darüber hinaus können beide optischen Eigenschaften bei einer ausreichend hohen elektrischen Leitfähigkeit verwendet werden, so dass Verluste durch elektrische Widerstände vermieden werden. Jedoch müssen zwei Herausforderungen überwunden werden, damit μc-SiC:H(n) erfolgreich in SHJ-Solarzellen eingesetzt werden kann. Einerseits litten die optoelektrischen Eigenschaften der Siliziumkarbidschichten in der Vergangenheit unter Reproduzierbarkeitsschwierigkeiten. Deshalb war es nötig das Wissen um die Zusammenhänge zwischen Mikrostruktur, elektrischen Leitfähigkeit und optischer Transparenz zu vertiefen. Andererseits war unklar, ob die notwendigen Abscheidebedingungen für das hoch qualitative μc-SiC:H(n) kompatibel mit dem Erhalt einer hohen Passivierqualität der Siliziumwaferoberflächen sind. Eine hohe Wasserstoffverdünnung während des Schichtwachstums ist nötig um die vielversprechenden optoelektrischen Eigenschaften anbieten zu können, aber zugleich erleiden konventionelle Passivierschichten aus intrinsischem amorphen Silizium starke Beschädigungen durch Wasserstoffätzungen. Eine systematische Anpassung der Wachstumsbedingungen von μc-SiC:H(n) und die Entwicklung einer geeigneten Passivierschicht fehlten bislang.

Die Materialeigenschaften und Prozessparameter der μc-SiC:H(n)-Schichten wurden detailliert in dieser Doktorarbeit erforscht. Die μc-SiC:H(n)-Schichten wurden mittels *hot wire chemical vapor deposition* (HWCVD) und auch mittels *plasma enhanced chemical vapor deposition* (PECVD) gewachsen. Die Zusammenhänge zwi-

schen kristalliner Korngröße im μc-SiC:H(n) und der Depositionsrate, der elektrischen Leitfähigkeit, dem Wasserstoffgehalt, dem Kohlenstoffanteil sowie dem optischen Absorptionskoeffizienten wurden untersucht. Der Einfluss von Sauerstoff- und Stickstoffdotierung auf die optischen und elektrischen Eigenschaften wurden getrennt untersucht. Insbesondere deren Einfluss auf die elektrische Leitfähigkeit, die Ladungsträgerdichte, die Ladungsträgermobilität, Wasserstoffgehalt und optischer Absorptionskoeffizient wurden tiefer studiert. Die neuen Erkenntnisse über den Effekt der Korngröße, Sauerstoff- und Stickstoffdotierung wurden verwendet um ein Model über den elektrischen Transport in μc-SiC:H(n) aufzustellen. Basierend auf dem tieferen Verständnis der Materialeigenschaften des HWCVD und PECVD gewachsenen μc-SiC:H(n) konnte die elektrische Leitfähigkeit auf 10^1 S/cm verbessert werden. Dies ist der höchste Leitfähigkeitswert, der je für dieses Material veröffentlicht wurde. Des Weiteren wurde die optische Transparenz des μc-SiC:H(n) erhöht, während eine ausreichend hohe elektrische Leitfähigkeit beibehalten werden konnte. Wenn also μc-SiC:H(n) als dotierte Schicht auf der beleuchteten Seite von SHJ-Solarzellen verwendet wird, kann die Generierungsrate der Photo-Ladungsträger gesteigert werden.

Der Schwerpunkt in dieser Doktorarbeit lag auf dem Einsatz eines hochtransparenten μc-SiC:H(n), ohne die Passivierschicht in der SHJ-Solarzelle zu beschädigen. In einem ersten Konzept wurden die Siliziumwaferoberflächen von einem mittels PECVD gewachsenen intrinsischen amorphen Siliziumoxid (a-SiO_x:H(i)) passiviert, welches durch ein n-dotiertes mikrokristallines Siliziumoxid (μc-SiO_x:H(n)) gegen Wasserstoffätzen während des HWCVD-Wachstums des μc-SiC:H(n) geschützt wird. Jedoch haben die HWCVD-Wachstumsbedingungen für das μc-SiC:H(n) trotzdem einen großen Einfluss auf die finale Passivierqualität der Waferoberfläche, da diese durch Eindiffusion von Wasserstoffatomen aus der Gasphase beschädigt werden kann. Zudem müssen der kristalline Volumenanteil sowie der Sauerstoffanteil in der μc-SiO_x:H(n) Schutzschicht an die HWCVD-Wachstumsbedingungen für das μc-SiC:H(n) angepasst werden. Ein maximaler Wirkungsgrad des aktiven Bereichs von 18.9 % wurde erreicht, wobei die offene Klemmspannung (V_{oc}) 677 mV, die Kurzschlussstromdichte (J_{sc}) 37.6 mA/cm^2 und der Füllfaktor (FF) 74.2 % betrugen. In einem zweiten Konzept wurden die Siliziumwaferoberflächen von einem ultra-dünnen

Siliziumdioxid (SiO_2) passiviert, welches nass-chemisch gewachsen wurde. Eine zusätzliche Schutzschicht war nicht nötig, aber auch in diesem Fall hängt die Passivierqualität stark von den HWCVD-Bedingungen für das μc-SiC:H(n)-Wachstum ab. Doppelseitig-kontaktierte SHJ-Solarzellen mit μc-SiC:H(n)/SiO_2-Schichtstapel auf der beleuchteten Seite erzielten im aktiven Bereich einen maximalen Wirkungsgrad von 17.6 %, wobei die V_{oc} 665 mV, die J_{sc} 40.3 mA/cm^2 und der FF 65.8 % betrugen. Für vollständig rückseitig-kontaktierte SHJ-Solarzellen konnten die optischen Verluste auf der beleuchteten Seite durch den Einsatz von μc-SiC:H(n) auf lediglich 0.5 mA/cm^2 reduziert werden. Dies stellt ein exzellentes Ergebnis dar, welches mit den momentan besten SHJ-Solarzellen konkurrieren kann.

1. Introduction

In the last years, sustainable electricity generation attracted an increasing attention from the public. Especially in Germany, the installed electrical capacity of renewable energy sources is growing exponentially [1] and has reached about 32 % of the annual electricity generation in 2016 [1]. According to the German Federal Ministry for Economic Affairs and Energy it is planned to reach a share of 40-45 % by 2025 [2], thus, it can be expected that the strong growth for installed electrical capacity from renewable sources will continue. An important part is contributed by photovoltaic (PV) electricity generation which covered about 7 % of Germany's electricity demand in 2016 [1] and should also grow further according to the plans of the Ministry.

Globally, PV electricity generation is currently a fast growing market where the compound annual growth rate was 42 % between 2000 and 2015 [1]. A large majority of the PV technology is currently based on crystalline silicon (c-Si) which accounted 93 % of the global PV production in 2015 [1]. The first c-Si solar cell was already developed in 1954 [3]. In parallel, c-Si was intensively studied for the computer chip industry. Thus, c-Si solar cells have a large technological advance compared to more recent solar cell developments. The learning curve of the PV module price followed Moore's law and showed an average decrease of 23 % each time the cumulative production was doubled during the last 35 years [1]. As a result, the average price for PV rooftop systems in Germany decreased by 13 % per year and by 75 % in total from 2006 to 2016 [1]. The average system price reached a value of 1250 €/kW_p in 2016 [1]. A more detailed view on the data from Ref. [1] shows that the strong decrease in system price was meanly driven by a strong decrease in average price for PV modules. The PV module price decreased by around 80 % from 2006 to 2016

and the percentage of the total cost decreased from 71 % in 2006 to 47 % in 2016. Nevertheless, the system price per kW_p and the PV module price stagnate since 2013 [1]. The PV module price per kW_p consist of production cost and of electrical power output. To decrease the system price per kW_p by further reducing the PV module production costs has limited impact at the moment, because the production process chain is already well optimized for the currently used c-Si solar cell type. Therefore, it is more important to optimize the solar energy conversion efficiency of the c-Si solar cell to increase the electrical power output per solar cell so that the PV module price per kW_p is reduced in future.

Shockley and Queisser calculated in 1961 the maximum theoretical efficiency of an ideal solar cell using a single pn-junction [4] under non-concentrated sun light. According to their calculations the maximum solar conversion efficiency is around 32-33 % for a bandgap of 1.1-1.4 eV. With 1.1 eV c-Si has a favorable bandgap for high solar energy conversion efficiency. Although there exist materials, e.g., GaAs, that are more favorable for high solar energy conversion efficiency, due to a higher absorption coefficient, none of these materials is as abundant on Earth and is as industrially well known as c-Si.

Due to high c-Si wafer prices in the past, a second type of Si solar cells, namely the Si thin film technology, was developed as low cost alternative. It is based on amorphous Si (a-Si:H) thin films. Lower process temperatures and shorter process times for the solar cell production lead to lower production costs as compared to the c-Si technology [5]. Meanwhile, the costs of c-Si wafers have fallen drastically from 96 \$/W in the mid-1970s to 0.68 \$/W in 2016 [6] and a third type of Si based solar cells arose. This third type is called silicon heterojunction (SHJ) solar cell. It combines c-Si wafer and Si thin films from the first and the second Si technology. The SHJ solar cells combine the best of both technologies: high solar energy conversion efficiency and low costs. In 2016 SHJ solar cells reached a maximum solar energy conversion efficiency of 26.3 % on lab scale [7] and 24.4 % on module scale [7] which were the highest efficiencies for non-concentrator, single-junction Si based solar cells.

The SHJ solar cell consists of a doped c-Si wafer with passivated surfaces, e.g., by intrinsic a-Si:H, and doped thin films that form the pn-junction on one side and an electrical surface field on the other. Transparent conductive oxide layers are required to enhance the charge carrier transport to the contacts because the lateral conductivity of the doped thin film layers is low. On the illuminated side of the SHJ solar cell the sun light needs to pass through several layers before it is absorbed in the c-Si. In this thesis, the doped layer on the front side of the SHJ solar cell is in the scope of the investigation. Beside forming the pn-junction or the electrical surface field, absorption and reflection of the sun light that are caused by the doped layer need to be minimized. N-type microcrystalline silicon carbide (μc-SiC:H(n)) is a promising material for the doped layer that offers a combination of large bandgap for high optical transparency and suitable refractive index for low reflection. Moreover, both optical properties can be provided at sufficiently high electrical conductivity in order to minimize electrical resistance losses.

However, two issues need to be overcome for a successful implementation of μc-SiC:H(n) in SHJ solar cells. First, the opto-electrical properties of the μc-SiC:H(n) films suffered from reproducibility problems in the past [8, 9], which demonstrates that the study of the material is still incomplete and needs to be proceeded. Second, it is still unclear, if the required growth conditions of μc-SiC:H(n) are compatible with high passivation quality of the c-Si surfaces. A high hydrogen dilution during the film growth is necessary to provide the promising opto-electrical properties, but the common passivation layers, e.g., a-Si:H, suffer from severe deterioration due to hydrogen etching. Only few references (e.g., [10–12]) exist that report on first tentative attempts to implement μc-SiC:H(n) in SHJ solar cells. A systematic adaptation of the μc-SiC:H(n) growth conditions or a systematic development of a suitable passivation layer are missing so far.

This thesis contains six chapters. In Chapter 2, basic aspects of SHJ solar cells are reviewed and an overview on the μc-SiC:H(n) material is given based on the current status in literature. The chapter is divided into four sections. In Section 2.1, an introduction into the general working principles of photovoltaic solar cell devices is provided and the different types of c-Si based solar cell are presented. In

Section 2.2, different passivation methods are described. In Section 2.3, different doped layer materials and front side designs are presented. In the Section 2.4, the μc-SiC:H(n) material is introduced in more detail based on the current knowledge from literature.

In Chapter 3, all details of sample preparation and characterization methods are described. In Section 3.1, parameters of the μc-SiC:H(n) deposition are listed. The films were produced by Hot-wire chemical vapor deposition (HWCVD) and plasma-enhanced chemical vapor deposition (PECVD). In Section 3.2 details about the Si wafers and their pre-treatments are provided. Further, the process details are described for intrinsic amorphous silicon oxide, silicon dioxide, indium tin oxide, silicon nitride, and magnesium fluoride films. In Section 3.3, details of the structural characterizations of μc-SiC:H(n) are addressed. In Section 3.4, the characterization techniques of the opto-electronic properties of μc-SiC:H(n) are described. In Section 3.5, information about characterization methods of Si wafer surface passivation and solar cell performance are given.

In Chapter 4, the μc-SiC:H(n) material is described. The relation between structural, electrical, and optical properties is investigated in detail. Further, HWCVD and PECVD grown μc-SiC:H(n) materials are compared. In Section 4.1, the effect of the grain size in unintentionally doped μc-SiC:H(n) is related to deposition rate, electrical conductivity, hydrogen content, grain size, carbon fraction, and optical absorption coefficient. In Section 4.2, the role of oxygen and nitrogen on optical and electrical properties is investigated separately. In particular, their influence on electrical conductivity, charge carrier density and mobility, as well as on grain size, hydrogen content, and optical absorption coefficient are studied in detail. Finally, the insights of both sections are used to propose a model for the electrical transport mechanisms in μc-SiC:H(n).

In Chapter 5, the feasibility and the potential of implementing μc-SiC:H(n) in SHJ solar cells are discussed. In Section 5.1, intrinsic amorphous silicon oxides (a-SiO_x:H(i)) were used to passivate the c-Si surfaces of the tested structures, whereas in Section 5.2, the surfaces were passivated by ultra-thin wet-chemically grown silicon

dioxide (SiO_2). In both sections, the influence of the HWCVD deposition parameters on the passivation quality and on the SHJ solar cell performance with μc-SiC:H(n) doped layer are analyzed.

In Chapter 6, the main conclusions of this thesis are summarized and a outlook for future works is provided.

2. Fundamentals

This chapter provides fundamental information on SHJ solar cells and on window layer materials. In Sec. 2.1, general photovoltaic working principles are introduced and the different concepts of c-Si based solar cells are described. In Sec. 2.2, different c-Si surface passivation mechanisms are introduced. In Sec. 2.3, the requirements for a doped window layer are presented. In Sec. 2.4, this chapter is completed by a literature review of HWCVD and PECVD grown μc-SiC:H(n) material.

2.1. Working principles of solar cells

The most fundamental working principle of a photovoltaic device is based on the photoelectric effect which was discovered in 1905 by A. Einstein [13] who was awarded by the Nobel Prize in Physics 1921 [14] for this discovery. The effect describes theoretically that it is possible to excite electrons in a material by shining light on the material: Photons with a certain photon energy are absorbed and transfer their photon energy to electrons which are then excited to a higher energy state. The discreet energy difference between excited state and initial state corresponds to the energy of the absorbed photon.

In semiconductors the energy states form energy bands [15]. At zero Kelvin, electrons are all bound to their atoms in their lowest energy states: they stay in the so called valence band. In a defect-free semiconductor the nearest excited states form the so called conduction band which is empty at zero Kelvin. The energy difference between the bottom of the conduction band (E_{C}) and the top of the valence band (E_{V}) is called bandgap energy (E_{g}). It is the minimum energy that is necessary to excite an electron in a defect-free semiconductor. One possibility to excite electrons

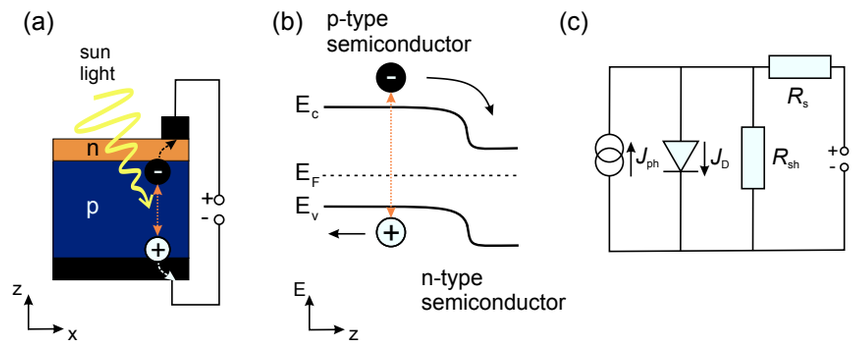

Figure 2.1.: *Working principle of photovoltaic solar cell from different points of view: (a) cross-section of illuminated device, (b) energy band diagram of pn-junction, and (c) equivalent electrical circuit*

to the conduction band is by photon absorption. In the valence band the absence of electrons leaves holes, so that always an electron-hole pair is created. Both are then called photogenerated charge carrier. More details of semiconductor physics may be found in Ref. [15].

The value of E_g for c-Si is 1.1 eV. A photon energy of 1.1 eV and higher corresponds to wavelengths (λ) of 1240 nm and lower, as the photon energy depends on the wavelength by de Broglie's equation

$$E = \frac{\mathrm{hc}}{\lambda} = \mathrm{h}\nu, \tag{2.1}$$

where h is the Planck's constant, c is the speed of light, and ν is the wavenumber. The photon flux of the sun light that arrives at the surface of Earth is highest for photons with an energy of about 2 eV which corresponds to a λ of 632 nm. Thus, the majority of the energy of the sun light that arrives on Earth can be absorbed by c-Si which excites electrons from the valence band into the conduction band. More detailed information about the sun spectrum can be found in Ref. [16].

The transfer of energy from photons to electrons is however not enough to form a power generating photovoltaic solar cell, because the energy needs to be harvested

before the photogenerated charge carriers relax back to their ground state, i.e., electrons tend to relax to the valence which then reduces the number of holes. This relaxation process is called recombination of the charge carriers. Thus, every excited charge carrier has a limited lifetime (τ_{eff}) before the gained energy is dissipated. To make use of the absorbed energy by supplying it to an external electric circuit it is necessary to extract excess electrons and excess holes through their respective contacts before they recombines. Carrier-selective contacts should be implemented for an effective extraction. According to Würfel et al. [17] the selectivity is achieved by differences in the conductivities of electrons and holes in two distinct regions of the device, which, for one charge carrier, allows transport to one contact and block transport to the other contact.

The pn-junction and the surface field (back or front) are the selective contacts in a solar cell device. For a c-Si based solar cell, the pn-junction extracts the minority excess charge carriers and the surface field extracts the majority excess charge carriers. In Fig. 2.1(a) a cross-section of an illuminated pn-junction illustrates the charge separation. In Fig. 2.1(b) the energy band diagram of the pn-junction is presented.

From electrical point of view, the pn-junction in the dark can be represented by a diode which is expanded by a photogenerator if the pn-junction is illuminated. This combination represents the ideal case, where electrical resistances are neglected. The total electrical current density (J) in the ideal case can be expressed by the superposition of diode current density (J_{D}) and photo current density (J_{ph}) as a function of the voltage (V)

$$J(V) = J_0(e^{\frac{\mathrm{q}V}{\mathrm{k_B}T}} - 1) - J_{\mathrm{ph}}, \tag{2.2}$$

where J_0 is the saturation current density, q the elementary charge, $\mathrm{k_B}$ the Boltzmann constant, and T the temperature. In the real case, bulk and contact resistances as well as shunts also play an important role for the functioning of the solar cell device. Bulk and contact resistances can be summarized as series resistance (R_{s}) and the shunts can be represented as shunt resistance (R_{sh}), so that the current density

can be expressed as

$$J(V) = J_0(e^{\frac{q(V-R_s J)}{k_B T}} - 1) + \frac{V - R_s J}{R_{sh}} - J_{ph}. \tag{2.3}$$

The equivalent electrical circuit is shown in Fig. 2.1(c). The expression in Eq. 2.3 can be extended by further corrections, in order to describe the real case even more exactly. The additional corrections may be found in Ref. [18]. For this thesis, however, it is sufficient to consider only Eq. 2.3.

With an illuminated solar cell, electrical power can be generated which is maximum (P_{max}) where the product of V and J is highest. Therefore, the solar energy conversion efficiency (η) can be written as

$$\eta = \frac{P_{max}}{P_{sun}}, \tag{2.4}$$

where P_{sun} denotes the incoming power from sun light. Under standard test conditions with AM1.5g sun spectrum [19] (global spectrum at the Earth's surface, including direct and diffuse radiation) the maximum P_{sun} is 100 W/cm^2. The theoretical limit of η for a non-concentrated single junction solar was derived by Shokley and Queisser to be around 33 % [4].

To study the performance of an illuminated solar cell device in detail, three characteristic values are derived from the measured current-voltage curve. First is the short circuit current density (J_{sc}) which is the current density at $V = 0$. Second is the open circuit voltage (V_{oc}) which is the voltage where $J = 0$. Third is the fill factor (FF) which is defined by $FF = P_{max}/(J_{sc}V_{oc})$. The η from Eq. 2.4 can be reformulated as

$$\eta = \frac{J_{sc}V_{oc}FF}{P_{sun}}. \tag{2.5}$$

In a simplified picture, it is possible to attribute the three parameters to three different loss effects that limit the device performance of a c-Si based solar cell:

- J_{sc} depends on optical losses that hinder the light to be fully absorbed in the c-Si absorber and on the collection efficiency of the photogenerated charge carriers.

- V_{oc} is fundamentally determined by recombination of photogenerated electrons and holes - the lower the effective recombination rate the higher is V_{oc}. More limits of V_{oc} are discussed in Ref. [20].
- As the FF is determined at P_{max}, electrical losses from high R_s or low R_{sh} decrease the FF significantly. The mathematical expressions describing the FF can be found in Ref. [20].

2.2. Passivated contacts

The photo-electric effect is reversible and recombination of the different charge carriers may occur in the inverse process. Three main types of recombination co-exist. One is the radiative recombination or band-to-band recombination, where electrons relax back to their ground state, i.e, valence band for c-Si based solar cells, by emitting a photon with the excess energy. With silicon being an indirect semiconductor, band-to-band recombination of an charge carriers is with low probability. Non-radiative recombination processes are far more probable with c-Si, which can occur in form of so called Shockley-Read-Hall defect recombination and Auger recombination. Defects arise from crystallographic defects incorporated in the c-Si bulk or from defects at the c-Si surface. Crystallographic defects in the bulk are nowadays well controlled, but defects at the c-Si surface are unavoidable. They can be passivated in several ways which will be introduced in more detail in the following. The defects essentially introduce energy states within the bandgap, which provide a low-energy pathway for electrons and holes to recombine. The recombination rates at the c-Si wafer surfaces are much higher than in the bulk, thus the effective carrier lifetime is limited by the recombination at the surfaces and recombination in the bulk can be neglected. In the case of Auger recombination, the excess energy of the photogenerated charge carriers is transferred to a second charge carrier which then dissipates its excess energy incrementally by phonon emission. However, Auger recombination becomes only important at high concentration of charge carriers. Detailed information about the three types of recombination may be found in Ref. [21].

At the c-Si wafer surfaces high defect densities (D_{it}), forming unoccupied energy states within the energy bandgap, lead to high recombination probabilities. The high D_{it} arises from open Si bonds which either form unsaturated dangling bonds or reconstruct to Si-Si bonds. In order to decrease the recombination probability, either *chemical passivation* of the defects or/and an electrical field can be applied. In the case of chemical passivation, the Si dangling bonds are saturated by other atoms, e.g., hydrogen or oxygen, so that the number of unoccupied energy states within the energy bandgap is significantly reduced at the c-Si surface. In the case of applying an electric field at the c-Si surface, the electrons and holes are separated by the electrical force of the field which, in other words, is the carrier-selective contact. The reduction of the amount of one type of charge carrier near the defects states reduces the recombination probability due to missing recombination counter partners. Moreover, one type of charge carrier is accelerated towards the interface by the electric field while the other is repelled. The residence time of the charge carriers near the defects is reduced, thus the recombination probability is further reduced. For this reason, the second approach is named *field effect passivation*. The combination of field and passivation makes the interface a passivated contact. It should be noted that a passivated contact is always a carrier-selective contact, but not all carrier-selective contacts are passivated contacts.

In Fig. 2.2 three key passivation concepts for different c-Si based solar cell types are presented that have been developed over the last decades. The first case is the homojunction case. The term homojunction describes a pn-junction which is built by only one semiconductor material, only one E_{g}, and consequently without any band offset. In Fig. 2.2(a) a n^+ emitter is, e.g., diffused into a p-doped c-Si wafer that the pn-junction is located inside the c-Si which can be considered as field effect passivation. Consequently, an important part of the photogenerated charge carriers are separated before they reach the defect rich c-Si surfaces so that the recombination probability is significantly reduced. To reduce the recombination probability further for the homojunction case, the defects at the c-Si surface are passivated by an oxide or by a hydrogenated silicon nitride film, in order to terminate the open silicon bonds by oxygen (O) or hydrogen (H) atoms, which can be referred as chemical passivation. In addition, these passivation layers incorporate fixed charges that improve the field

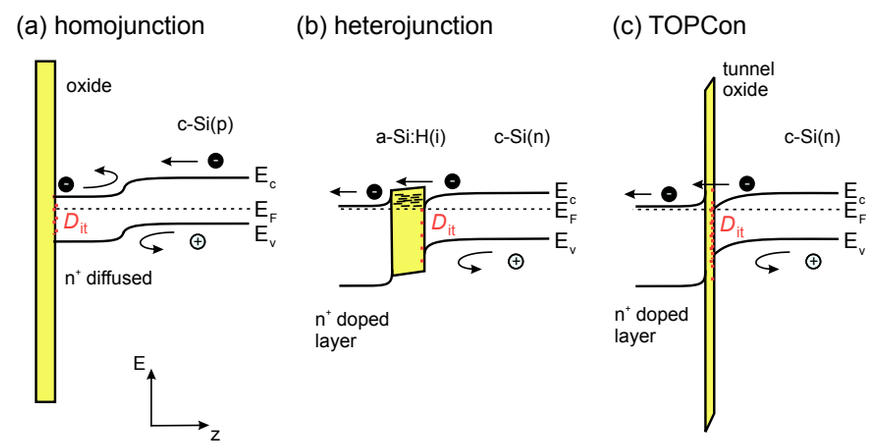

Figure 2.2.: *Three key concepts of c-Si surface passivation for (a) homojunction with passivated surface, (b) classical heterojunction, and (c) TOPCon (tunnel oxide passivated contact). The passivation layers are highlighted in yellow. Schematic is not to scale.*

effect passivation at the interface by induced band bending [22]. More detailed information about the passivation in the case of homojunction may be found in Ref. [23–25]. The described passivation concept for c-Si homojunctions, which is based on the combination of chemical and field effect passivation, is illustrated in form of energy band diagram in Fig. 2.2(a) and in form of cross section of the solar cell device in Fig. 2.3(a). The passivation quality can be improved by annealing [26] and by H treatment, e.g., forming gas anneal (FGA) [26]. The simple annealing enables the O or H atoms to distribute more effectively over the unsaturated Si dangling bonds. The H treatment introduces more H atoms to the interface to passivate the defects [26–28]. As silicon oxide and silicon nitride have very low electrical conductivity, the passivation layers are removed locally to implement local contacts where the electrical current is then collected. This cell type is known as PERL (passivated emitter, rear locally diffused) and is presented in Fig. 2.3(b). Zhao et al. demonstrated a maximum η of 25.0 % [29, 30] with a PERL cell.

The second case is the heterojunction case. The term heterojunction describes a pn-junction which is built by two semiconductor materials and two E_g which results

in bandoffsets and band discontinuities. Higher values of η than with homojunction c-Si solar cells were achieved with two-side contacted silicon heterojunction (SHJ) solar cells (25.1 % [31]). The pn-junction is formed by doped c-Si and a doped thin silicon based film. Thus, the pn-junction is located at the defect rich c-Si surface so that the passivation of the defects is of particular importance. Classical SHJ solar cells are typically passivated by intrinsic hydrogenated amorphous silicon (a-Si:H(i)) films as shown in Fig. 2.2(b). In this case, Si-H and Si-Si bonds are formed to passivate the Si dangling bonds which leads to a reduction of the D_{it} [28] down to around 10^9 $\mathrm{eV}^{-1}\mathrm{cm}^{-2}$. In comparison the D_{it} with silicon nitride is about 1 order of magnitude higher, which underlines the excellent passivation ability of a-Si:H(i). It is possible to increase the passivation quality by post-deposition annealing [28] and H treatment [26–28]. Finally, combining this type of chemical passivation with field effect passivation, by adding a thin doped Si layer, it is possible to achieve an excellent surface passivation quality. In Ref. [32] the optimization of the surface passivation quality leads to a V_{oc} value of up to 750 mV and corresponding η of 24.7 %. A schematic illustration of the stated solar cell can be found in Fig. 2.3(d).

A third possibility to realize a passivated c-Si interface for a solar cell device is a combination of the two first concepts, by using an ultra-thin oxide layer for chemical passivation of the c-Si surface and a thin n-doped poly-silicon layer to span an electrical field as illustrated in Fig. 2.2(c). As the oxide layer is highly insulating, its thickness is kept below 2 nm so that the charge carriers can tunnel through the oxide. Thus, this third concept is most commonly known as tunnel oxide passivated contact (TOPCon) [33], although the real mechanism is not clearly verified at the moment. The solar cell structure is illustrated in Fig. 2.3(e). Due to a bandgap of poly-silicon which is comparable to the bandgap of c-Si, the TOPCon is used at the non-illumanted side of the solar cell. The front side design consists structure of a typical homojunction c-Si based solar cell. However, TOPCon is classified into SHJ, due to the heterojunction around the tunnel oxide. So far, the interface structure needs to be annealed at around 850 °C in a nitrogen atmosphere [33–36] with a subsequent FGA treatment at around 450 [34–36], in order offer a high degree of passivation. The annealing step transforms the a-Si:H(n) capping layer film into n-typre polycrystalline Si (pc-Si:H(n)) with an increased charge carrier

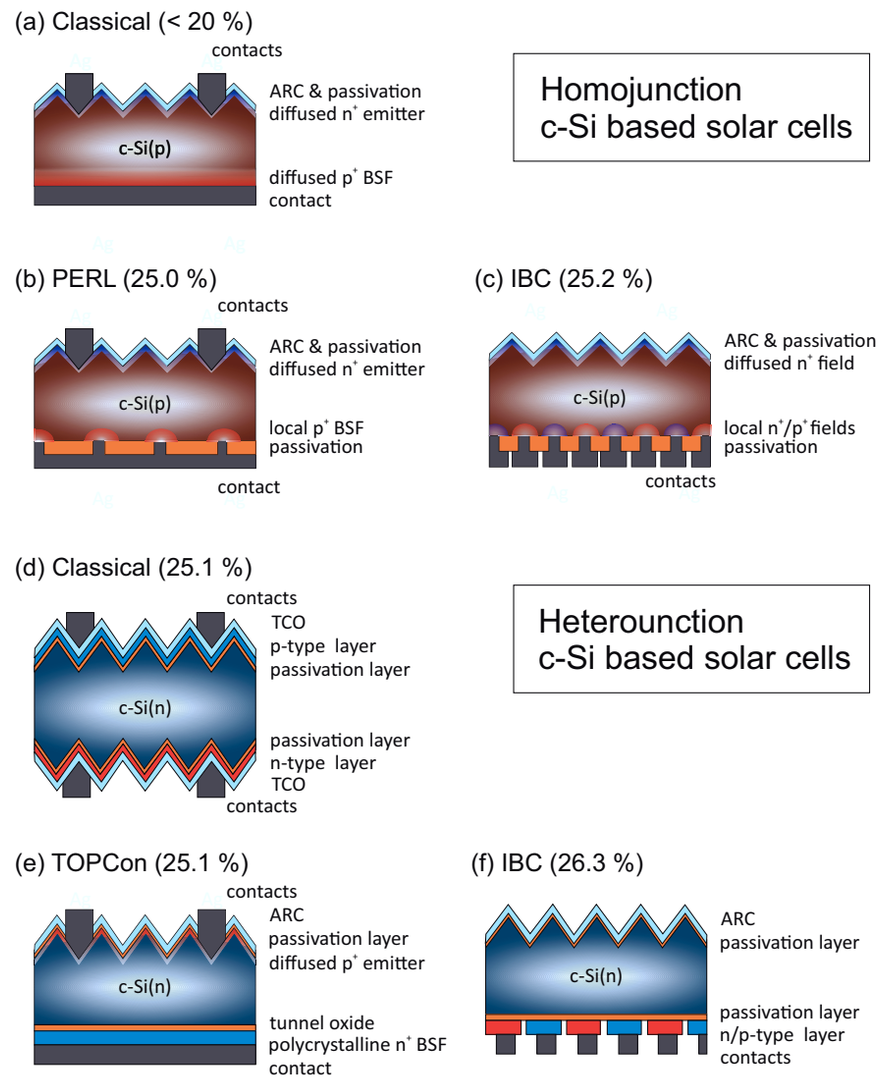

Figure 2.3.: *Various c-Si based solar cell concepts and their current record solar energy conversion efficiencies: (a-c) homojunction and (d-f) heterojunction solar cells.*

density [35], but also leads to a diffusion of the phosphorus doping atoms into the c-Si [37–40]. The increased charge carrier density in the doped layer together with the highly n-doped c-Si surface, caused by the in-diffused phosphorous atoms, induce a strong band bending around tunnel oxide [40, 41] that leads to stronger field effect passivation. The energy band diagrams for TOPCon are illustrated in Fig. 2.2(c). The subsequent FGA treatment improves the chemical passivation by an in-diffusion of H atoms that saturate the unsaturated Si dangling bonds [26–28]. Currently, TOPCon solar cells on lab scale reached η of up to 25.1 % [42] and V_{oc} of 718 mV.

Although it is possible to achieve high solar energy conversion efficiencies with c-Si based solar cells that are contacted on both sides, the current record efficiencies are achieved by placing all contacts on the non-illuminated back side. This contact concept is called interdigitated back contact (IBC) and avoids shadow losses on the front side that would limit the J_{sc}. The full solar cell stacks for homojunction and for heterojunction solar cells are illustrated in Fig. 2.3(c) and in Fig. 2.3(f), respectively. In 2016, a maximum η of 25.2 % [43] was achieved for c-Si homojunction by SunPower Corporation and a maximum η of 26.3 % [7] was achieved for c-Si heterojunction by Kaneka. Generally, such high efficiencies are only possible if recombination losses as well as optical losses are kept to a minimum.

2.3. Window layer materials for SHJ solar cells

To reduce optical losses in SHJ solar cells several aspects of the front side design, summarized in Fig. 2.4, have to be taken into account. Contacts are needed to collect the generated electrical current, but simultaneously they reduce the illuminated area of the c-Si absorber. As introduced in Sec. 2.2, it would be ideal to place all contacts on the back side of the solar cell (IBC) to avoid shadowing losses. Whatever contact concept is chosen - two-side contacted or IBC - the front side design always plays an important role. It consists of so called *window layers* that need to fulfill several requirements. First, the window layer has to be sufficiently transparent for the incoming sun light so that it is not parasitically absorbed in the window layer, but in the c-Si. Thus, window layers need large E_{g}. Secondly, a high lateral conductivity

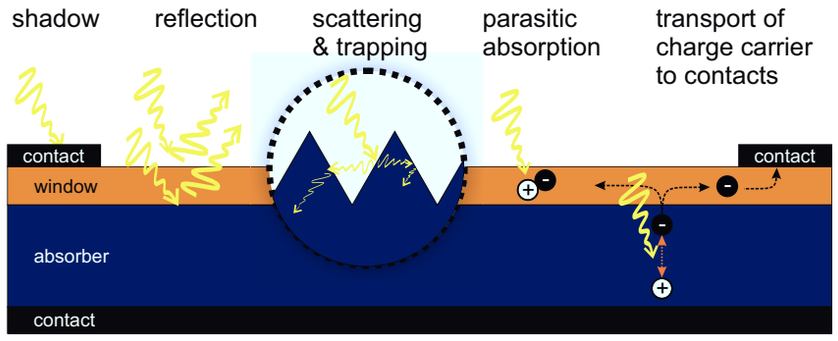

Figure 2.4.: *Aspects of front side design of a solar cell device that increase or decrease the short circuit current density.*

(σ) is also required, in order to transport the separated charge carriers to the front contacts. Lastly, window layers should also avoid reflection losses by being part of an anti-reflection coating (ARC) structure.

The reflectivity (R) for normal incident light at the interface of two materials is given by

$$R = \left(\frac{n_{\mathrm{j}} - n_{\mathrm{j+1}}}{n_{\mathrm{j}} + n_{\mathrm{j+1}}}\right)^2, \tag{2.6}$$

where n_{j} and $n_{\mathrm{j+1}}$ are the refractive indices of the two materials. The refractive index is in the range of 3.6-6.9 [44] for c-Si and it is 1 for air, which leads to a reflectivity of 32-56 % at the air/c-Si interface. ARC is needed to reduce the reflectivity. The window layers should exhibit a refractive index between 1.0 and 3.6 so that through an index grading the total reflection is reduced.

The term window layer applies to all layers at the illuminated side of the absorber and can refer to the doped layer on the illuminated side as well as to a transparent conductive oxide (TCO) which is placed at the top of the doped layer. Currently, typical two-side contacted SHJ solar cells consist of a combination of a doped a-Si:H layer to form the pn-junction and a transparent conductive oxide (TCO), e.g., indium tin oxide (ITO), which provides a sufficiently high conductance to transport the charge carriers to the front contacts, since the underlying doped a-Si:H layers

material	E_g [eV]	n_j [-]	σ [S/cm]	grown by
ITO	3.0 - 3.4 [45]	2.0 - 2.5 [45]	10^4 - 10^5 [46]	PVD
a-Si:H(n)	1.5 - 1.7 [47]	3.6 - 4.9 [45]	10^{-2} - 10^{-12} [48]	PECVD
a-Si:H(p)	1.5 - 1.7 [45]	3.5 - 4.8 [45]	10^{-2} - 10^{-12} [48]	PECVD
μc-SiO$_x$:H(n)	1.8 - 2.7 [49–51]	2.0 - 3.7 [51]	10^1 - 10^{-12} [49, 50]	PECVD
μc-SiO$_x$:H(p)	1.8 - 2.8 [51–53]	2.0 - 4.0 [51–53]	10^1 - 10^{-12} [51–54]	PECVD
μc-SiC:H(n)	$\approx$ 3.0 [12, 55]	1.9 - 3.4 [56, 57]	10^{-3} - 10^{-9} [12, 55]	PECVD
μc-SiC:H(p)	2.2 - 2.9 [58–60]	2.5 - 3.0 [60]	10^{-5} - 10^{-8} [60]	PECVD
μc-SiC:H(n)	2.5 - 3.4 [8, 61]	1.8 - 2.5 [62, 63]	10^0 - 10^{-7} [8, 61]	HWCVD
μc-SiC:H(p)	2.0 - 2.8 [8, 61]	-	10^{-1} - 10^{-5} [8, 61]	HWCVD
c-Si	1.1	3.6 - 6.9 [44]	10^{-1}	Cz

Table 2.1.: *Opto-electrical properties of Si alloys, ITO, and c-Si: optical bandgap E_g, refractive index n_j, and lateral electrical conductivity σ. The order of the σ values corresponds to the order or the E_g values. The n_j values are not correlated. The materials were produced by physical vapor deposition (PVD), plasma enhanced chemical vapor deposition (PECVD), hot wire chemical vapor deposition (HWCVD), and Czochralski (Cz) method.*

do not provide sufficient lateral conductivity. N- and p-doped a-Si:H have an E_g of only 1.5 - 1.9 eV which leads to significant parasitic absorption. The refractive index is in the range of 3.5 - 4.9 which is not suitable for index grading and hence does not reduce the reflection loss. In the following of this work the term window layer refers to the doped layer at the illuminated side of a solar cell. In order to decrease parasitic absorption and reflection losses in a two-side contacted SHJ solar cell, it is desired to develop and implement an optically more suitable material as window layer. In Table 2.1, the opto-electrical properties of the most prominent alternative window layer materials are listed together with the properties of doped a-Si:H as well as ITO.

The most prominent alternative window layers are silicon alloys, e.g., microcrystalline silicon oxide (μc-SiO$_x$:H) and microcrystalline silicon carbide (μc-SiC:H). Both materials provide larger E_g that are beneficial for reducing parasitic absorp-

tion in the doped layer. The E_g is in the range of 1.8 - 2.8 eV [49–53] for n- and p-doped μc-SiO$_x$:H. The E_g is in the range of 2.0 - 3.4 eV [8, 58–63] for n- and p-doped μc-SiC:H which is in the range range of the E_g of ITO (3.0 - 3.4 eV [45]). Most of the time, there is a trade-off for these materials between large E_g and large σ, because both parameters are not decoupled. Lambertz et al. postulated that a minimum σ of 10^{-6} S/cm for the doped layers is required to obtain reasonably low series resistance in silicon based solar cells. Based on this minimum σ, the upper E_g limit reported in literature for n- and p-doped μc-SiO$_x$:H is around 2.6 eV [51]. It is around 2.7 eV for μc-SiC:H(p) [61] and around 3.3 eV for μc-SiC:H(n) [61]. Based on these values of E_g, μc-SiC:H(n) is most promising to lower parasitic absorption in the doped layer on the front side of the SHJ solar cell. Additionally, the refractive index is suitable for index grading which offers the possibility to simultaneously reduce the reflection. Hence, μc-SiC:H(n) fulfills best all the opto-electrical requirements for an ideal window layer material in a SHJ solar cell.

2.4. Microcrystalline silicon carbide

The μc-SiC:H material consists of crystalline silicon carbide grains with a size in the micrometer range. Its development started only two decades ago while the development of mono-crystalline silicon carbide (c-SiC) started already at the end of the 19th century, when Acheson proposed and patented a method for industrial production of c-SiC [64]. Nowadays, c-SiC is a well known semiconductor which is used in high voltage electronic devices. Its indirect band structure offers a wide bandgap of 2.2-2.4 eV [65–68].

Crystalline SiC may have a variety of more than 140 reported crystalline modifications which have different material properties [69]. These crystalline modifications are known as polytypes. The most widespread polytypes are cubic (C) and hexagonal (H). More details concerning the material properties of different c-SiC polytypes can be found in Ref. [70, 71]. Wide bandgap μc-SiC:H films have been successfully prepared either by hot wire chemical vapor deposition (HWCVD) [8, 61, 72] or plasma enhanced chemical vapor deposition (PECVD) [12, 60, 73]. Hexagonal and

cubic polytypes are present in μc-SiC:H films [73, 74].

Lebedev [75] reports that nitrogen, phosphorus, and oxygen are well-known dopants for n-type doping of c-SiC. Aluminum, boron, and gallium are well-known acceptors [75] for p-type doping of c-SiC. The doping of μc-SiC:H is very similar to the doping of c-SiC. Nitrogen and phosphorus are the most popular donors for μc-SiC:H [8, 76–78]. For p-type doping of μc-SiC:H aluminum is well known [8, 79, 80]. Interestingly without using any doping gas, μc-SiC:H films show electrical characteristics of a n-type semiconductor [8, 9, 81]. Therefore, these films are often called to be *unintentionally n-doped* (sometimes also undoped). This phenomenon is the matter of ongoing research. According to Lebedev [75] the same phenomenon also exists for c-SiC. He stated in Ref. [75] that the unintentionally n-type conductivity can be explained by uncontrolled doping by nitrogen due to its high solubility in c-SiC ($\approx 10^{21}$ cm^{-3}). Moreover, nitrogen has the lowest ionization energy with 50-100 meV of all donor levels so that there is a high probability for the electrons to be part of electrical conductivity. Miyajima et al. come to a different conclusion for μc-SiC:H films in Ref. [8]. By referring to unintentional doping in microcrystalline silicon (μc-Si:H) [82], where oxygen located at the grain boundaries is considered as donor, Miyajima et al. assume that the large amount of oxygen found in their samples could be the donor for the n-type conductivity of μc-SiC:H. Finger et al. tried to clarify the above mentioned assumptions in Ref. [9], but they did not find a consistent indication that either oxygen or nitrogen atoms might be exclusively responsible for the unintentional n-doping. Both impurity concentrations were found to be on a high level compared e.g., with a-Si:H or μc-Si:H material prepared under similar conditions. The suggestion that oxygen and nitrogen impurities come from the process gas has been checked by using gas purifiers like in Ref. [82]. It was found that purifiers have no notable impact on the electrical properties of unintentionally n-doped μc-SiC:H. Hence, the reason for the n-type conductivity of μc-SiC:H films has not been understood so far. The investigation of the unintentional n-doping is a key point of the present thesis (see Chapt. 4).

Beside the study of doping mechanisms in n-type μc-SiC:H films, it is also evaluated which deposition technique, HWCVD or PECVD, is most suitable for im-

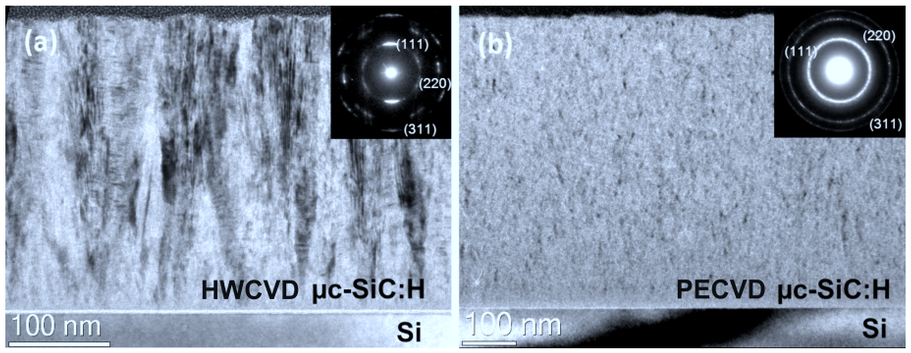

Figure 2.5.: *Bright field transmission electron microscopy micrographs of (a) HWCVD and (b) PECVD grown µc-SiC:H(n) with corresponding diffraction patterning. With the courtesy of F. Köhler taken from Ref. [73].*

plementing μc-SiC:H(n) as a window layer. From the opto-electrical properties in Tab. 2.1 it is not clear which technique is most suitable. There seems to be only a slight advantage of using HWCVD, due to highest E_g for $\sigma \geq 10^{-6}$ S/cm which seems to be related to larger crystalline grains in HWCVD grown μc-SiC:H(n) films. In Fig. 2.5, two bright field transmission electron microscopy (TEM) cross sectional micrographs of HWCVD and PECVD grown μc-SiC:H(n) films with corresponding diffraction patterning as inlets are illustrated showing the differences in microstructure.

The implementation in a SHJ solar cell is problematic from the preparation process point of view for both types of μc-SiC:H(n) film. On one hand, a high density of atomic H in the gas phase is needed to grow wide bandgap μc-SiC:H(n) [9, 55], but on the other hand, it was reported several times that a high H density leads to etching of the c-Si surface so that the surface passivation quality is significantly degraded [11, 83, 84]. Thus, it is an issue to use conventional passivation layers, e.g., a-Si:H(i), in combination with wide bandgap μc-SiC:H(n) deposited by HWCVD or PECVD. Therefore, it is crucial to find an approach to implement high quality μc-SiC:H(n) in a SHJ solar cell device and at the same time achieve a high passivation quality. So far, only Miyajima et al. [11, 84] reported a first successful approach which lead to a decent passivation quality with V_{oc} up to 680 mV. The approach

consists of a two step deposition method where first an amorphous SiC buffer layer of 1-2 nm is deposited before the deposition condition are changed to deposit the μc-SiC:H(n) layer. But 680 mV is not satisfactory, therefore in the second part of this thesis (see Chapt. 5) two new approaches are introduced.

3. Experimental details

In this chapter experimental details and characterization methods are described. In the first section the deposition parameters for the μc-SiC:H(n) preparation are listed. In the second section details of the structural characterizations are addressed, which is followed by a third section, where the characterization methods for the opto-electronic properties are described. The last section contains device relevant information about passivation and solar cell characterization.

3.1. Preparation of microcrystalline silicon carbide

Hot wire chemical vapor deposition (HWCVD) Most of the μc-SiC:H(n) films were grown in a Hot Wire Chemical Vapor Deposition (HWCVD) system that was built in-house. As illustrated in Fig. 3.1(a), the HWCVD vacuum chamber contained three filaments, a heater, and a substrate holder. The Rhenium filaments had a diameter of 0.5 mm were curled from originally 15 cm to an effective length of 10 cm and were mounted with a distance of 3 cm to each other on a stainless steel filament holder. The possible distances from filament to substrate ($d_{\text{f-s}}$) were in the range of 40-100 mm. If not specified otherwise, $d_{\text{f-s}}$ was kept at 97 mm. Beneath each filament there was a gas tube with an array of small holes to inject the mixed gases towards the heated filament, working similarly as a shower head. The filament temperature (T_{f}) was varied by changing the electrical current and was measured with a pyrometer (Raytek Marathon). In this work, the highest T_{f} used was 2200 °C, which corresponds to an electrical current of up to 60 A and a voltage of up to 17 V. If not specified otherwise, the T_{f} was kept at 1950 °C, for investigations on the μc-SiC:H(n) material properties, and was kept at 1800 °C, for implementations of μc-SiC:H(n) layers in silicon heterojunction solar cells. Every week the filaments were heated

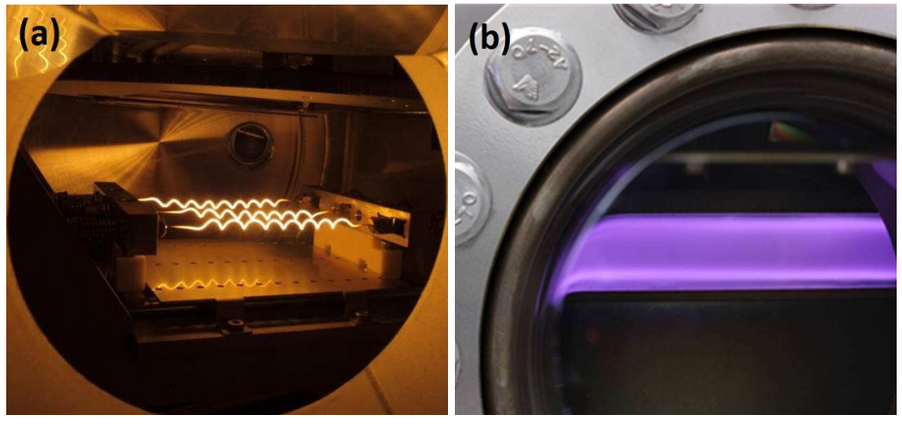

Figure 3.1.: *(a) HWCVD-chamber and (b) PECVD-chamber during deposition process.*

up in the vacuum without any process gas for 10 min at 1800 °C to avoid degradation of the filaments by carbonization or silanization. The heater temperature (T_{H}) could be increased up to 550 °C. The distance between heater and substrate was about 1 cm. The gases used for the deposition were molecular hydrogen (H_2) and monomethylsilane (MMS) diluted to 5 % in H_2. The corresponding gas flow rates could be increased up to 500 sccm and 100 sccm, respectively. From both gas flow rates the concentration of MMS (c_{MMS}) is determined. The deposition pressure was kept at 0.75 mbar for all depositions.

Plasma enhanced chemical vapor deposition (PECVD) Some μc-SiC:H(n) films for the study were prepared by using Plasma Enhanced Chemical Vapor Deposition (PECVD). The PECVD chamber during the process is pictured in Fig. 3.1(b). All PECVD grown films were deposited using a 81.14 MHz generator (Dressler CESAR) with a forward power (P_{f}) of up to 200 W. The electrode had a size of 140 mm, the electrode distance was 14 mm, and the heater was always in contact with the backside of the substrate carrier during the deposition. The T_{H} was kept at 450 °C. Like for HWCVD, MMS and H_2 were used as process gases. The corresponding flow rates were mostly 6 sccm and 148 sccm, respectivley, wich corresponds to c_{MMS} of 0.2 %. The deposition pressure was kept at 1.00 mbar.

3.2. Preparation of silicon wafer and thin films

Wafer and cleaning Two types of wafer were processed for investigations on the passivation and on the energy conversion efficiency of SHJ solar cells. Either double side polished 250 μm thick float zone wafers or double side textured 170 μm thick Czochralski wafers with resistivity around 3.0 Ωcm were used. All wafers were pre-cleaned by the supplier before shipping using complete RCA (Radio Croporation of America) treatment [85]. Prior to the deposition of an a-SiO_x:H(i) passivation layer, the wafers were treated by a mixture of sulfuric acid and hydrogen peroxide to clean off organic residues, followed by a 5 min dip in 1 % diluted hydrofluoric acid (HF) to remove any oxide from the wafer surface. Prior to the growth of an ultra-thin SiO_2 tunnel oxide layer, the wafers were only dipped into a 1% diluted HF solution for 10 min.

a-SiO_x:H(i) The a-SiO_x:H(i) passivation layers were deposited with PECVD. For oxygen free a-Si:H(i) films, the T_{H} was 140 °C, the frequency was 13.56 Hz, and the P_{f} was 4 W. Silane gas at 10 sccm and hydrogen gas at 90 sccm were used at a p of 1.00 mbar. The deposition lasted 92 s on double side polished wafers and 157 s on double side textured wafers. Both deposition times correspond to an effective thickness of around 8 nm. After the deposition the samples were annealed at 200 °C at atmosphere for 48 h. For a-SiO_x:H(i) films with $x > 0$ the T_{H} was 235 °C, the frequency was 81.14 Hz, and the P_{f} was 1 W. Silane gas at 11.2 sccm, hydrogen gas at 10 sccm, and carbon dioxide gas at 4.11 sccm were used at a p of 0.25 mbar. The deposition took 14 s for the front side and 21 s for the back side, which corresponds to 4 nm and 8 nm, respectively. After the deposition the samples were not annealed.

SiO_2 Ultra-thin SiO_2 passivation layers were grown wet-chemically by using a nitric acid solution (HNO_3) with a concentration of 69.5 % at room temperature. Higher temperatures of up to 110 °C, which is the boiling temperature of HNO_3, did not lead to significantly better passivation quality. Therefore, for safety reasons and for simplicity the solution was not heated.

Transparent conductive oxide (TCO) and anti-reflection coating (ARC) For TCO in a two-side contacted SHJ solar cell a 70 nm thick ITO film was sputtered on top of the μc-SiC:H(n) as it was also used by Ding et al. [50]. For IBC-SHJ solar cells, a triple layer anti-reflection coating (ARC) was developped where silicon nitride (SiN_x) and magnesium fluoride (MgF_2) layers were added to the front side of the solar cell. The SiN_x layers were deposited in a plasma-enhanced chemical vapor deposition chamber using 7.8 sccm of SiH_4 and 10 sccm of NH_3 diluted in 450 sccm of Argon and 138 sccm of Helium. The chamber pressure was 8 Pa, the temperature was 100 °C, and the ICP Power was 700 W. MgF_2 layers were thermally evaporated.

3.3. Characterization of structural properties

All μc-SiC:H(n) films were deposited on 5×10 cm^2 glass (Corning EAGLE XG) and on 15×15 mm^2 c-Si substrates.

Profilometer Before the deposition of μc-SiC:H(n), a dot was planted in the center of each substrate using a permanent marker. After the deposition, the dot was removed with isopropanol, so that a hole of ca. 1 mm diameter and a depth down to the substrate surface remained in the film. The crater edges served to determine the film thickness (d_{SiC}) using a profilometer (Vecco DEKTAK 6M Stylus Profiler). The estimated error of the measurement varied between 5 % and 10 %, depending on the roughness of the film surface. The deposition rate was then calculated by dividing the d_{SiC} by the deposition time. In this work, all thicknesses were in the range of 100-200 nm.

Fourier transform infra-red (FTIR) spectroscopy Fourier transform infra-red spectroscopy (FTIR) is useful to derive material properties concerning composition and structure. The technique is based excitation of electric dipoles in the material that leads to molecular vibration. More information can be found in Ref. [86]. In this work, FTIR spectrometer (Nicolet 5700 FTIR) was used to measure the resonances of the Si-C mode oscillation at 770-800 cm^{-1} [87] and Si-H_x related mode oscillations at 2000-2150 cm^{-1} [88]. The FTIR peaks provide fast information

about structure (Si-C mode) and hydrogen content (Si-H mode) of the μc-SiC:H(n) films. To determine the hydrogen content ([H]) quantitatively, the area under the Si-H peak was integrated from 1900-2300 cm^{-1} and was used for the calculation as described by King et al. [89]. It is worth to mention, that for all samples the C-H related stretching modes at 2860-3000 cm^{-1} [90] were not distinguishable from the background noise. All FTIR spectra were corrected by the film thicknesses as described by Langford et al. [91].

Secondary ion mass spectrometry (SIMS) Secondary ion mass spectrometry (SIMS) is a useful technique to obtain a chemical analysis - especially for impurities. It is possible to perform a depth profiling with a resolution of a few nanometers. Further information may be found in Ref. [92]. SIMS has been performed in UHV-ambient (residual gas pressure $< 1 \times 10^{-10}$ mbar) with a quadrupole instrument (ATOMIKA 4000) to determine the carbon fraction (X = [C]/([C]+[Si])) of μc-SiC:H(n), the oxygen content ([O]), the nitrogen content ([N]), and the hydrogen content ([H]). In order to get better statistics and to rule out lateral deviation in the film composition, SIMS analysis of the μc-SiC:H(n) films has been repeated at least once in a different area of each sample. For depth profiling of [O] and [N] within the μc-SiC:H(n) films, near-normal 6 keV Cs^+-bombardment and detection of negative secondary ions have been applied. The SIMS raw data have been quantified by relative sensitivity factors (RSFs), as determined via ^{16}O (dose 2×10^{15} cm^{-2}) and ^{14}N (dose 1×10^{16} cm^{-2}) ion implantation (150 keV ion acceleration in both cases) in single crystalline SiC-wafer [93]. Depth profiles of the silicon and carbon matrix elements have been collected during 6 keV Cs^+-bombardment at 65 °, with respect to the sample normal, applying the CsM^+ technique [94]. The resulting $^{133}Cs^{28}Si^+$ and $^{133}Cs^{12}C^+$ dimer ion count rates have been quantified assuming constant sensitivity factors for both matrix species, as previously reported in the literature [95], [96]. In case of quantitative matrix elements analysis, the ratio of CsM^+ sensitivity factors has been determined during sputter removal of single crystalline SiC wafer applying exactly the same bombardment conditions as used for depth profiling of the μc-SiC:H(n) films, i.e., proceeding these calibration runs at least twice for each μc-SiC:H(n) samples-set mounted on the SIMS sample holder.

X-ray diffraction (XRD) X-ray diffraction (XRD) has been measured to investigate crystalline structure of μc-SiC:H(n). The diffractometer (Bruker D8 Advance) was used in Bragg-Bretano-angle mode for the measurement. An average c-SiC grain size (L_{SiC}) was derived from the 3C-SiC peak by using the Scherrer equation [97]. The time of the measurement was chosen, in order to provide a resolution of 1 nm. More details on the working principles of XRD and the measurement setup can be found in Ref. [74].

3.4. Characterization of opto-electronic properties

Coplanar electrical conductivity measurement The lateral electrical conductivity (σ) of the films was measured between two thermally evaporated coplanar silver contacts. The measurement was performed in the dark and at 300 K. The distance between the contacts was 0.5 mm and the sample was always cut out of the same location in center of the glass substrate, where the films were most homogenous.

Thermopower measurement The charge carrier density (n) and the charge carrier mobility (μ) are related to σ by

$$\sigma_{\mathrm{d}} = \mathrm{q}n\mu, \tag{3.1}$$

where q is the elementary charge. To acquire more insights of the electrical transport mechanisms of μc-SiC:H(n), the n and μ were derived from combined measurements of the σ and the thermopower (S) over a coplanar contact distance of 4 mm in vacuum, as reported in more detail elsewhere [98, 99]. The values for n were derived by using the following relation of S [100]:

$$S = \frac{\mathrm{k_B}}{\mathrm{q}} \left[\frac{4F_3(\mu^*(T))}{3F_2(\mu^*(T))} - (\mu^*(T)) \right], \tag{3.2}$$

where $\mathrm{k_B}$ is the Boltzmann constant, F_{x} is the Fermi-Dirac integral, and $\mu^*(T)$ is the reduced Fermi-energy. The Fermi-Dirac integral is a measure that corresponds to the transition probability from one state to another. The eq. 3.2 was then used in the following expression for n:

$$n(T) = N_{\mathrm{C}}(T) F_{1/2}(\mu^*(T)). \tag{3.3}$$

Based on former investigations of μc-SiC:H(n), it was assumed that the effective density of states at the conduction band N_c is $3 \times 10^{15}\ T^{3/2}$ [81]. Each data point of S was determined by varying the temperature gradient from +30 K to -30 K. In this measurement geometry, surface oxide layers etc. should not play a role as long as they do not result in carrier accumulation within the material. In order to determine also the activation energy of n (E_n) and the activation energy of μ (E_μ), the sample temperature was varied from 360 K to 600 K. The values were derived from the corresponding slopes in Arrhenius plot at 360 K. More detailed information can be found in Ref. [99, 101]

Photothermal deflection spectroscopy (PDS) The optical absorption coefficient (α) as a function of the photon energy was investigated using an in-house photothermal deflection spectroscopy (PDS) measurement setup [102]. The method is very sensitive, so that it is also possible to detect very low α. Thus, in addition to the determination of the optical bandgap of the material, also the sub-bandgap absorption was measured which provides further information about defect densities and free-carrier absorption. The photon energy ranged from 0.5 eV to 4.0 eV. A refractive index of 2.5 was assumed for the evaluation of the measured data. A variation of the refractive index from 2.0 to 3.0 showed only very small effect on the absolute values of α.

Ellipsometery The refractive index and the extinction coefficient of μc-SiC:H(n), SiN_x and MgF_2 were derived from ellipsometer measurements using SE 800 from the SENTECH. Also the SiO_2 layer were measured by ellipsometer to obtain the thickness which was derived by using the software. More detailed information about ellipsometry can be found in Ref. [103].

3.5. Characterization of passivation and solar cell

Photo-conductance measurement The effective minority carrier lifetime (τ_{eff}) in a silicon wafer was measured with a Sinton Consulting WCT-120 quasi-steady state photo-conductance (QSSPC) setup [104]. In this measurement, minority charge

carriers are photogenerated homogeneously in the wafer by a infra-red light pulse. The amount of photogenerated minority charge carriers, here named Δn for both types of minority charge carriers in p- and n-type wafers, changes with time, which can be described as the difference between generation rate (G) and recombination rate. The recombination rate can be written as $\Delta n/\tau_{\text{eff}}$, where the effective minority charge carrier lifetime is denoted by τ_{eff}. Thus, the change in Δn with time, can be rewritten by

$$\frac{\mathrm{d}}{\mathrm{d}t}\Delta n = G - \frac{\Delta n}{\tau_{\text{eff}}}, \tag{3.4}$$

and

$$\tau_{\text{eff}} = \frac{\Delta n(t)}{G(t) - \frac{\mathrm{d}}{\mathrm{d}t}\Delta n}. \tag{3.5}$$

Generally, the τ_{eff} is limited by defects in the bulk or at the surfaces and can also be written as

$$\frac{1}{\tau_{\text{eff}}} = \frac{1}{\tau_{\text{bulk}}} + 2 \times \frac{1}{\tau_{\text{surface}}}, \tag{3.6}$$

where τ_{bulk} is the lifetime in the bulk and τ_{surface} the lifetime at the surface. Usually, a silicon wafer has a very low bulk defect density as compared to the surface defect density that $\tau_{\text{bulk}} \gg \tau_{\text{surface}}$. Therefore, the term $1/\tau_{\text{bulk}}$ can be neglected for silicon wafers and the τ_{eff} represents $\tau_{\text{surface}}/2$. For the characterization of the passivation quality the τ_{eff} value is read at $\Delta n \approx 10^{15}$ cm^{-3}. Another way to present the passivation quality of wafer surfaces is by providing an implied open circuit voltage (iV_{oc}):

$$\mathrm{i}V_{\text{oc}} = \frac{\mathrm{k_B}T}{\mathrm{q}} \ln\left[\frac{(\Delta n + N_{\text{A}})\Delta n}{n_{\text{i}}^2}\right], \tag{3.7}$$

where $\mathrm{k_B}$ is the Boltzmann constant, T the temperature, q is the elementary charge, N_{A} the acceptor doping concentration, and n_{i} the intrinsic carrier concentration. The value of iV_{oc} serves as prediction of the maximum achievable open circuit voltage, which is an important parameter with direct influence on the energy conversion efficiency of the solar cell device.

Solar simulator The solar energy conversion efficiency (η) of the solar cells in this work was determined under standard test conditions (AM1.5G, 100 mW/cm^2, 25 °C) by using an an in-house Class AAA solar simulator. The current-voltage (IV) characteristics provided information about the short circuit current ($I_{\text{sc}} = \mathrm{I}(0)$), the

open circuit voltage (V_{oc}, I(V_{oc}) = 0), and the fill factor (FF). The shunt resistance (R_{sh}) was derived from the slope of the IV curve at 0 mV and the series resistance (R_s) was derived from the slope of the IV curve at 0 mA. More fundamental information about the current-voltage relation in a solar cell device can be found in Sec. 2.1.

Differential spectral response and optical photometry The external quantum efficiency (EQE) spectrum provides detailed insight to the photon absorption and the extraction of the photogenerated charge carrier as a function of the wavelength. The EQE spectrum was measured with a custom differential spectral response setup by focusing a light spot of approximately 3 mm^2 between two front contact fingers. A more detailed description of the setup can be found in Ref. [105]. By measuring the spectral reflectance (R) with a calibrated spectrometer (Perkin Elmer LAMBDA 950), it was possible to derive the spectral absorptance (A = 1 - R) of the solar cell. To receive spectral information of the extraction efficiency of the photogenerated charge carriers, the EQE was normalized by A, which is called internal quantum efficiency (IQE).

Transmission line measurement (TLM) Transmission line measurements (TLM) served to determine the contact resistivity (ρ_c) of the whole front side layer stack of the SiO_2 passivated solar cell, i.e., Ag/ITO/μc-SiC:H(n)/SiO_2/c-Si(n). The TLM structure consisted of eight 1.3 × 6.0 mm^2 silver stripes with spacing in between ranging from 0.41 mm to 1.85 mm. The resistances between the stripes were measured by four point probe technique to suppress the parasitic resistance introduced by the probe. By linear extrapolation of the resistances, plotted as a function of the spacing, it was possible to derive the ρ_c from the resistance at the intersection with y-axis. More detailed information about TLM can be found in [106].

Optical simulations To simulate optical losses for different anti-reflection coating stack designs, the OPAL2 [107] software was used together with the measured refractive indices and extinction coefficients. For the c-Si surface morphology randomly distributed, upright pyramids were assumed that posses a characteristic angle of 54.75°and a planar fraction of 8 % (independent planar). The value of 8 % for

planar fraction was derived from the minimum in difference between measured and simulated reflectance of the used textured silicon wafers. For the incident illumination was used a zenith angle of 8°(because reflection measurement performed with 8°) and the AM1.5g spectrum as reported by C. Gueymard [19]. A substrate thickness of 170 μm was assumed for the light trapping model.

4. Material properties of microcrystalline silicon carbide

In this chapter the structural, electrical, and optical properties of μc-SiC:H(n), deposited by HWCVD and PECVD, are discussed in detail. The first section of this chapter focuses on unintentionally doped μc-SiC:H(n) where the material structure in different sample series is related to deposition rate, electrical conductivity, hydrogen content, intensity of the FTIR Si-C stretching mode, c-SiC grain size, carbon fraction, and optical absorption coefficient. The second section is dedicated to the role of oxygen and nitrogen in the μc-SiC:H(n) material. Their effect on electrical conductivity, charge carrier density and mobility, on c-SiC grain size, hydrogen content, and optical absorption coefficient is studied in detail. Finally, the insights of both sections are used to propose a hypothetical model of the electrical transport mechanisms in μc-SiC:H(n).

4.1. Unintentionally doped films

In the past, highly conductive and at the same time highly transparent μc-SiC:H(n) films were produced by HWCVD or PECVD [8, 9, 55]. Finger et al. [9] and Miyajima et al. [8, 55] reported that without adding any doping gas during the growth process the material shows an n-type character with remarkably high lateral electrical conductivity (σ) of up to 10^{-1} S/cm. As no doping gas was added during the film growth, this type of material is called *unintentionally doped* μc-SiC:H(n). In this section six film series are studied in detail with regard to the origin of the unintentional doping. First, the influence of the deposition parameters on film structure, hydrogen content, and stoichiometry is described. Then these morphological

material properties are related to the electrical conductivity. Last, the impact of morphological and electrical properties on optical properties is studied.

4.1.1. Influence of deposition parameters on microstructure

There is only few reports in the literature on the microstructure of unintentionally doped μc-SiC:H(n) films. The microstructure was studied by FTIR spectroscopy [108–110], Raman spectroscopy [79, 111], XRD [79, 110, 112], and electron diffraction [108, 111, 113].

In 2000, Kerdiles et al. systematically studied the Si-C stretching mode in the FTIR spectroscopy around 800 cm^{-1} of sputtered μc-SiC:H(n) films [108]. They fitted the Si-C peak by a Lorentzian peak and a Gaussian peak and attributed the Lorentzian part to a crystalline phase and the Gaussian part to a amorphous phase. Consequently, Kerdiles et al. interpreted the portion of the Lorentzian part as crystalline volume fraction and the Gaussian part as amorphous volume fraction. Since then it is very common that the Lorentzian portion of the Si-C mode is used as equivalent for the crystalline volume fraction, although no further quantitative prove was given. In 2012, Köhler et al. correlated FTIR measurements of the Si-C stretching mode to XRD measurements of the (111)-3C-SiC peak [73,74]. They found that films that exhibited broad FTIR peaks indicating an amorphous character still showed sharp XRD peaks indicating a crystalline character. It was therefore excluded that the Lorentzian portion of the Si-C stretching mode from FTIR is equivalent to a crystalline volume fraction in the films. According to the XRD results the films were generally either crystalline or amorphous. The idea of mixed amorphous and crystalline phases, as it is known from microcrystalline silicon [114], was therefore eliminated for μc-SiC:H(n). Also a general correlation between Lorentzian portion and grain size was excluded, based on two films with similar Lorentzian portion but significantly different grain sizes from TEM [74].

For this thesis, the microstructure is studied via the intensity of the Si-C mode ($I_{\text{Si-C}}$) and the grain size (L_{SiC}) from XRD. The structural properties were obtained from six series of unintentionally doped μc-SiC:H(n) films where the following de-

position parameters were varied: (i) monomethylsilane (MMS) gas concentration (c_{MMS}) in the gas phase, (ii) filament temperature (T_{f}), (iii) MMS flow rate with constant c_{MMS}, (iv) MMS flow rate with constant c_{MMS} using PECVD (all other with HWCVD), (v) distance between filament and substrate ($d_{\mathrm{f\text{-}s}}$), and (vi) film thickness (d_{SiC}). For the series (ii)-(vi) the c_{MMS} was kept 0.3 %.

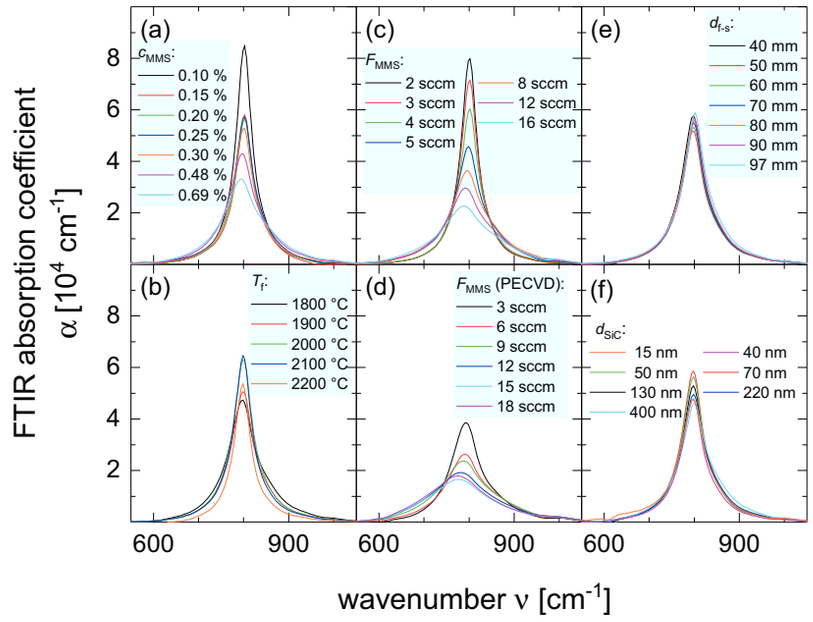

Figure 4.1.: *Si-C stretching mode in FTIR spectrum from unintentionally doped μc-SiC:H(n) film series, where the following deposition parameters were varied: (a) MMS gas concentration c_{MMS}, (b) filament temperature T_f, (c) MMS flow rate while keeping MMS gas concentration constant at 0.3 %, (d) MMS flow rate while keeping MMS gas concentration constant at 0.3 % using PECVD, (e) distance between filament and substrate $d_{f\text{-}s}$, and (f) film thickness d_{SiC}. The sub-figures (c) and (d) are reproduced from Ref. [115], with the permission of AIP Publishing.*

In Fig. 4.1 the Si-C stretching modes from FTIR spectroscopy measurements are shown for the six film series. In Fig. 4.1(a) the peaks of the Si-C mode from the

MMS concentration series show the typical transition from Lorentzian shape towards a more and more Gaussian shape with increasing c_{MMS}. A similar behavior is observed with increasing MMS flow rate for HWCVD in Fig. 4.1(c) and for PECVD in Fig. 4.1(d). The broadening of the peaks is accompanied by a shift of the peak position from 802 cm^{-1} to 790 cm^{-1} for the HWCVD grown films and from 794 cm^{-1} to 775 cm^{-1} for the PECVD grown films. The peak shift towards lower wavenumbers signifies a decrease in binding energy between Si and C atoms, which equally corresponds to an increase in Si-C binding lengths. In Fig. 4.1(b) the Si-C modes from the filament temperature series does not show a transition towards Gaussian shape and does not show any shift in position. With increasing T_{f} the Si-C mode became sharper, where the full width at half maximum (FWHM) decreased from 73 cm^{-1} to 44 cm^{-1}. The intensity of the Si-C mode ($I_{\mathrm{Si\text{-}C}}$) rose for increasing T_{f} up to 2100 °C. The Si-C modes from the filament-substrate distance series in Fig. 4.1(e) are nearly identical for $d_{\mathrm{f\text{-}s}}$ in the range of 40-100 mm. The Si-C modes from the film thickness series also exhibit Lorentzian shapes with small variation in the intensity of the Si-C mode. The $I_{\mathrm{Si\text{-}C}}$ increased first with increasing d_{SiC} from 15 nm to 70 nm and then decreased with increasing d_{SiC} from 70 nm to 540 nm. In the following the value of $I_{\mathrm{Si\text{-}C}}$ is used to correlate the FTIR results to other material parameters.

The microstructure was also analyzed by XRD for the MMS flow rate series (HWCVD and PECVD) and for the filament-substrate distance series. The corresponding diffractograms are shown in Fig. 4.2(a-c). In agreement with the results from Köhler et al. [73, 74], no amorphous phase was detected which would have a diffraction maximum at a diffraction angle of around 32°. Instead, there is only the (111)-3C-SiC peak visible at diffraction angles in the range of 35-36°for all three series. Other peaks were not present which could have been related to a hexagonal phase, stacking faults, or to other orientations of the cubic lattice, e.g. (220) and (311). Similar to the Si-C stretching mode from FTIR spectroscopy, the (111)-3C-SiC peaks of the MMS flow rate series (HWCVD and PECVD) in Fig. 4.2(a-b) decreased in intensity and broadened in width for increasing F_{MMS}. A shift in the peak position towards lower diffraction angles with increasing F_{MMS} was present as it was also observed for the FTIR spectra in Fig. 4.1(c,d) where the Si-C stretching mode shifted to lower wavenumbers. Similarly, the peak shift towards lower

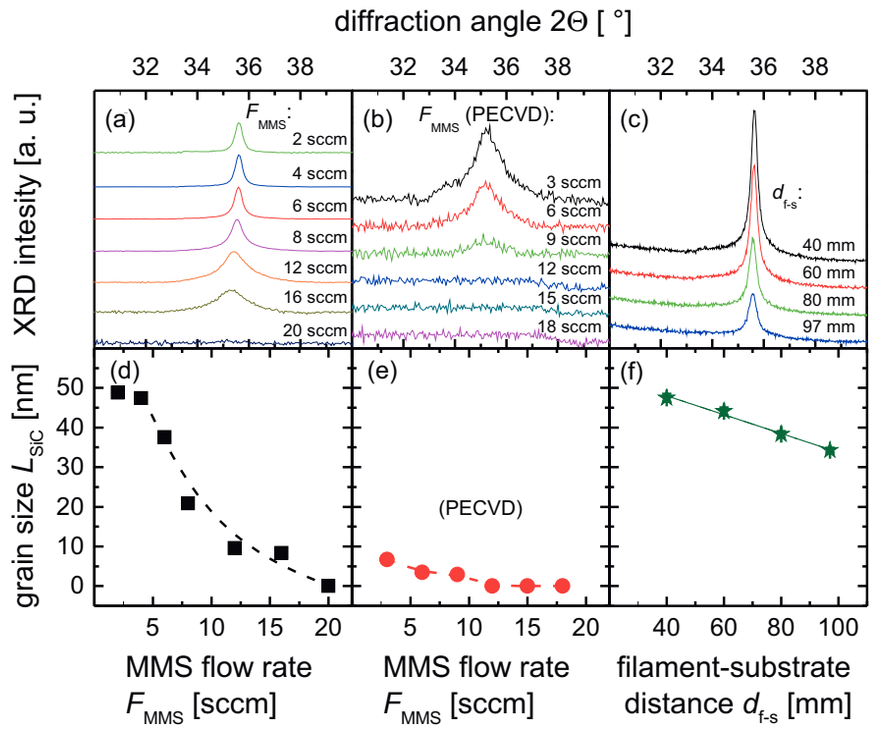

Figure 4.2.: *(a-c) (111)-3C-SiC peaks from XRD from unintentionally doped μc-SiC:H(n) film series, where the following deposition parameters were varied: (a) MMS flow rate while keeping MMS gas concentration constant at 0.3 % using HWCVD, (b) MMS flow rate while keeping MMS gas concentration constant at 0.3 % using PECVD, and (c) distance between filament and substrate $d_{f\text{-}s}$ during the HWCVD. (d-f) Grain size as a function of the respective deposition parameters. The grain size was obtained by using the Scherrer equation [97]. The sub-figures (a),(b),(d), and (e) are reproduced from Ref. [115], with the permission of AIP Publishing.*

diffraction angles indicates, according to Bragg's equation [116], an increase in Si-C binding lengths. Although the Si-C stretching modes in the FTIR spectra were very similar for different $d_{\text{f-s}}$, the (111)-3C-SiC peak increased significantly for smaller $d_{\text{f-s}}$.

From all diffractograms an average grain size (L_{SiC}) was derived from the (111)-3C-SiC peak by using the Scherrer equation [97]. The resulting values of L_{SiC} are plotted in Fig. 4.2(d,e) as a function of F_{MMS} (HWCVD and PECVD) and in Fig. 4.2(f) as a function of $d_{\mathrm{f\text{-}s}}$. All L_{SiC} values decreased with increasing F_{MMS} or $d_{\mathrm{f\text{-}s}}$. The grain sizes were in the range of 0-50 nm for HWCVD grown films and in the range of 0-7 nm for PECVD grown films. In Fig. 4.3(a) the intensity of the Si-C stretching mode is plotted as a function of the grain size. The data points that were obtained from the F_{MMS} series using HWCVD can be fitted linearly where the slope is about 1000 $\mathrm{cm}^{-1}/\mathrm{nm}$ and the value for $I_{\mathrm{Si\text{-}C}}$ at zero L_{SiC} is 2.3×10^4 cm^{-1}. The data points of the PECVD grown films are mostly also located on the fit of the HWCVD grown films, but the data points of the $d_{\mathrm{f\text{-}s}}$ series does follow the fit of the HWCVD grown films. At this point, it is worth to mention that is open for the diffractograms in Fig. 4.2(a-c) without (111)-3C-SiC peak if the measurement time was to short to distinguish the (111)-3C-SiC peak or if the films were amorphous. Nevertheless, the values for the derived grain sizes lose validity if they are in the range of the lattice plane distance, i.e., $\leq$1 nm.

The difference in grain size arising from the different growth methods are in good agreement with the grain sizes that were observed by TEM in the past [73, 84, 111]. Larger L_{SiC} of fims that were grown using HWCVD compared to PECVD grown films can be explained by the higher hydrogen (H) radical density [117] and the absence of ion bombardment [118]. The atomic H in form of radicals or ions is known to be essential for the formation of ordered microstructure in μc-SiC:H(n) films [9]. The H ions however, due to the high kinetic impact on the substrate surface, damage the crystalline growth and lead to defect creation [119].

The H radical density in the gas phase plays an important role for all six film series that were introduced so far in this thesis. It is known that is possible to increase the H radical density by decreasing the MMS gas concentration [9] and by increasing the filament temperature [117, 120]. According to Umemoto et al. [117], more H radicals are generated at the filaments if T_{f} is higher. The reported H radical densities increased by power law. Another way to increase the H radical density is by increasing the deposition pressure during the film growth [72]. An increased H

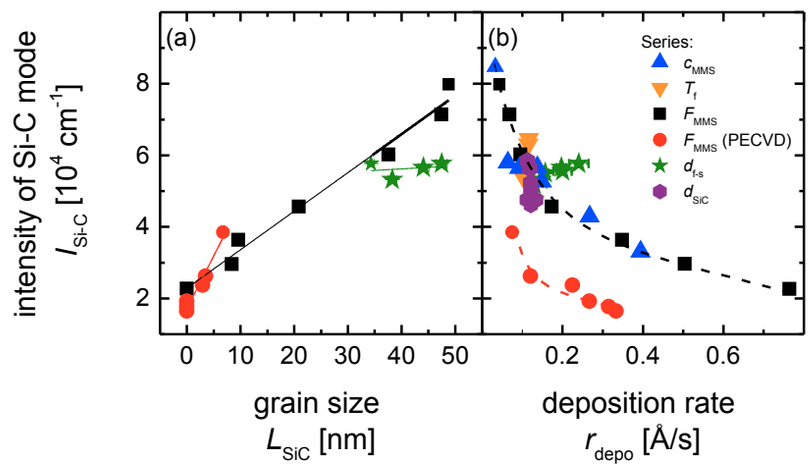

Figure 4.3.: *Intensity of Si-C stretching mode $I_{Si\text{-}C}$ from FTIR spectroscopy (Fig. 4.1) as a function of (a) XRD grain size and of (b) deposition rate r_{depo} for unintentionally doped μc-SiC:H(n) film series. Straight lines represent linear fits of the series with the corresponding color. Dashed lines only serve as guide to the eye.*

radical density leads to a stronger H etching of the substrate including already grown films. Therefore, weak atomic bonds at the surface of the film are erased during the deposition process which is in favor of crystalline growth. More detailed explanations on H etching and crystalline growth can be found in Ref. [121–123]. But H radical density cannot be the only effect. In the case of the series where the MMS gas flow rate was varied despite of constant MMS gas concentration (= 0.3 %), the resulting FTIR spectra (Fig. 4.1(c,d)) and the resulting diffractograms (Fig. 4.2(a,b)) resemble the results of the c_{MMS} variation in Fig. 4.1(a) and Ref. [9]. In other words, the H radical density in the gas phase was the same for all films that were deposited with different total flow rates, but the resulting FTIR spectra (Fig. 4.1(c,d)) and the resulting diffractograms (Fig. 4.2(a,b)) resemble the results of the c_{MMS} variation in Fig. 4.1(a) and Ref. [9]. Also the FTIR and XRD results of the filament-substrate distance series and the film thickness series cannot be explained by a higher effective H radical density in the vacuum chamber. All four series, i.e., the F_{MMS} (HWCVD and PECVD), the $d_{\mathrm{f\text{-}s}}$, and the d_{SiC}, have barely been reported in the literature so

far.

The radical density in the gas phase is not the only aspect that influences the microstructure. As the F_{MMS} was decreased while maintaining the c_{MMS} constant at 0.3%, an increased residence time of the MMS molecules in the chamber might be the origin of higher $I_{\mathrm{Si\text{-}C}}$ and larger L_{SiC}, due to longer time of atoms that are adsorbed on the surface to migrate to strong Si-C bonding sites that form a crystallite SiC phase. In Fig. 4.3(b) all values of $I_{\mathrm{Si\text{-}C}}$ are plotted versus the deposition rate (r_{depo}) during the growth of the samples. In the case of the F_{MMS} series using HWCVD, the decrease in the r_{depo} from 0.76 Å/s to 0.04 Å/s correlates with the increase in $I_{\mathrm{Si\text{-}C}}$. The data points from the c_{MMS} series and from the filament temperature series, where the radical density in the gas phase was varied, follow the same trend as the data points from F_{MMS} series, where the radical density in the gas phase was kept constant. The data points from the PECVD grown films show the same behavior of increasing $I_{\mathrm{Si\text{-}C}}$ and L_{SiC} for lower deposition rates. Therefore, r_{depo} seems to determine the resulting microstructure, where reducing r_{depo} gives rise to higher $I_{\mathrm{Si\text{-}C}}$ and larger L_{SiC}. Only for the films of the filament-substrate distance series the suggestion was not true. There, the $I_{\mathrm{Si\text{-}C}}$ remained comparable for increasing r_{depo} and the L_{SiC} even increased with increasing r_{depo}. The simultaneous increase in L_{SiC} and r_{depo}, when distance between filaments and substrate is reduced, might arise from the reduced distance that the generated radicals have to overcome. The impact of the radicals from the gas phase has changed, although all flow rates were kept constant. All radicals that are generated at the filaments possess a mean free path which is mainly defined by the radical density in the gas phase [117,124]. The higher the radical density the higher is the probability for a generated radical to hit another radical which can lead to recombination of both radicals. Therefore, a reduction of the distance between filament and substrate should increase the probability of the generated radicals to reach the surface of the substrate.

4.1.2. Stoichiometry and hydrogen content

Up to this point in this thesis, it was shown how the microstructure of unintentionally doped μc-SiC:H(n) films is influenced by different deposition parameters. In

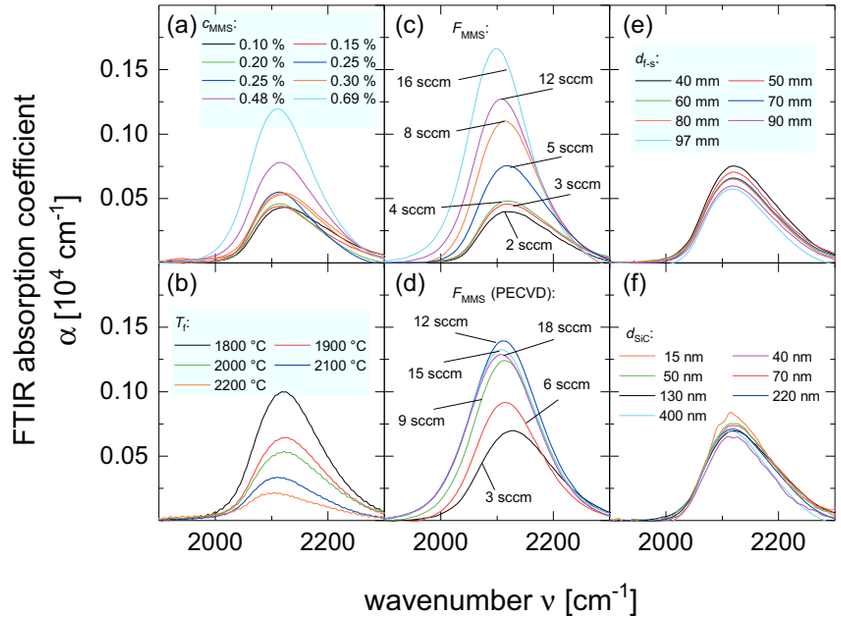

Figure 4.4.: *Si-H related modes in FTIR spectrum from unintentionally doped μc-SiC:H(n) film series, where the following deposition parameters were varied: (a) MMS gas concentration c_{MMS}, (b) filament temperature T_f, (c) MMS flow rate while keeping MMS gas concentration constant at 0.3 %, (d) MMS flow rate while keeping MMS gas concentration constant at 0.3 % using PECVD, (e) distance between filament and substrate $d_{f\text{-}s}$, and (f) film thickness d_{SiC}. The sub-figures (c) and (d) are reproduced from Ref. [115], with the permission of AIP Publishing.*

the following, the hydrogen content ([H]) and the stoichiometry in unintentionally doped μc-SiC:H(n) are studied by using the same film series that were introduced before to complete the microstructure picture.

In Fig. 4.4 the Si-H related modes in the FTIR spectra are presented for the films of the six series. The C-H related stretching modes at 2860-3000 cm-1 [90] were not distinguishable from the background noise. The Si-H modes of the films from the c_{MMS}, T_{f}, and F_{MMS} (HWCVD and PECVD) in Fig. 4.4(a-d) increase inversely

in intesity as compared to the corresponding Si-C modes in Fig. 4.1(a-d). The Si-H modes of the films of the $d_{\text{f-s}}$ series increase in intensity with increasing $d_{\text{f-s}}$, although the Si-C modes were almost indifferent. The Si-H modes of the films of the d_{SiC} series are comparable for all thicknesses of 15-400 nm. The small differences can be interpreted as scattering.

In Fig. 4.5 SIMS depth profiles are plotted for the SiH/Si and CH/Si relations for selected films with $F_{\text{MMS}} = 2$ sccm and $F_{\text{MMS}} = 16$ sccm from the F_{MMS} series (HWCVD). Both relations confirm that the average hydrogen content was strongly increased for $F_{\text{MMS}} = 16$ sccm. Furthermore, the depth profiles all exhibited a sharp increase in [H] near the interface to the substrate. This increase in [H] at the interface is attributed to the more hydrogen rich amorphous nucleation zone of the films, as it can be found in the TEM micrographs published for this type of HWCVD grown μc-SiC:H(n) [9, 73, 80, 113] and which might be of interest when μc-SiC:H(n) of less than 30 nm thickness is implemented in a SHJ solar cell (Sec. 5.1.2, Sec. 5.2.1).

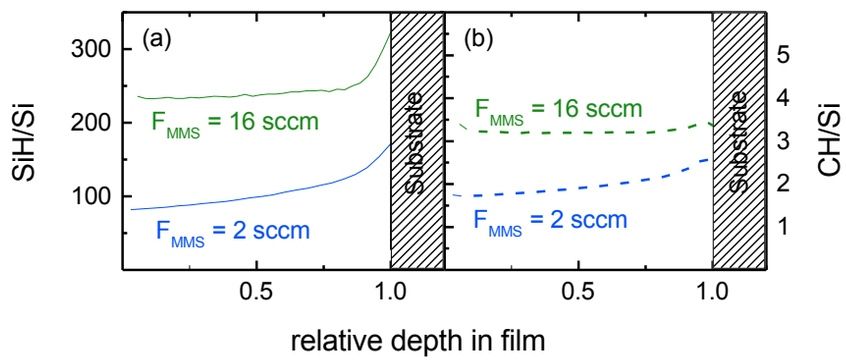

Figure 4.5.: *SIMS depth profiles of (a) SiH/Si and (b) CH/Si for two films from the F_{MMS} series (HWCVD) with F_{MMS} of 2 sccm and 16 sccm.*

In Fig. 4.6(a,b) the hydrogen content, obtained from the Si-H related modes in Fig. 4.4 as described in Ref. [89], is plotted as function of the intensity of the Si-C stretching mode from FTIR measurement and as a function of $^{30}\text{Si}^{1}\text{H}^{-}/^{30}\text{Si}^{-}$ from

SIMS measurement. The [H] decreased from 1.5×10^{22} at/cm^3 to 0.5×10^{22} at/cm^3 with $I_{\text{Si-C}}$ increasing from 2×10^4 cm^{-1} to 8×10^4 cm^{-1}, whereby [H] seems to saturate around 0.5×10^{22} at/cm^3 for $I_{\text{Si-C}} > 5 \times 10^4$ cm^{-1}. The values for the hydrogen content of the F_{MMS} series (HWCVD) are supported by the values for $^{30}\text{Si}^1\text{H}^-/^{30}\text{Si}^-$ from SIMS measurement in Fig. 4.6(b) where both sets of data originating from very different measurement methods show a good correlation in form of linear alignment of data points.

Since the solubility of H in c-SiC is very low (10^{14} at/cm^3 [125]), it is reasonable that most of H atoms should be situated outside the c-SiC grains. As further, the material does not contain an amorphous phase in the XRD measurements, H atoms should rather be located at the c-SiC grain surfaces. In the nucleation zone the size of the grain is probably smaller which gives rise to a higher [H] as it was indicated by the SIMS depth profiles in Fig. 4.5. The suggestion of hydrogen covering the c-SiC grains is supported by the data in Fig. 4.6(a) which can be interpreted in the way that for increasing grain size the hydrogen content is decreased. Indeed the total area of all grain surfaces decreases with increasing grain size. The suggestion, that the H atoms terminate the grain surface, is also in good agreement with the work of A. Heidt et al. [113, 126], who observed a high degree of disorder within the nucleation zone and at heterogeneous grain boundaries, by using energy filtered transmission electron microscopy.

After the investigation of the microstructure of unintentionally doped μc-SiC:H(n) and hydrogen in the films, the stoichiometry of the materials is investigated in the following. It has been suggested by Ref. [8, 9] that a deposition from MMS gas would lead to perfectly stoichiometric μc-SiC:H(n) layers, because MMS (CH_3SiH_3) contains Si and C in equal proportions. However, the carbon fraction (X) shown in Fig. 4.6(c), which was determined from SIMS measurements, reveals a Si excess for all films from the F_{MMS} series (HWCVD and PECVD). The carbon fraction increased from 0.38 to 0.49 with increasing grain size for both deposition methods (Fig. 4.6(c)).

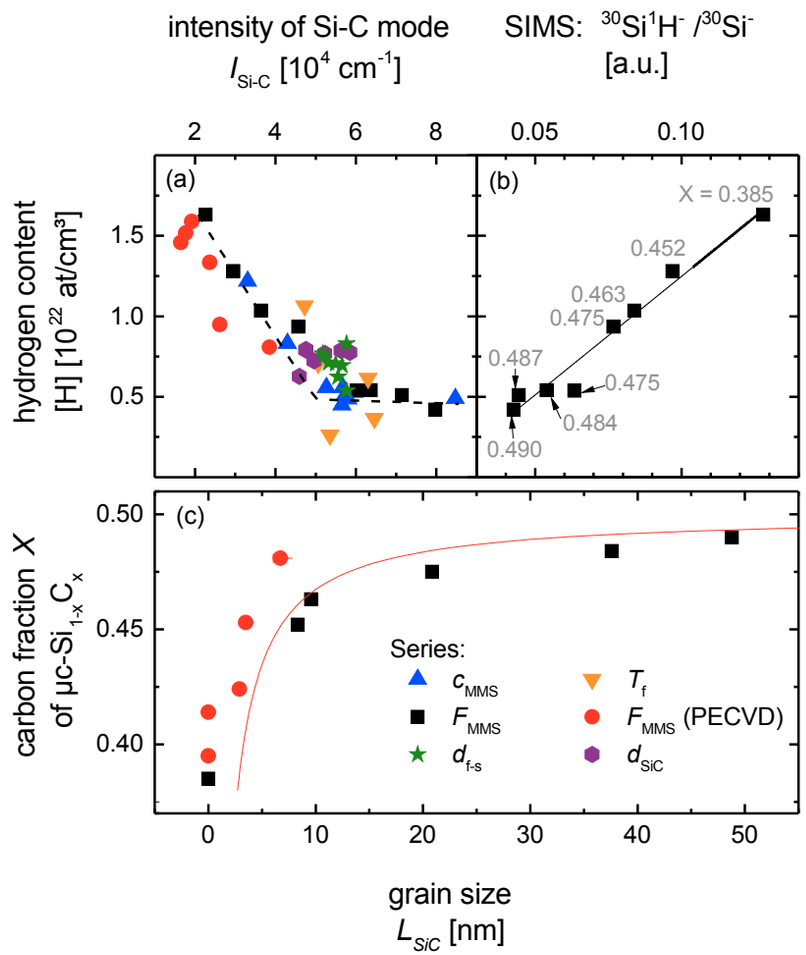

Figure 4.6.: *(a) Hydrogen content as a function of intensity of Si-C stretching mode from FTIR spectroscopy of unintentionally doped µc-SiC:H(n) film series, where the following deposition parameters were varied: MMS gas concentration c_{MMS}, filament temperature T_f, MMS flow rate while keeping MMS gas concentration constant at 0.3 %, MMS flow rate while keeping MMS gas concentration constant at 0.3 % using PECVD, distance between filament and substrate $d_{f\text{-}s}$, and film thickness d_{SiC}. (b) Hydrogen content derived from FTIR measurement as a function of $^{30}Si^1H^-/^{30}Si^-$ from SIMS measurement for films of the F_{MMS} series (HWCVD). (c) Carbon fraction X obtained from SIMS measurement as a function of grain size from XRD for films from both F_{MMS} series (HWCVD and PECVD). The sub-figure (c) is reproduced from Ref. [115], with the permission of AIP Publishing.*

According to Köhler et al. [73] and according to the measured XRD data of the present work (Fig. 4.2), there is no amorphous phase detected for μc-SiC:H(n). Only films with zero grain size can be considered to be amorphous. The c-SiC grains are assumed to be stoichiometric, the excess Si atoms then should be located outside of the grains, i.e, at the grain surface and in the nucleation phase. If the excess Si atoms are located outside the grains, the carbon fraction should increase with increasing grain size, due to the decrease of surface to volume fraction. In Fig. 4.6(a) that requirement is confirmed by the grain sizes plotted versus the corresponding carbon fractions. In order to describe the relation between X and L_{SiC} arithmetically, the shape of the c-SiC grains is simplified to cubes with a size of L. As the thickness of the surface layer can be written as $D^{-1/3}$, where D is the c-SiC density (9.68×10^{22} at/cm^3 [127]), the volume of the surface layer (V_{s}) of a single cubic grain can be written as

$$V_s = 6 \times L^2 \times D^{-1/3}. \tag{4.1}$$

Originally, the surface layer of the c-SiC grain should consist of equal quantity of Si and C atoms, but proposing the grain surfaces to be fully Si-terminated, leads to the fact, that all C atoms of the surface layer would be replaced by Si atoms. Therefore, the supplementary Si atoms would occupy a volume of $V_{\mathrm{s}}/2$. An other way to express the volume of the Si excess is by $2(0.5 - X) \times L^3 = (1 - 2X)L^3$. By combining both equations to $(1 - 2X)L^3 = V_s/2 = 3 \times L^2 \times D^{-1/3}$, the L can be written as

$$L(X) = \frac{3 \times D^{-1/3}}{1 - 2X} \tag{4.2}$$

This relation is plotted in Fig. 4.6(c) (red line) together with the data of L_{SiC} and X of HWCVD and PECVD films and shows a good agreement with the experimental data. Hence, assuming the c-SiC grains to be cubic and Si terminated, seems to be a valid simplified description of the material morphology, if the μc-SiC:H(n) film is highly crystallized.

Both, the hydrogen content as well as the Si excess decrease with decreasing total grain surface induced which is induced by larger crystalline SiC grains and are expected to terminate the surfaces. Therefore, the grain surfaces might be Si-H$_x$ (x = 1, 2, 3) terminated.

4.1.3. Electrical conductivity

At this point in the thesis, it possible to investigate the electrical conductivity of the unintentionally doped μc-SiC:H(n) material based on the detailed description of the material morphology that was studied in Sec. 4.1.1 and Sec. 4.1.2. The conductivity (σ) values of the films from the six series in Fig. 4.7 vary in the range of 10^{-13}-10^{-1} S/cm, although no doping gas was used during growth of any of the films. Oxygen and nitrogen are known donors for crystalline silicon carbide [75]. For μc-SiC:H(n), nitrogen is commonly used for *intentional* doping [8, 76–78] whereas intentional oxygen doping is lacking of reports in the literature. The oxygen content ([O]) and nitrogen content ([N]) in the films were determined from SIMS measurements for the samples of the series where the MMS gas flow rate was varied but the MMS gas concentration was kept constant at 0.3 % using HWCVD and PECVD. The obtained values for [O] and [N] are plotted as a function of σ in Fig. 4.8, where σ covers a range of 10^{-13}-10^{-3} S/cm. The values of [O] and [N] scattered around average values of $(1 \pm 1) \times 10^{19}$ at/cm^3 and $(5 \pm 2) \times 10^{19}$ at/cm^3, respectively, for the films which were grown by HWCVD. Both contents were higher for PECVD than for HWCVD films, but they also seemed to be unchanged around $(1 \pm 1) \times 10^{21}$ at/cm^3 for [O] and around $(3 \pm 1) \times 10^{19}$ at/cm^3 for [N]. Therefore, it can be excluded that the strong increase in conductivity arose from a variation in oxygen or nitrogen content. However, it cannot be excluded that one impurity atom or both might be responsible for the n-type conductivity in the films. The impurity concentrations of $\geq 10^{19}$ at/cm^3 can be considered to be high, although they seem to be some sort of background concentration. For comparison, the density of c-SiC is reported to be 9.68×10^{22} at/cm^3 in Ref. [127]. Possibly, storing the substrate carrier for PECVD in a N_2 gas flow box was not effective enough to avoid contamination by O and N from the atmosphere. The substrate carrier for HWCVD was stored in the load lock of the HWCVD chamber at a pressure in the order of 10^{-6} mbar. Further, the vacuum chambers themselves contain atmospheric residuals which might be another possible source of O and N contamination.

After having shown that potential donor concentrations were comparable over an electrical conductivity range of 10 orders of magnitude, certain morphological

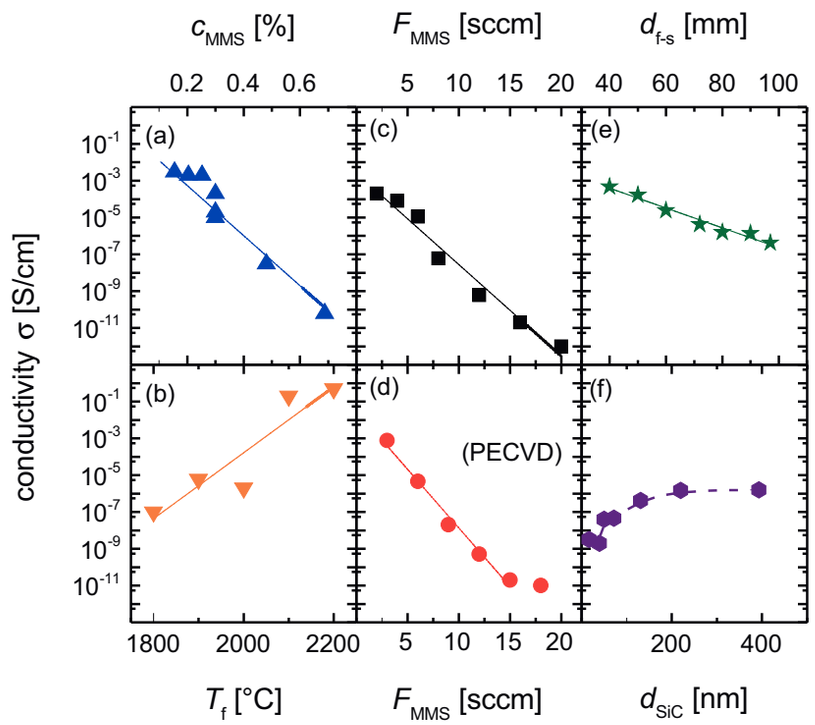

Figure 4.7.: *Lateral electrical conductivity σ of unintentionally doped μc-SiC:H(n) film series as a function of the following deposition parameters that were varied each series: (a) MMS gas concentration c_{MMS}, (b) filament temperature T_f, (c) MMS flow rate while keeping MMS gas concentration constant at 0.3 %, (d) MMS flow rate while keeping MMS gas concentration constant at 0.3 % using PECVD, (e) distance between filament and substrate $d_{f\text{-}s}$, and (f) film thickness d_{SiC}.*

properties should lead to the rise in electrical conductivity. In Fig. 4.9(a), the values of σ are plotted as a function of the intensity of the Si-C stretching mode from all six series. The values of σ increase with increasing $I_{\text{Si-C}}$. The σ increased by 3.7 orders of magnitude per 10^4 cm^{-1} for PECVD grown films, while it increased only by around 1.9 orders of magnitude per 10^4 cm^{-1} for HWCVD grown films. A similar separated alignment of data points from HWCVD and PECVD grown films can be

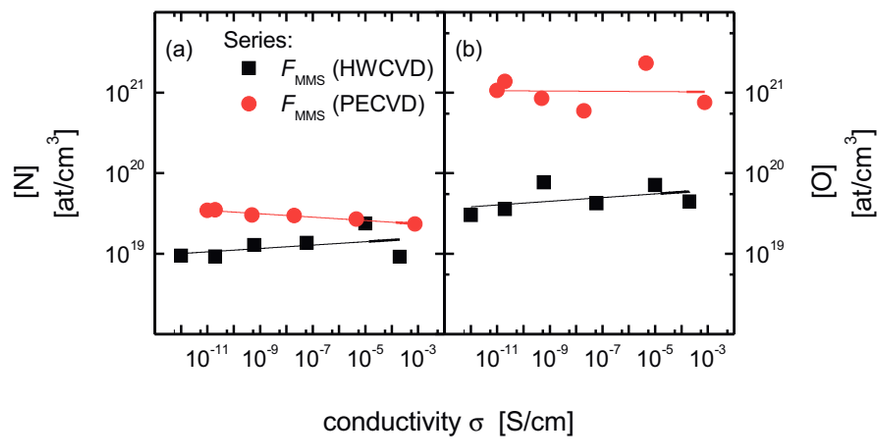

Figure 4.8.: *(a) Nitrogen content [N] and (b) oxygen content [O] determined by SIMS measurements as function of σ for the films from the F_{MMS} series using HWCVD or PECVD. Straight lines represent linear fits of the series with the corresponding color. Reproduced from Ref. [115], with the permission of AIP Publishing.*

observed in Fig. 4.9(b) where σ is plotted versus the grain size values from the F_{MMS} series (HWCVD and PECVD) as well as from the filament-substrate distance series. In this case, σ increases by about 1.1 orders of magnitude per nanometer of grain size for PECVD grown films while it increases only by about 0.2 orders of magnitude per nanometer for HWCVD grown films. Interestingly, the data of the $d_{\mathrm{f\text{-}s}}$ series are also following the trace of the data from the F_{MMS} series (HWCVD) which was not the case for the intensity of the Si-C stretching mode (Fig. 4.1(c,e)) and the deposition rates (Fig. 4.3(b)). Also in Fig. 4.9(c) all σ values correlate well with the values of the hydrogen content of the HWCVD grown films, i.e., including the films of the $d_{\mathrm{f\text{-}s}}$ series, where the conductivity decreased with increasing hydrogen content in the films. The data points from the PECVD grown films are again slightly off the trace of the data from the HWCVD grown films, but also show a decrease in σ with increasing [H]. In addition to the correlations between σ and the structural parameters and the hydrogen content, σ increased for increasing carbon fraction in Fig. 4.9(d).

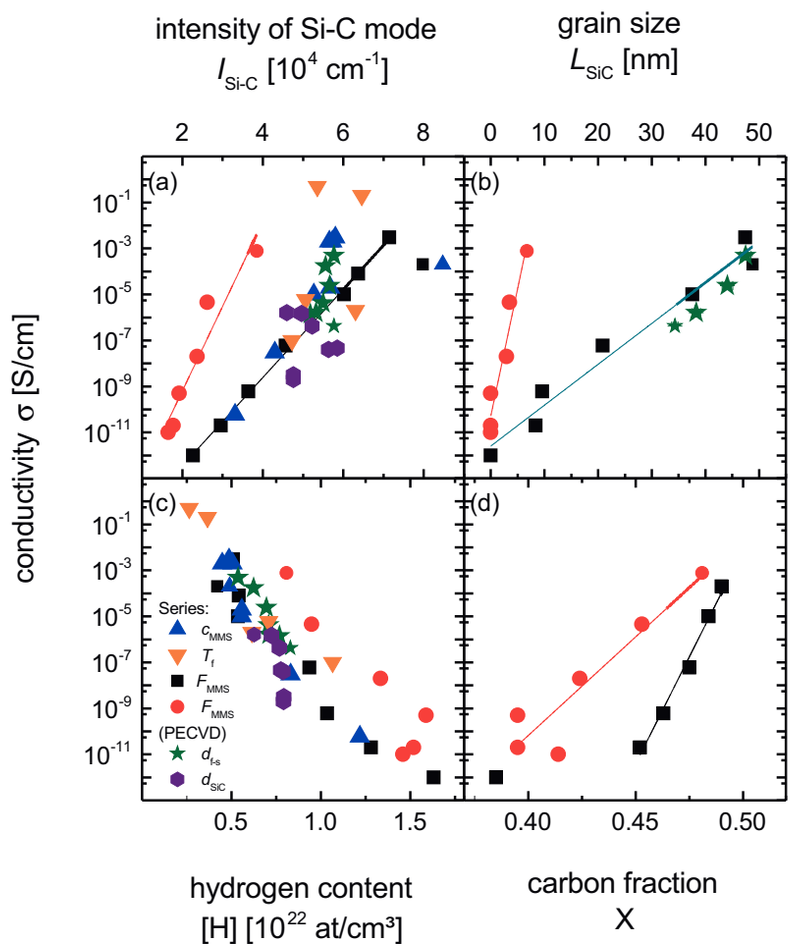

Figure 4.9.: *Lateral electrical conductivity σ of unintentionally doped μc-SiC:H(n) films as a function of (a) intensity of Si-C stretching mode $I_{Si\text{-}C}$ from FTIR spectroscopy, (b) XRD grain size L_{SiC}, (c) hydrogen content [H] derived from Si-H related modes form FTIR spectroscopy, and (d) carbon fraction X. Presented is the data from film series where the following deposition parameters were varied: MMS gas concentration c_{MMS}, filament temperature T_f, MMS flow rate F_{MMS} while keeping MMS gas concentration constant at 0.3 %, MMS flow rate F_{MMS} while keeping MMS gas concentration constant at 0.3 % using PECVD, distance between filament and substrate $d_{f\text{-}s}$, and film thickness d_{SiC}.*

Based on the correlations between the conductivity and different morphological properties in Fig. 4.9 and on reports from the literature, the following hypotheses for the origin of conductivity in unintentionally doped μc-SiC:H(n) are collected:

(i) An increased portion of stacking faults in SiC lattice might lead to lower σ, as it was reported in Ref. [61, 74] for p-type μc-SiC:H. More information about stacking faults in c-SiC and unintentionally doped μc-SiC:H(n) can be found in Ref. [112, 128]. Although it seems reasonable that a higher density of structural defects could hinder the electron transport in the material, none of the corresponding peaks at 33.6°or 38.0°was observed in the diffractograms in Fig. 4.2(a-c).

(ii) Hydrogen might passivate donors, as reported by several groups for c-SiC [129–131]. The groups calculated the passivation level from the drop in electron spin resonance (ESR) signal for nitrogen related paramagnetic states before and after hydrogenation of the c-SiC, and crosschecked it by measuring the charge carrier density. Qualitatively, the idea of donor passivation by hydrogen in the case of unintentionally doped μc-SiC:H(n) would be in good agreement with the decrease in σ for increasing [H] in Fig. 4.9(c), while [N] and also [O] remain practically unchanged. To verify or exclude hydrogen passivation of donor impurities, systematic ESR studies are necessary in future.

(iii) Large grain sizes improve the electronic transport in μc-SiC:H(n) films. Seto proposed a electrical transport model in 1975 for polycrystalline silicon where the conductivity increases with increasing grain size [132]. The theoretical model was in good agreement with experimental data from polycrystalline silicon films with 20 nm of average grain size which is in the order of magnitude of the grain sizes presented in this thesis.

In order to investigate the validity of the last hypothesis, charge carrier density (n), charge carrier mobility (μ), and the corresponding activation energies (E_{n},E_{μ}) were derived from combined temperature dependent measurements of electrical conductivity and thermopower. The resulting values are plotted as a function of grain size in Fig. 4.10 for both F_{MMS} series (HWCVD and PECVD). The n increased by 3 orders of magnitude with increasing L_{SiC} for the HWCVD grown films and by 2

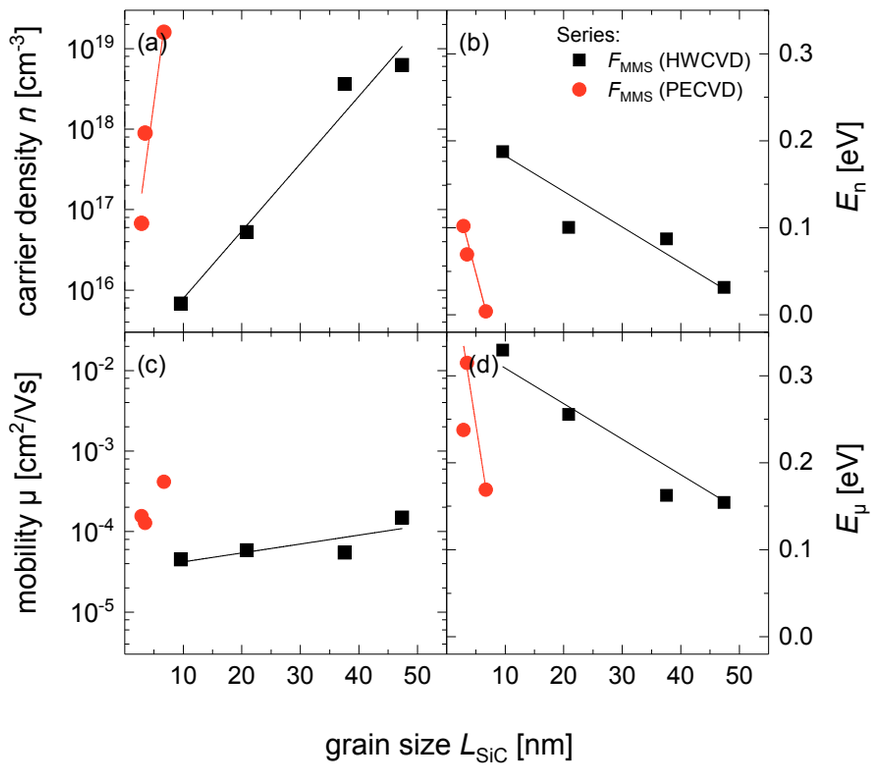

Figure 4.10.: *(a) Charge carrier density n, (b) charge carrier mobility μ, (c) activation energy of charge carrier density E_n, and (d) activation energy of charge carrier mobility E_μ as a function of grain size L_{SiC} for HWCVD and PECVD μc-SiC:H(n) samples from the F_{MMS} series. All values were derived from combined conductivity and thermopower measurements at 360 K. Straight lines represent linear fits of the series with the corresponding color. Reproduced from Ref. [115], with the permission of AIP Publishing.*

orders of magnitude for the PECVD grown films (Fig. 4.9(a)). Due to the microcrystalline character of the films, the material mainly consists of c-SiC grains with a high degree of ödisorder at heterogeneous grain boundaries as it was pictured in the past by transmission electron microscopy [9, 113, 126] and XRD [73, 74, 133]. It is known that for such polycrystalline materials a large number of defects can be present at

the grain boundaries, due to incomplete atomic bonding [134–136]. Therefore, electrons can be trapped in the defect states. The higher the trap density at the grain boundary the more electrons are trapped and form a depletion region which leads to a rise of potential barriers at the grain boundaries. More details about the electrical transport mechanisms in polycrystalline material can be found in Ref. [132, 137]. According to Seto's model, the average carrier concentration in a grain should consist of contributions from the depleted grain boundary region and the undepleted bulk region of the grain. Thus, for small grains, the high amount of depletion region causes a stronger reduction of the average n in the grain, whereas for larger grains the effect of the less depleted grain boundaries is smaller. The activation energy of n can be understood as average energy difference between bottom of the conduction band (E_{C}) and the Fermi level (E_{F}). Thus, the values represent effective E_{n} values. They decreased with increasing L_{SiC} (Fig. 4.9(b)) which supports the idea of an increased part of undepleted region in a grain which induces a shift of E_{C} towards lower energies while E_{F} remains unchanged. Concerning the mobility of the charge carriers, the values of μ increased slightly by less than one order of magnitude over the whole L_{SiC} for both deposition techniques (Fig. 4.9(c)) which might be related to the decrease in grain boundary density as the grain size increased by factor 5 for the HWCVD grown films and by factor 2 for the PECVD grown films. It is assumed that the activation energy of the mobility is the sum of E_{n} and the energy barrier height at the grain boundary. In Fig. 4.9(d) E_{μ} decreases with increasing L_{SiC}. As the slope of the linear fit of the data is around -4 meV/nm for E_{μ} as well as for E_{n}, the decrease in E_{μ} is dominated by the decrease in E_{n}. Consequently, the barrier height should remain unchanged. By extrapolating the fit of E_{n} in Fig. 4.9(b) for the HWCVD grown samples, E_{n} would become zero for a grain size of 55 nm. At this grain size, E_{μ} would correspond to roughly 125 meV which can be interpreted as the barrier height for the unintentionally doped μc-SiC:H(n) films from the F_{MMS} series using HWCVD. The barrier height would correspond to roughly 150 meV for the PECVD grown films, derived in the same way.

Although the data in Fig. 4.10 are in good agreement with the idea of change in undepleted regions in the material, the data is not in contradiction with the idea of hydrogen passivation of the donors. With increasing grain size the hydrogen content

decreases (Fig. 4.9(b,c)), thus the lower hydrogen content could lead to an increase in active donors which is reflected by the increase in obtained charge carrier density. Due to the increase in charge carrier density the Fermi-level shifts towards higher energies, which would explain the decrease in E_{n} in Fig. 4.10(b). The increase in charge carrier mobility and the decrease in its activation energy do not necessarily depend on the decrease in hydrogen content.

The increase in electrical conductivity of unintentionally doped μc-SiC:H(n) films, although no doping gas was used during the film growth, can be attributed to an increase in grain size or to a decrease in hydrogen content. The origin of the donor states is, however, unknown so far. It could be due to the presence of oxygen and nitrogen impurities in the films (Fig. 4.8) which could both give rise to donor states within the bandgap. The role of oxygen and nitrogen in μc-SiC:H(n) will be studied in Sec. 4.2.

4.1.4. Optical absorption coefficient

Beside the structural and the electrical properties, it is also important to know the optical properties of the unintentionally doped μc-SiC:H(n) films as the material will be used as window layer in SHJ solar cells in Chapt. 5. In Fig. 4.11 the PDS absorption coefficient (α) is plotted as a function of phonon energy (hν) which provides information about free-carrier absorption [138, 139], defect density [138] and optical bandgap [138] of the material. Presented are the α of the six series where the monomethylsilane (MMS) gas concentration (c_{MMS}) in the gas phase, the filament temperature (T_{f}), the MMS flow rate with constant c_{MMS} of 0.3 % (HWCVD and PECVD), the distance between filament and substrate ($d_{\mathrm{f\text{-}s}}$), and the film thickness (d_{SiC}) were varied. As for all α in this thesis, a refractive index of 2.5 was used to derive α from the measured PDS data. From ellipsometer measurements (not shown) it was derived that the refractive index is in the range of 2.4-2.8 for the samples of this thesis. A variation of the refractive index from 2.0 to 3.0 for the calculation of α showed only very small effect on the absolute values of α. The series can be grouped into three groups according to their spectra of the absorption coefficient. First, the c_{MMS} and F_{MMS} (HWCVD and PECVD) series can be grouped

together as α decreased in the low energy range ($<$ 2 eV) with increasing F_{MMS} or c_{MMS} while it increased in the high energy range ($>$ 2 eV) with increasing F_{MMS} or c_{MMS} in Fig. 4.11(a,c,d). Second, the spectra from the T_{f} series form a group where α increases over the entire range of the phonon energy for increasing T_{f} in Fig. 4.11(b). It should be noted that a transition from semiconductor behavior ($T_{\mathrm{f}}\leq$2000 °C) to metal behavior ($T_{\mathrm{f}}\leq$2200 °C) takes place, as indicated by the strong increase in the overall α and flattened slope with increasing T_{f}. Third, the series of $d_{\mathrm{f\text{-}s}}$ and d_{SiC} in Fig. 4.11(e,f) can be grouped together, because no clear trend of α as a function of $d_{\mathrm{f\text{-}s}}$ or d_{SiC} can be observed.

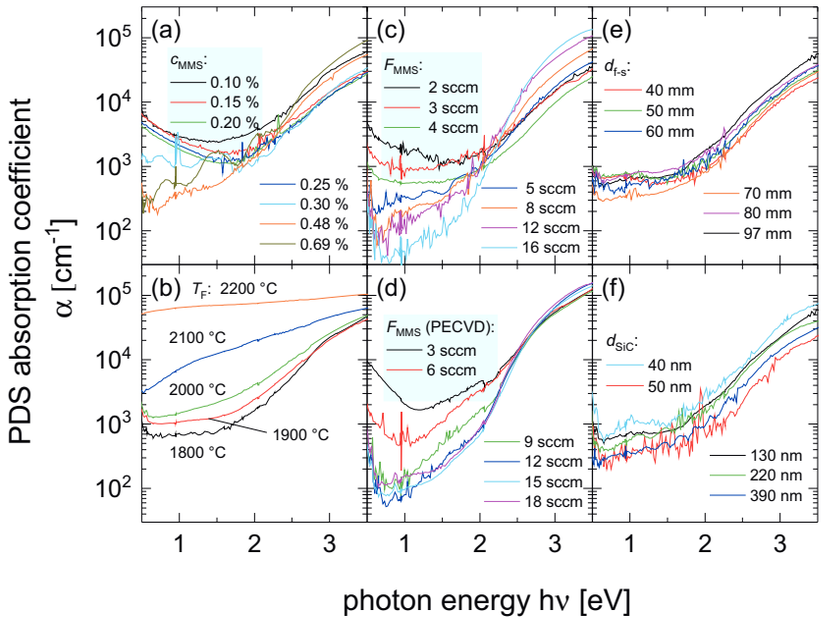

Figure 4.11.: *PDS absorption coefficient α as a function of photon energy $h\nu$ of unintentionally doped μc-SiC:H(n) film series where the following deposition parameters were varied: (a) MMS gas concentration c_{MMS}, (b) filament temperature T_f, (c) MMS flow rate F_{MMS} while keeping MMS gas concentration constant at 0.3 %, (d) MMS flow rate F_{MMS} while keeping MMS gas concentration constant at 0.3 % using PECVD, (e) distance between filament and substrate $d_{f\text{-}s}$, and (f) film thickness d_{SiC}.*

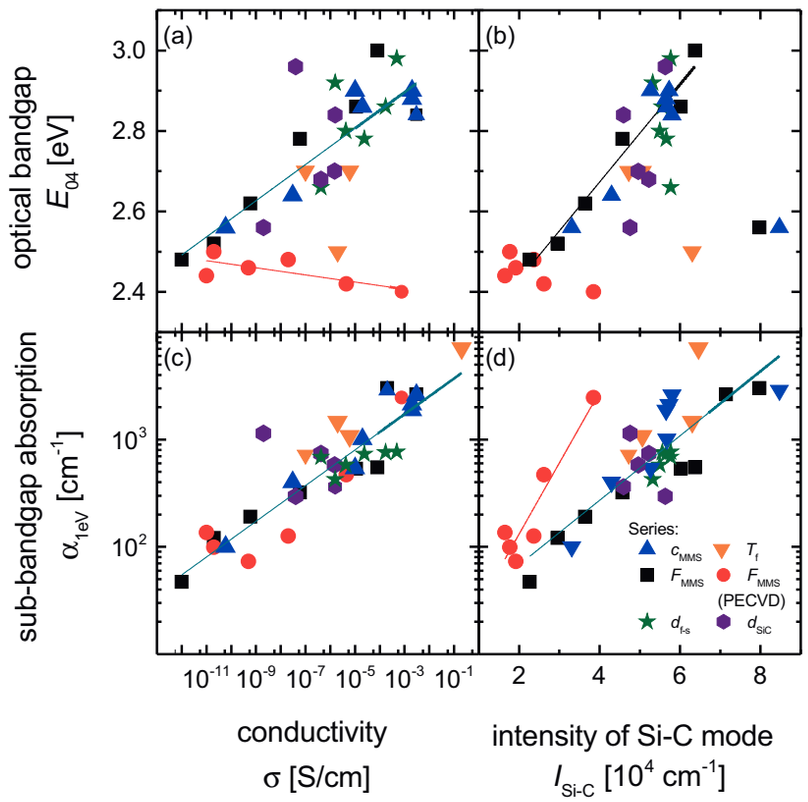

Figure 4.12.: *(a,c) Optical bandgap E_{04} and (b,d) sub-bandgap absorption α_{1eV} as a function of lateral electrical conductivity σ and of intensity of Si-C stretching mode $I_{Si\text{-}C}$ from FITR. Presented is the data from film series where the following deposition parameters were varied: MMS gas concentration c_{MMS}, filament temperature T_f, MMS flow rate F_{MMS} while keeping MMS gas concentration constant at 0.3 %, MMS flow rate F_{MMS} while keeping MMS gas concentration constant at 0.3 % using PECVD, distance between filament and substrate $d_{f\text{-}s}$, and film thickness d_{SiC}.*

As the optical properties of the three groups differ strongly, it is necessary to quantify α and correlate it to the intensity of the Si-C stretching mode ($I_{\text{Si-C}}$) from FTIR spectroscopy and electrical conductivity (σ) to draw relations to the microstructure and the electrical conductivity. To quantify the data of α, the optical bandgap

(E_{04}) is derived from the energy where α becomes 10^4 cm^{-1} and the free carrier absorption coefficient ($\alpha_{1\text{eV}}$) is obtained at 1 eV phonon energy. The values of E_{04} are correlated to σ and to $I_{\text{Si-C}}$ in Fig. 4.12(a) and Fig. 4.12(b), respectively, for values for all six series. It can be seen that the E_{04} increases for the HWCVD grown films with increasing $I_{\text{Si-C}}$ (Fig. 4.12(b)). The linear fit of the data from the F_{MMS} (HWCVD, black line) exhibits an average increase in E_{04} of 0.1 eV per 10^4 cm^{-1}. This increase in E_{04} can be explained by the higher order in microstructure of the μc-SiC:H(n) material which reduces defect density near the energy band edges [8]. Interestingly, the films around $I_{\text{Si-C}}$ of 2×10^4 cm^{-1} that were suggested to be amorphous in Sec. 3.3, due to vanishing 3C-SiC peak in the diffractograms, possess an E_{04} of around 2.5 eV which is still sufficiently transparent and of interest for window layer in a silicon heterojunction solar cell. The E_{04} values of the PECVD grown films seem to scatter in the range of 2.4-2.5 eV independently of $I_{\text{Si-C}}$ and, consequently, also independently of σ (Fig. 4.12(a)). The E_{04} values increase in average (cyan line) around 0.04 eV per order of magnitude of σ for all the films of the five HWCVD grown series.

The values of $\alpha_{1\text{eV}}$ of all six series correlated with σ in Fig. 4.12(c). The linear fit of all data points (cyan line) has a slope of 0.17 orders of magnitude of $\alpha_{1\text{eV}}$ per order of magnitude of σ. This seems to be a general dependency for unintentionally doped μc-SiC:H(n) material independent of deposition method or deposition parameter that was varied. According to Smith [138] the free carrier absorption coefficient is proportional to the charge carrier density (n) by

$$\alpha = \frac{\mathrm{q}^3\lambda^2 n}{4\pi^2\epsilon_0 c^3 n_{\mathrm{j}} m^{*2}\mu}, \tag{4.3}$$

where q is the elementary charge, λ the wavelength, ϵ_0 the vacuum permittivity, n_{j} the refractive index, m^* the effective mass, and μ the charge carrier mobility. The values of $\alpha_{1\text{eV}}$ also correlate with the values of $I_{\text{Si-C}}$. The $\alpha_{1\text{eV}}$ increases with increasing $I_{\text{Si-C}}$. The average increase is higher for PECVD grown films. It is 0.7 cm^{-1} per 10^4 cm^{-1} for PECVD grown films while it is only 0.3 cm^{-1} per 10^4 cm^{-1} for HWCVD grown films. As the free carrier absorption coefficient is proportional to the charge carrier density, the stronger increase in $\alpha_{1\text{eV}}$ for PECVD grown films with increasing $I_{\text{Si-C}}$ can be related to the stronger increase in charge carrier density (Fig. 4.10(a))

with increasing grain size as compared to HWCVD grown films.

4.2. Role of oxygen and nitrogen in the films

The microstructure represents a major characteristic of the material that strongly influences the opto-electronic properties. However, several groups [8, 9, 120] found indications for the existence of more mechanisms, based on (i) films with large opto-electronic differences but similar structural properties, and (ii) reproducibility issues or strong scattering in the data. The latter is illustrated in Fig. 4.13, where σ is plotted as a function of T_{f} and of T_{H}. It can be observed that the values suffer from a significant scattering. Therefore, it is necessary to search for mechanisms additionally to the microstructure, in order to control the opto-electronic properties and to avoid irreproducibility.

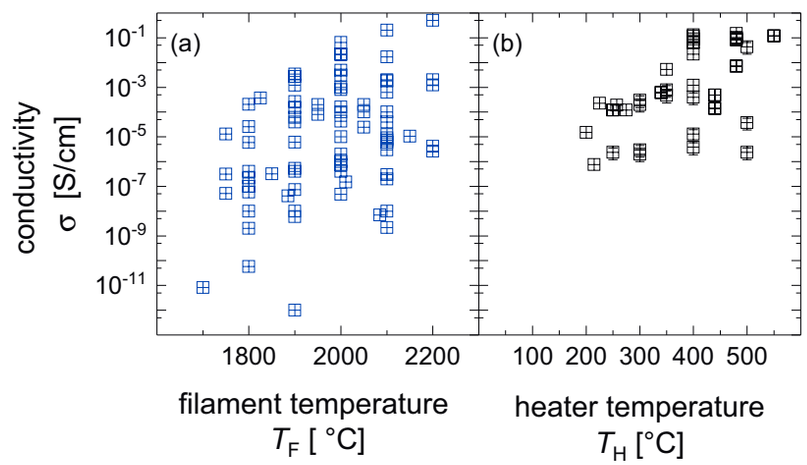

Figure 4.13.: *Scattering of the data of lateral electrical conductivity σ as a function of (a) filament temperature T_f and (b) heater temperature T_H. The order of the depositions is random*

Nitrogen (N) is widely used for n-type doping for crystalline silicon carbide (c-SiC) since several decades, because its ionization energy is only 48-54 meV [75, 140]. In

comparison, the donor levels for oxygen (O) are located much deeper in the energy bandgap with ionization energies of 129-950 meV [75, 141]. For this reason, there is only a small number of studies involving O in c-SiC(n). Research groups [9, 55, 120] speculated in the case of HWCVD grown μc-SiC:H(n) that O or N impurities from contamination could influence the opto-electronic properties, but so far no direct relation could be found. As for the depositions only SiC precursor gases (e.g., MMS, SiH_4 and CH_4) and hydrogen gas have been used, unintentional doping could arise from atmospheric residuals that are present in the chamber. Contamination of the gas themselves was excluded by the usage of gas purifiers in Ref. [9]. Interestingly, both residual atoms are already known to increase the σ of amorphous silicon (a-Si:H) [142] and microcrystalline silicon (μc-Si:H) [82, 143–145].

4.2.1. Atmospheric residuals

In order to investigate the effect of the atmospheric residuals, a series was processed were the contamination level of the chamber was varied. The chamber is exclusively used for depositing unintentionally doped μc-SiC:H(n), so that contamination from depositions of other materials can be excluded. As shown in Fig. 4.14(a), the HWCVD chamber was opened and then pumped down for 16h. This procedure resulted in an increase of the base pressure (p_{base}) compared to before the chamber opening and served as measure to contaminate the chamber. The p_{base} is presented as a function of the accumulated deposition time (t_{acc}) of several three-hours-depositions of μc-SiC:H(n). Starting with a p_{base} of almost 10^{-5} mbar, the p_{base} needed in total 20 h of repetitive deposition runs and permanent pumping to decrease below 10^{-7} mbar. After a second chamber opening the p_{base} increased again abruptly and decreased with further deposition runs. In Fig. 4.14(b) σ of the films is plotted as a function of t_{acc}. A similar trend as for the p_{base} can be observed. The σ is highest after the chamber opening, i.e. 2×10^{-2} S/cm and 1×10^{-1} S/cm. Then, it decreases with increasing t_{acc} down to 1×10^{-5} S/cm. The HWCVD deposition parameters were kept the same for all samples.

Four samples were highlighted in Fig. 4.14. They represent: (A) the first deposition after the first chamber opening and overnight heating at 350 °C, (B) the third

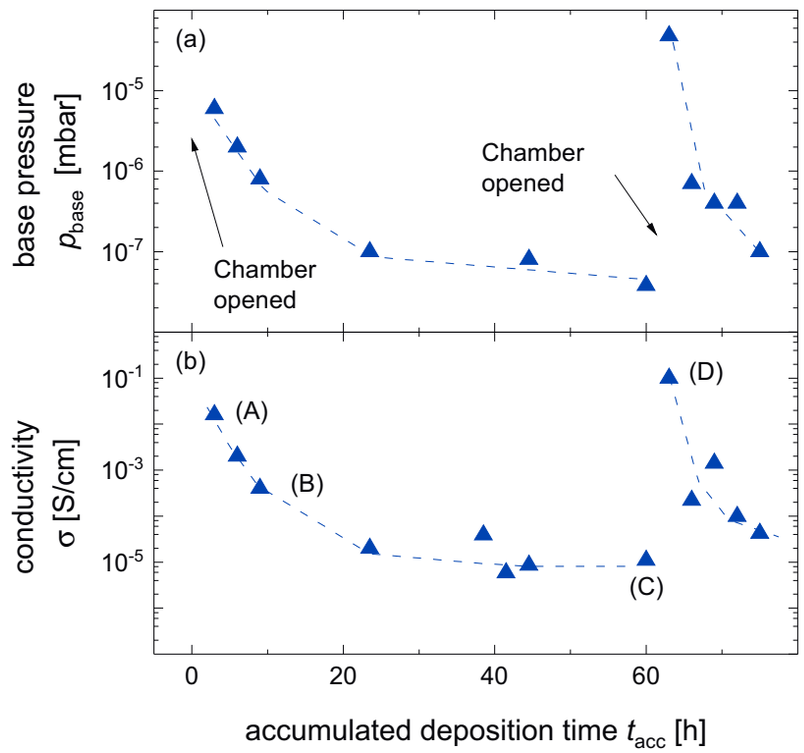

Figure 4.14.: *(a) Base pressure p_{base} in the HWCVD vacuum chamber before the deposition and (b) lateral electrical conductivity σ as a function of the accumulated deposition time t_{acc}. The deposition chamber was opened twice, indicated at t_{acc} of 0 h and 60 h. The presented samples were all deposited with the same deposition parameters. The highlighted samples represent (A) the first deposition after the first chamber opening and overnight heating at 350 °C, (B) the third deposition after the first chamber opening, (C) a deposition after several weeks (t_{acc} = 60 h) after the first chamber opening, and (D) the first deposition directly after the second chamber opening without any bake-out treatment.*

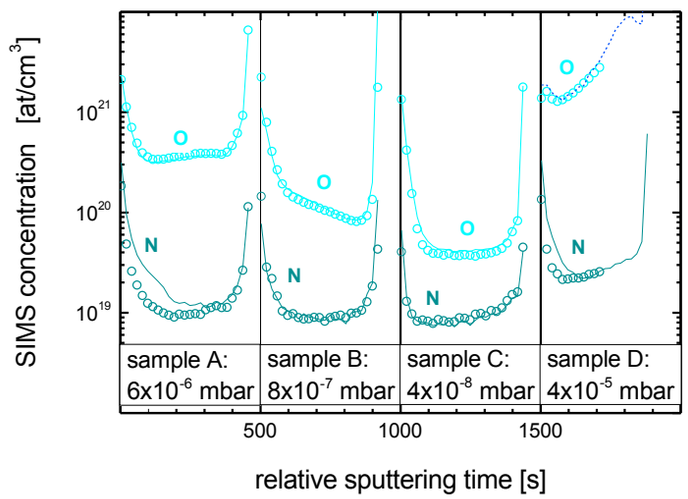

Figure 4.15.: *Oxygen concentration [O] and nitrogen concentration [N] depth profiles measured by SIMS of HWCVD grown μc-SiC:H(n) films. Relative sputtering times of 0 s, 500 s, 1000 s, and 1500 s represent the film surfaces of the corresponding samples. Similarly, the relative sputtering times 500 s, 1000 s, 1500 s, and 2000 s represent the interfaces to the glass substrate of the corresponding samples. The indicated samples represent (A) the first deposition after the first chamber opening and overnight heating at 350 °C, (B) the third deposition after the first chamber opening, (C) a deposition after several weeks (t_{acc} = 60 h) after the first chamber opening, and (D) the first deposition directly after the second chamber opening without any bake-out treatment. All deposition parameters were kept the same.*

deposition after the first chamber opening, (C) a deposition after several weeks (t_{acc} = 60 h, $p_{base} < 10^{-7}$ mbar) after the first chamber opening, and (D) the first deposition directly after the second chamber opening without any bake-out treatment. All four samples were investigated by SIMS measurements to find the oxygen content ([O]) and nitrogen content ([N]) in the films. The results are presented in Fig. 4.15 in form of depth profiles as a function of arbitrary relative sputtering time. The [O] clearly decreased with decreasing p_{base} whereas the [N] rather remained at the same

level. The [O] ranged from $(6 \pm 2) \times 10^{19}$ at/cm^3 to $(4 \pm 2) \times 10^{21}$ at/cm^3 while [N] only ranged between $(1 \pm 1) \times 10^{19}$ at/cm^3 and $(4 \pm 1) \times 10^{19}$ at/cm^3. Hence, the SIMS measurements show that the contamination by oxygen plays a dominant role in this set of samples.

4.2.2. Heater temperature

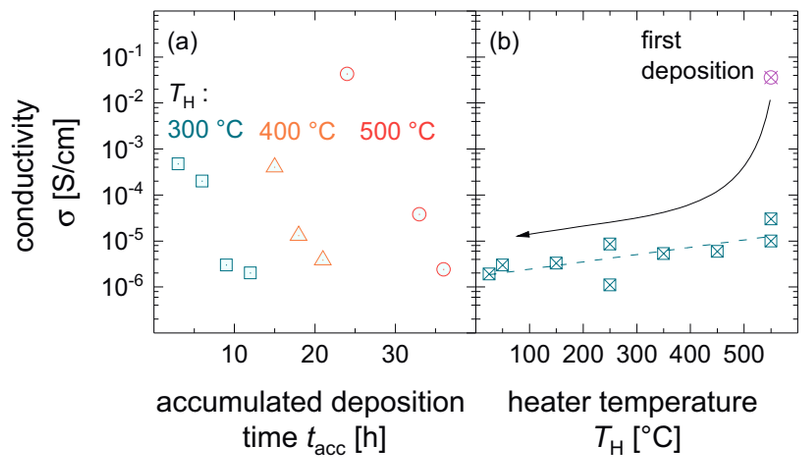

Figure 4.16.: *Lateral electrical conductivity σ as a function of (a) accumulated deposition time t_{acc} and (b) heater temperature T_H. The HWCVD deposition order was chosen carefully. In (a), the T_H was increased from 300-500 °C after 3-4 depositions at the same T_H. In (b), T_H was continuously decreased from 550 °C to 23 °C, where the heater was switched off. The first deposition is highlighted in pink. Both series were performed after a chamber opening and overnight heating of 350 °C.*

In two following control experiments, high temperatures were applied to the HWCVD chamber, in order to intentionally reduce the [O] by baking out the residuals from the chamber walls. It was assumed that the main source of O are the chamber walls adsorbing O when the chamber is opened. In the first control experiment, the T_{H} was increased twice after a couple of depositions at the same T_{H}. The corresponding σ values are presented as a function of t_{acc} in Fig. 4.16(a). It can be

observed, that starting with T_{H} of 300 °C the σ values first dropped with increasing t_{acc} similar to the experiment before, but could be recovered after increasing the T_{H} to 400 °C. Then, the σ dropped again while maintaining the T_{H} constant. This behavior could be observed once more with T_{H} of 500 °C. The order of T_{H} was reversed for the second control experiment. It started with the highest possible T_{H}, i.e. 550 °C, to decrease the T_{H} stepwise down to room temperature (heater switched off), and to return to 550 °C at the end. The resulting σ are plotted as a function of T_{H} in Fig. 4.16(b), where the first deposition at 550 °C is highlighted with a pink circle. It can be observed, that the σ dropped from 4×10^{-2} S/cm to 6×10^{-6} S/cm between the first and the second deposition. Except for the σ of the film from the first deposition, the σ ranged from 1×10^{-6} to 9×10^{-6} S/cm over the entire T_{H} range. Compared to the σ data with T_{H} in random order (Fig. 4.13), the σ values with T_{H} in chosen order followed a certain pattern (Fig. 4.16(a)) or scatter only by up to one order of magnitude over the whole T_{H} range. This indicates that atoms from atmospheric residuals are present at the HWCVD chamber walls even after several depositions and have a strong impact on the electrical properties of the μc-SiC:H(n) films. Dasgupta et al. reported in Ref. [120] of nearly unaltered structural properties in TEM dark field micrographs of μc-SiC:H(n) films that were deposited at different substrate temperatures. According to the results presented in Fig. 4.15, it is most probable that increased oxygen impurity concentrations also play a major role for the samples of Fig. 4.16, leading to higher electrical conductivity. It seems that oxygen contamination of the chamber lasts for several depositions. Preferably the maximum system temperature should be applied during pre-depositions, in order to minimize oxygen incorporation during sample depositions. Although the electrical conductivity is more reproducible after high temperature pre-conditioning of the chamber, the electrical conductivity only slightly overcomes 10^{-6} S/cm which was postulated by Lambertz et al. [51] to be a rough minimum for doped layer materials in silicon heterojunction solar cells.

4.2.3. Controlled oxygen incorporation

Alternatively to opening the chamber, another method to introduce oxygen impurities in the μc-SiC:H(n) films - in a more controlled way - would be to add a gas

during the deposition that contains O. With the PECVD chamber, it was possible to introduce O_2 gas and H_2O vapor through a needle valve. In addition, it was also possible to introduce CO_2 gas through a mass flow controller. With the HWCVD chamber, it was not possible to test these gases. The amount of O_2 and H_2O that was added to the PECVD chamber through the needle valve was adjusted before the deposition. It was controlled by the displayed pressure which is denoted here as leak pressure (p_{leak}). The p_{leak} was varied between 10^{-8} mbar and 10^{-4} mbar, where for 10^{-8} mbar the needle valve was closed and p_{leak} is equal to p_{base}. In Fig. 4.17(a) it can be observed that the σ increased slightly from 3×10^{-6} S/cm to 8×10^{-6} S/cm with increasing p_{leak} of O_2. The σ dropped drastically down to 10^{-11} S/cm for $p_{leak} > 2 \times 10^{-6}$ mbar. The reason for this strong change in σ seemed to be a transition in material from μc-SiC:H(n) with O impurities into silicon oxycarbide alloy. Indications for this transition towards silicon oxycarbide were the presence of the Si-O stretching mode at 1080 cm^{-1} in the FTIR spectrum (not shown), a doubled deposition rate, and α smaller than 10^4 cm^{-1} over the whole measurable energy range. The higher deposition rate indicates that a significant amount of additional atoms, i.e., oxygen atoms, were incorporated in the films. The low α in combination with the low σ is typical for oxygen rich silicon oxides [51]. Increasing the p_{leak} of H_2O increased the σ continuously up to 1×10^{-4} S/cm, but dropped it down to 10^{-11} S/cm for $p_{leak} > 2 \times 10^{-5}$ mbar, as it is plotted in Fig. 4.17(a). Again, the material seemed to have turned into silicon oxycarbide. The indications are similar as before: presence of the Si-O stretching mode in the FTIR spectrum (not shown), strong increase of the deposition rate by factor three to seven, and α smaller than 10^4 cm^{-1} over the whole measurable energy range in combination with low σ. The strong decrease of σ after inlet of minimum amount of CO_2 indicates that the material probably turned into silicon oxycarbide directly, when CO_2 was introduced, although the smallest F_{CO2} was only 0.06 sccm which was controlled by a 3 sccm mass flow controller. All other indications, that were observed before with O_2 and H_2O, were comparable. It can be summarized that introducing a gas containing O did not lead to the same high σ values as after chamber opening that were shown in Sec. 4.2.1. Only one of the samples produced by using H_2O had a similar σ namely 4×10^{-1} S/cm, but this value could not be reproduced. Another reason for not reaching similar σ values as after opening of the HWCVD chamber arise from the

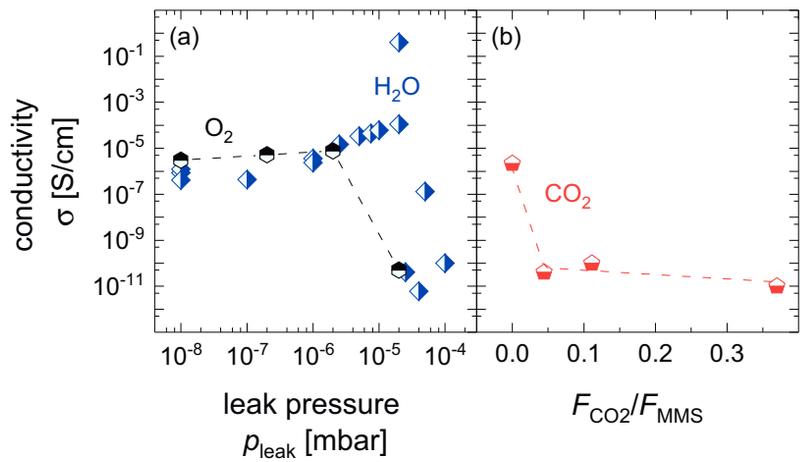

Figure 4.17.: *Oxygen incorporation during PECVD μc-SiC:H(n) growth by adding pure O_2, H_2O or CO_2 gas during the deposition process. In (a), the lateral electrical conductivity σ is plotted versus the set leak pressure p_{leak} before the deposition using O_2 or H_2O. At the p_{leak} of 1×10^{-8} mbar the leak was closed. In (b), the σ is plotted versus the CO_2 gas flow rate F_{CO2} as ratio to the MMS gas flow rate F_{MMS}.*

difference in deposition method or/and chamber. In Fig. 4.8(b) it was observed that the oxygen content in the PECVD grown films was with in average 10^{21} at/cm^3 already at a very high level, although no gas containing O was added. For HWCVD grown films, only the sample D which was processed directly after chamber closing exhibited an oxygen content in the 10^{21} at/cm^3 range (Fig. 4.5). Conventional HWCVD grown films had an O content in the order of 10^{19} at/cm^3 (Fig. 4.8(b)). It might be that the background O content which is in the order of 1at.% is already near the critical impurity concentration where doping becomes alloying. Further, it might be speculated at this point in the thesis that the high O content (Fig. 4.8(b)) in PECVD films might be the reason for similarly high electrical conductivity as for HWCVD grown films although the grain size is significantly smaller than for HWCVD grown films. The source of oxygen might be substrate carrier which was systematically stored in a nitrogen flow box for films that were grown using PECVD while the substrate carrier was kept in the load-lock for films that were grown using

HWCVD. The oxygen concentration in the nitrogen flow box is much higher than in the vacuum ($\approx 10^{-6}$ mbar) of the load-lock. The base pressure of the PECVD and the HWCVD chambers were both in the 10^{-8} mbar range. Future works should investigate the σ transition between silicon carbide and silicon oxycarbide in more detail, in order to permit a reliable reproduction of the σ maximum. Another investigation in the future could be the effect of controlled addition of gas that contains oxygen during the HWCVD growth of μc-SiC:H(n) which was not covered in this thesis.

4.2.4. Controlled nitrogen incorporation

Also nitrogen doping was investigated, in order to complete the picture of the mechanisms responsible for the electrical transport in μc-SiC:H(n). So far, hexamethyldisilazane [8, 12], ammonia [77], and pure nitrogen [147] have been successfully used for doping of μc-SiC:H(n). In this work, pure nitrogen was added to HWCVD and PECVD depositions. In agreement with the references, the σ increased with increasing nitrogen flow rate F_{N2} for HWCVD grown μc-SiC:H(n) and increased with increasing p_{leak} for PECVD grown μc-SiC:H(n). The conductivity results are presented in Fig. 4.18(a) and in Fig. 4.19, respectively. The highest value of σ was 2 S/cm using HWCVD, while it was 1×10^{-3} S/cm by using PECVD. In Fig. 4.18(a) it can be observed that the doping by nitrogen atoms started to saturate for flow rates above 5 sccm. SIMS measurements were performed for some of the HWCVD samples, in order to determine the oxygen content and the nitrogen content in films with different σ. In Fig. 4.18(b) both contents are plotted as a function of the F_{N2}. The nitrogen content rose continuously by two orders of magnitude up to 2×10^{21} at/cm^3. This time, the oxygen content remained unchanged around an average value of $(8\pm4)\times10^{19}$ at/cm^3 whereas in Fig. 4.15 for the p_{base} series (Sec. 4.2.1) the trends of nitrogen content and oxygen content were the other way around.

4.2.5. Model for electrical transport

In this work, it was shown that the σ of μc-SiC:H(n) films can be increased independently by increasing the grain size, by increasing the oxygen content, or by

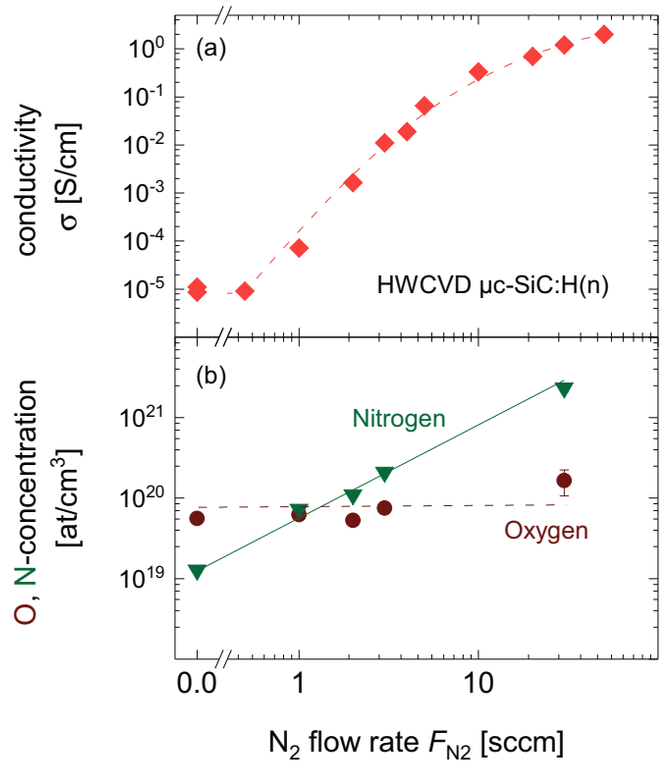

Figure 4.18.: *(a-b) Nitrogen incorporation during the HWCVD µc-SiC:H(n) growth by adding pure nitrogen gas (N_2) during the deposition process. In (a), the σ is presented as a function of the nitrogen gas flow rate F_{N2} and in (b), the corresponding [N] and [O] determined by SIMS measurements are plotted versus F_{N2}. Reproduced from Ref. [146], with the permission of AIP Publishing.*

increasing the nitrogen content of the material. In the following the model for the electrical transport in μc-SiC:H(n), that was introduced in Sec. 4.1.3, is reviewed and expanded based on the additional insights from the p_{base} series (Sec. 4.2.1) and from the F_{N2} series (Sec. 4.2.4).

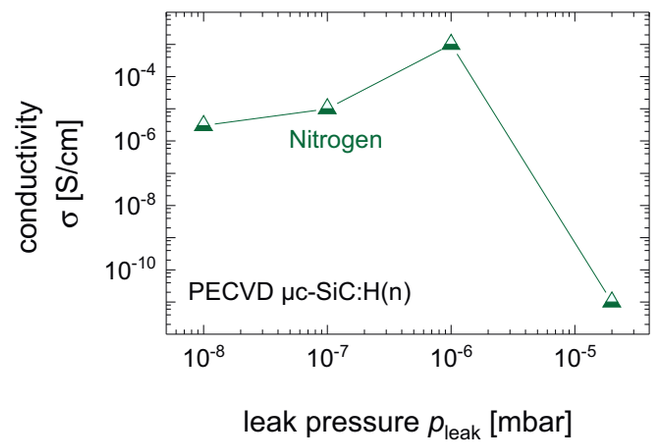

Figure 4.19.: *Nitrogen incorporation during the PECVD µc-SiC:H(n) growth by adding pure nitrogen gas (N_2) during the deposition process. The nitrogen incorporation is controlled by the leak pressure (p_{leak}) before the deposition. The lateral electrical conductivity σ is plotted as a function of p_{leak}. At the p_{leak} of 1×10^{-8} mbar the leak was closed.*

The microstructure, the hydrogen content, and the impurity concentration of the films are not decoupled. The total impurity concentration of the samples from the F_{MMS} (HWCVD) series, from the p_{base} series and from the F_{N2} series are plotted as a function of grain size in Fig. 4.20(a). The grain size ranged from 0-49 nm for the F_{MMS} series while the total impurity concentration scattered around an average value of $(6 \pm 3) \times 10^{19}$ at/cm^3. In this case, the increase of grain size probably arises from the decrease in the r_{depo} in the range of 0.04-0.76 Å/s. In the case of the p_{base} series, and the F_{N2} series, the F_{MMS} was kept constant (= 6 sccm) and consequently, the r_{depo} remained unchanged around 0.13 ± 0.01 Å/s for the whole grain size range. However, the grain size decreased with increasing total impurity concentration which suggests that an increase of the total impurity concentration hinders the crystal growth and induces defects to the material. There seems to be no quantitative difference for the decrease in grain size by increasing oxygen content or increasing nitrogen content.

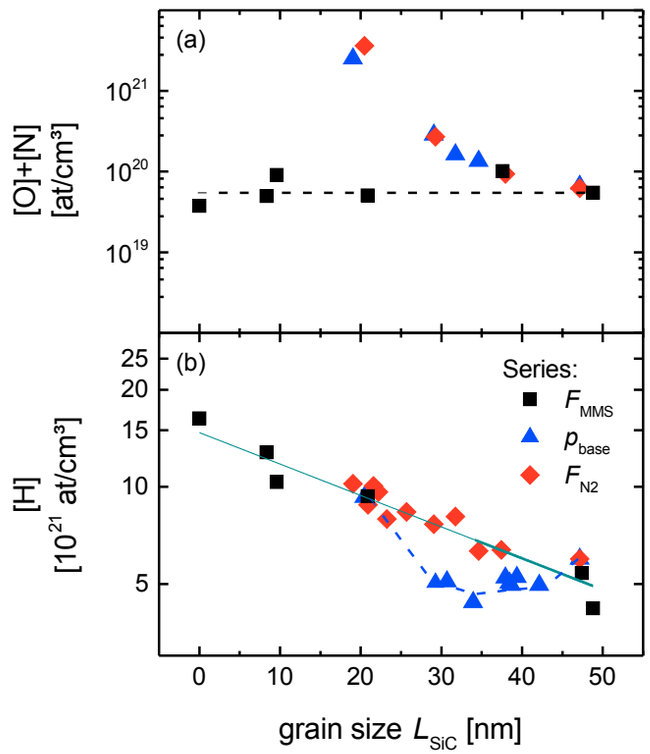

Figure 4.20.: *(a) Total impurity concentration of oxygen and nitrogen [O]+[N] and (b) hydrogen content [H] plotted as a function of the average grain size L_{SiC} for HWCVD μc-SiC:H(n) samples from the F_{MMS} series, from the p_{base} series, and the F_{N2} series. The blue straight line represents a linear fit of the data points from the F_{MMS} and the F_{N2} series. The black dashed line serves as a guide for the eye and represents the average total impurity concentration for the F_{MMS} series.*

Another interesting aspect is the correlation of hydrogen content and grain size. In Fig. 4.20(b) the hydrogen content of samples from the F_{MMS} (HWCVD), the p_{base}, and from the F_{N2} series are plotted as a function of grain size. The values of hydrogen content from the F_{MMS} (HWCVD) and the F_{N2} series decreased with increasing grain size and can be fitted using $[\mathrm{H}] = 10^{a \times L_{SiC}+b}$ where the fit parameters are a =

-0.0097 and b = 22.2. This empirical relation seems to be valid for films produced with different r_{depo} (F_{MMS} series) and different nitrogen contents (F_{N2} series), but not for films with different oxygen contents (p_{base} series) for which the values of hydrogen content scatter around 5×10^{21} at/cm^3. As it was shown in Sec. 4.1.2 the c-SiC grains might be terminated by Si-H which explains the correlation between hydrogen content and grain size for the F_{MMS} series. This argument also holds for the data of the F_{N2} series in Fig. 4.20(b), but not for the p_{base} series. Hydrogen did not increase with increasing L_{SiC} for the p_{base} series, likely due to additional occupation of grain boundary sites by oxygen in substitution to hydrogen which is supported by a low solubility of oxygen atoms in c-SiC ($\approx 10^{14}$ cm^{-3} [148]). In comparison nitrogen atoms are very soluble in c-SiC ($\approx 10^{21}$ cm^{-3} [75]). It is still unsolved if an increase of electrical conductivity can arise from larger grain size or from smaller hydrogen content. Both hypotheses were introduced in Sec. 4.1.3: (i) hydrogen might passivate donors or (ii) larger grain sizes might decrease the effective activation energy of the charge carrier density. As hydrogen content and grain size seem to depend on each other, a clear statement is not possible here.

A model for electrical transport mechanisms in μc-SiC:H(n), based on the above mentioned observations and on simplified energy band diagrams, is proposed in Fig. 4.21. In Fig. 4.21(a) the potential barriers in the conduction band are illustrated for the reference with the lowest oxygen and nitrogen content in this work. An increase in grain size results in a smaller grain boundary density and therefore less potential barriers, which is illustrated in Fig. 4.21(b). The corresponding data for Fig. 4.21(a,b) are shown in Fig. 4.10 and the respective discussion is given in Sec. 4.1.3.

The increase in oxygen content and nitrogen content increases σ similarly. To investigate the role of oxygen and nitrogen in μc-SiC:H(n) in more detail the charge carrier density and mobility an their corresponding activation energies are determined by combined conductivity and thermopower measurements. The values for n, μ, E_{n}, and E_{μ} are plotted in Fig. 4.22 as function of oxygen content for films from

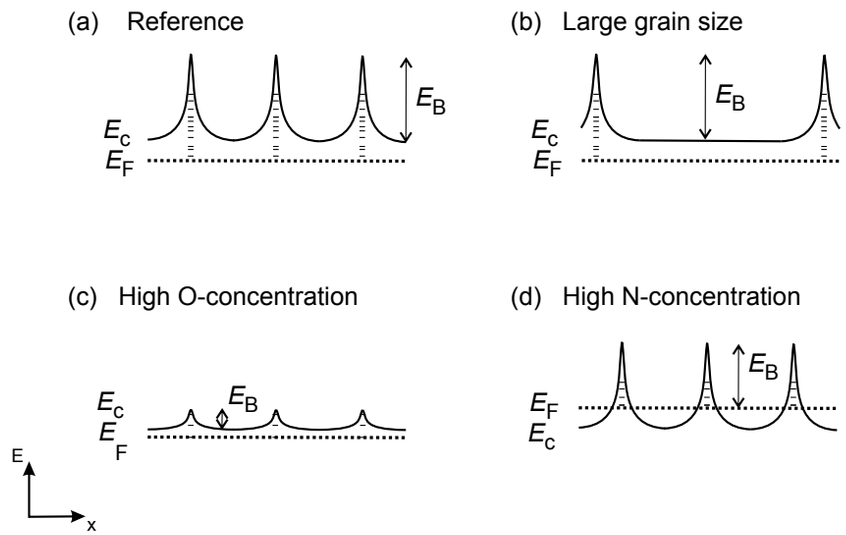

Figure 4.21.: *Illustrations of possible, simplified energy band diagrams of HWCVD grown μc-SiC:H(n) with (a) lower [O], lower [N] and moderate average grain size L_{SiC}, (b) lower [O], lower [N] but large L_{SiC}, (c) high [O], lower [N] and moderate L_{SiC}, and (d) low [O], high [N] and moderate L_{SiC}. Reproduced from Ref. [146], with the permission of AIP Publishing.*

the p_{base} series and as a function of nitrogen content for the films from the F_{N2} series, because the SIMS measurements in Fig. 4.15 and Fig. 4.8 have shown that either oxygen or nitrogen dominates the total impurity concentration by more than one order of magnitude in difference. From Fig.4.22(a) it can be derived that the incorporation of both impurities atoms leads to an increase in charge carrier density which is typical for donors. However, for impurity concentrations of $\geq 5 \times 10^{19}$ at/cm^3 the increase of the values for n is saturated around 5×10^{19} cm^{-3} for oxygen while the increase continues for nitrogen. In Fig. 4.22(a) a dashed line is added to represent 100 % doping efficiency, where n([X]) = [X], with [X] as impurity concentration. On average, the doping efficiency was 19 ± 3 % over the investigated nitrogen content range whereas the doping efficiency varied between 1 % and 26 % for oxygen content.

The saturation in n for increased oxygen content arises from a limited decrease of E_{n} in Fig. 4.22(d) which remains around 0.05 ± 0.01 eV for increased oxygen contents. As the ionization energy of oxygen in c-SiC is 129-950 meV [75, 141] whereas is only 48-54 meV for nitrogen in c-SiC [75], it might be possible that the position of the Fermi-level is ultimately determined by the nitrogen donor states. Consequently, the creation of new states below the Fermi-level has only low doping efficiency. An increase of the nitrogen content leads to zero E_{n} which is an indication for the μc-SiC:H(n) material to become degenerated.

The values for μ increased similarly for increasing oxygen content and increasing nitrogen content by 3 orders of magnitude over the entire range of impurity concentration. The highest value for μ was 9×10^{-2} cm^{-2}/Vs for the μc-SiC:H(n) film with the highest oxygen content. As the grain size decreased by factor 2 (Fig. 4.20), the increase of μ cannot be related to the grain size like for films from the F_{MMS} series (Sec. 4.1.3). In this case the effective height of the potential barriers at grain boundaries seems to decrease with increasing impurity concentration, because E_{μ} decreases in Fig. 4.22(d) while E_{n} remains unchanged for impurity concentrations of $\geq 5 \times 10^{19}$ at/cm^3 in Fig. 4.22(c). In the case of oxygen content, it might be that the flattening of the barriers arises from a possible decrease of trap density at the grain boundaries. This decrease of trap density might be induced by oxygen related bonds. In the case of elevated nitrogen content, the description of the charge carrier mobility might be more complicated, because the materials become degenerated and the Fermi-level rises inside the conduction band. The effective barrier height is decreased and according to Sommer et al. [137] inter grain tunneling becomes the dominant scattering mechanism at the grain boundaries for degenerately doped polycrystalline semiconductors and also Kozlovskyi et al. [149] concluded that the charge transfer in nanocrystalline SiC through energy barriers should be realized by tunneling as illustrated in Fig. 4.21(d).

In summary, the electrical conductivity of μc-SiC:H(n) films can be increased (i) by larger grain size which decreases the amount of depleted region and thus decreases the activation energy of the charge carriers; (ii) by higher oxygen content which mainly decreases the potential barriers at the grain boundaries and thus increases

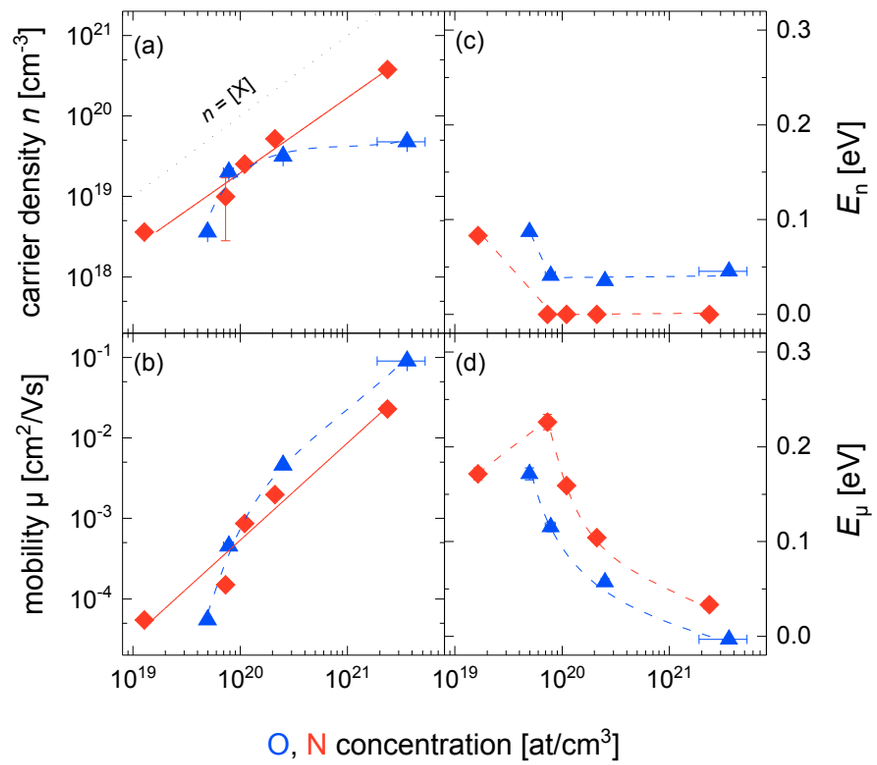

Figure 4.22.: *(a) Charge carrier density n, (b) charge carrier mobility μ, (c) activation energy of charge carrier density E_n, and (d) activation energy of charge carrier mobility E_μ as a function of the O-content for the films of the p_{base} seris and as a function of the N-content for the films of the F_{N2} series. All values were derived from combined conductivity and thermopower measurements at 360 K. Dashed lines serve as guide for the eye. The black dashed line indicates where the doping efficiency would be 100 %, which means that n = [X], where [X] represent either the [O] or the [N]. Reproduced from Ref. [146], with the permission of AIP Publishing.*

the charge carrier mobility; and (iii) by higher nitrogen content which rises the Fermi-level into the conduction band and thus increases the charge carrier density as well as the charge carrier mobility.

4.2.6. Electrical conductivity beyond state-of-the-art

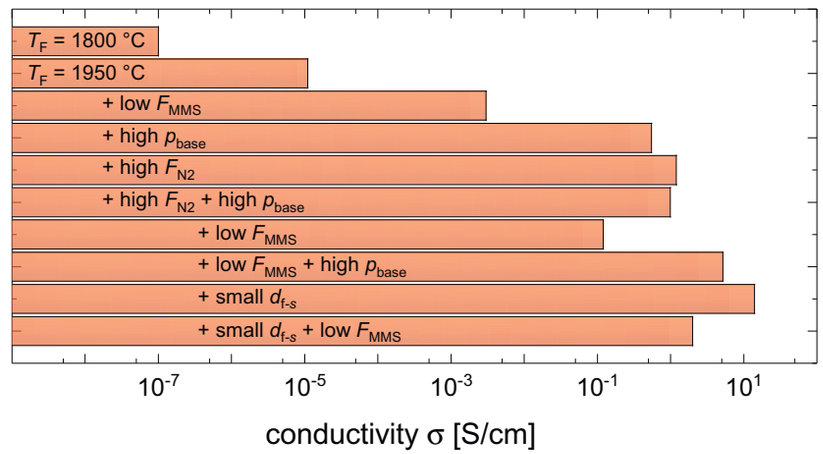

Figure 4.23.: *Maximization of the lateral electrical σ by combining deposition parameters that increase σ individually*

Based on all the introduced effects that the HWCVD growth conditions have on σ of μc-SiC:H(n), a further improvement of σ was carried out. In Fig. 4.23 the results of the σ optimization steps are summarized. The first improvement of the σ arises from increasing T_f from 1800 °C to 1950 °C which improved the σ from 1×10^{-7} S/cm to 1×10^{-5} S/cm. The increase in σ can be attributed to the higher order in microstructure and larger grain size [80]. Therefore, all other films of the optimization process were also deposited at a T_f of 1950 °C. A lower F_{MMS} of only 3 sccm (corresponds to c_{MMS} = 0.15 %) improved the σ by another 2 orders of magnitude and can be attributed a further increase in order of the microstructure (Fig. 4.9). However, using the standard F_{MMS} of 6 sccm in combination with a high p_{base} increases the σ strongly up to 6×10^{-1} S/cm due to oxygen incorporation (Fig. 4.14 and Fig. 4.5). Using the standard F_{MMS} of 6 sccm in combination with a high F_{N2} increases the σ up to 1 S/cm. Implementing high oxygen content and high nitrogen content simultaneously, by combining high p_{base} and high F_{N2}, did not increase the σ further. This result is in agreement with the assumption introduced in

the previous section that creation of new oxygen donor states below the Fermi level has only low doping efficiency and that the charge carriers predominately originate from nitrogen donor states which have a lower ionization energy than the oxygen donor states. Also combining low F_{MMS} and high F_{N2} did not increase σ further which is not yet understood. But, using a high p_{base} for oxygen incorporation in combination of low F_{MMS} improved σ to 5 S/cm. Finally, the highest value of σ in this work was obtained by reducing $d_{\mathrm{f\text{-}s}}$, which was presented as alternative to increase the grain size in Sec. 3.3, parallel to high F_{N2} and standard F_{MMS} (= 6 sccm). The measured value was 14 S/cm. To the best of our knowledge this is the highest σ value achieved for μc-SiC:H(n). A decrease of F_{MMS} for the last combination of deposition parameters only gave rise to 2 S/cm.

4.2.7. Optical absorption coefficient

Last, it will also be discussed how increasing oxygen and nitrogen content influence the optical properties of μc-SiC:H(n). The corresponding optical absorption coefficients α measured by PDS are plotted as a function of photon energy in Fig. 4.24(a)+(b). As for all α in this thesis, a refractive index of 2.5 was used to derive α from the measured PDS data. From ellipsometer measurements (not shown) it was derived that the refractive index is in the range of 2.4-2.8 for the samples of this thesis. A variation of the refractive index from 2.0 to 3.0 for the calculation of α showed only very small effect on the absolute values of α. In Fig. 4.24(a)+(b) the overall α increases with increasing impurity concentration for both types of impurity concentration. It even increases that strongly, that it is not possible to derive the optical bandgap for all films by conventional analysis methods, i.e., E_{04} (photon energy at $\alpha(E_{04}) = 10^4$ cm^{-1}) or Tauc plot, due to very small slopes of α in the range of 2-3 eV and due to $\alpha > 10^4$ cm^{-1} over the whole energy range for the films with very high impurity concentrations. Therefore, the optical absorption (A) in a 30 nm film was calculated by integrating the spectra of α over the conventional AM1.5 sun spectrum and using the Lambert-Beer law, i.e.,

$$A = \frac{\int \mathrm{AM1.5}(\lambda) \times (1 - \exp[-\alpha(\lambda) \times 30\ \mathrm{nm}])\mathrm{d}\lambda}{\int \mathrm{AM1.5}(\lambda)\mathrm{d}\lambda}, \tag{4.4}$$

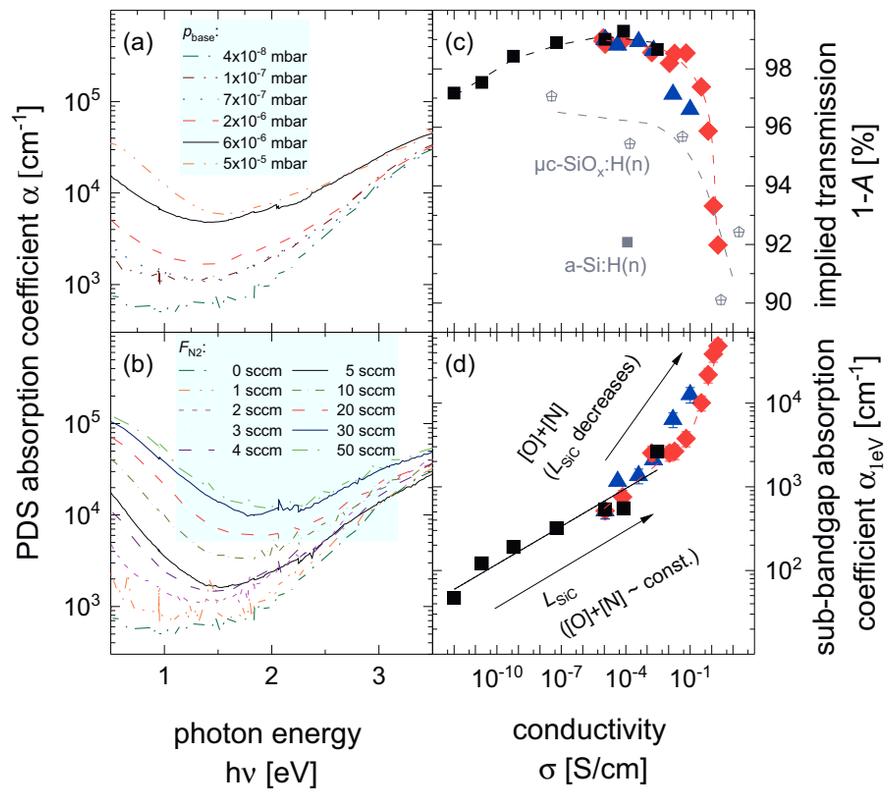

Figure 4.24.: *(a-b) PDS absorption coefficient α as function of the photon energy $h\nu$ for HWCVD grown µc-SiC:H(n) deposited with (a) different oxygen content [O] (p_{base} series) and (b) different nitrogen content [N] (F_{N2} series). In (c), the implied transmission 1-A of the AM1.5 sun spectrum through a 30 nm thick µc-SiC:H(n) layer is calculated using Lambert-Beer's law and plotted versus the σ for the films of the p_{base} series (blue triangles) and for the F_{N2} series (red rhombuses). The values the F_{MMS} series (black squares) and of 30 nm thick a-Si:H(n) and µc-SiO$_x$:H(n) layers are also added for comparison. In (d), the sub-bandgap absorption α_{1eV} is plotted as a function of the σ for the samples of the p_{base} series, for the F_{N2} series and for the F_{MMS} series. The straight black line represents the linear fit of the F_{MMS} data points whereas all the dashed lines only serve as guide to the eye. Reproduced from Ref. [146], with the permission of AIP Publishing.*

The thickness of 30 nm was chosen, because it is a realistic thickness for the implementation of μc-SiC:H(n) as window layer in a SHJ solar cell. In Fig. 4.24(c) the implied transmission 1-A is plotted as a function σ for films with increasing L_{SiC} and constant [O]+[N] (F_{MMS} series) as well as for films with decreasing L_{SiC} but increasing [O]+[N] (p_{base} and F_{N2} series). The implied transmission of the films from the F_{MMS} series increases by 2 % for increasing σ, whereas it decreases by 7 % with increasing σ for films from the p_{base} and F_{N2} series. This can be explained by a lower defect density for larger L_{SiC} that shifts the α spectrum to lower α. Hence, the highest values for 1-A of 99.0 % were found for films with large L_{SiC} and low total impurity concentration. The corresponding σ values range from 9×10^{-6} - 4×10^{-4} S/cm for such high implied transmission. The values for typical a-Si:H(n) and μc-SiO$_x$:H(n) films were added to Fig. 4.24(c) for comparison. The deposition conditions of these films can be found in Ref. [150]. The highest value for 1-A was 97.1 % at a σ of 10^{-8} S/cm for the μc-SiO$_x$:H(n) films, while increasing the σ decreased the implied transmission. The value for 1-A was 92.1 % at a σ of 10^{-4} S/cm for the a-Si:H(n) film. Hence, μc-SiC:H(n) offers the highest implied transmission of all silicon thin film materials. In addition to the implied transmission, the sub-bandgap absorption coefficient α_{1eV} is plotted as a function of the σ in Fig. 4.24(d). Overall, the α_{1eV} increased with increasing σ which can be interpreted as increase of free carrier absorption caused by the strong increase of the charge carrier density over the whole σ range. It can be observed that the strength of the increase in α_{1eV} for the films of the F_{MMS} series is lower than the increase for the other two series. The different slopes are also observed with α_{1eV} versus n (not shown). Thus, the n cannot be the only property influencing the α_{1eV}. A possible explanation for the lower slope of the data from the F_{MMS} series could be that the increase of n is accompanied by an increase of E_{04}, i.e., also by an increase of the effective E_{g} which lowers α over the whole energy range. Since the E_{g} decreases with increasing n for the two other series, it could be a plausible explanation for stronger enhancement of the free carrier absorption with increasing n.

5. Silicon carbide in silicon heterojunction solar cells

In this chapter, the feasibility and the potential of implementing HWCVD grown μc-SiC:H(n) in silicon heterojunction (SHJ) solar cells is discussed. The main focus in this chapter lies on the implementation of highly transparent μc-SiC:H(n) without deteriorating the passivation layer. In the first section, PECVD grown intrinsic amorphous silicon oxides (a-SiO_x:H(i)) were used to passivate the c-Si surfaces of the tested structures, whereas for the second section, the surfaces were passivated by ultra-thin silicon dioxide (SiO_2) which was grown wet-chemically. In both sections, the influence of the HWCVD deposition parameters on the passivation quality and on the SHJ solar cell performance are analyzed.

5.1. Silicon carbide in a-SiO_x:H(i) passivated SHJ solar cells

The combination of large bandgap and sufficiently high electrical conductivity makes μc-SiC:H(n) a promising material for low parasitic absorption loss in the window layer of SHJ solar cells. In the last chapter, HWCVD and PECVD grown μc-SiC:H(n) materials were compared. It was concluded that the HWCVD technique provides a μc-SiC:H(n) material with higher transparency at similar conductivity values as compared to the PECVD technique. It was further concluded that a high hydrogen (H) radical density is needed during the film growth to provide an optimum balance of high transparency and high electrical conductivity in the films (Fig. 4.24(c)). At the same time, however, the high amount of H radicals results in an

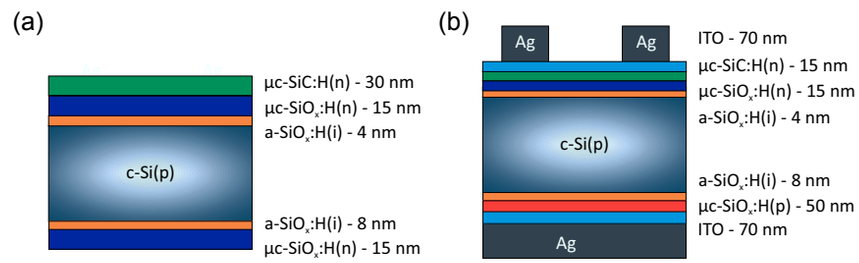

Figure 5.1.: *Schematic illustrations of (a) passivation test structure and (b) SHJ solar cell structure on flat p-type silicon wafer using a-SiO$_x$:H(i) as passivation layer.*

etching of the c-Si wafer surfaces. These surfaces are usually passivated by intrinsic amorphous silicon (a-Si:H(i)) which is also very sensitive to H etching (a-Si:H(i)) [79, 151, 152]. In this first section, it is studied how to implement μc-SiC:H(n) in a a-SiO$_x$:H(i) passivated SHJ solar cell. According to Einsele et al. [153], the quality of a-Si:H(i) and a-SiO$_x$:H(i) passivation decreases if the substrate is annealed at a too high temperature, due to effusion of the H atoms from the interface passivation. They reported that for a-Si:H(i) passivation τ_{eff} started to degrade from 250 °C whereas the critical temperature was shifted to 400 °C for a-SiO$_x$:H(i) with an oxygen (O) content of 5 %. This shift was ascribed to a higher bonding energy of the Si-H bonds due to the presence of back bonded O in the films.

5.1.1. Effect of silicon carbide deposition on a-SiO$_x$:H(i) passivation

A first approach consists of protecting the a-SiO$_x$:H(i) passivation layer from etch-off by a 15 nm thick n-type microcrystalline silicon oxide (μc-SiO$_x$:H(n)) layer. The μc-SiO$_x$:H(n) layer suits well the optical and electronic performance of the final device, as the μc-SiO$_x$:H(n)/a-SiO$_x$:H(i) layer combination was already successfully used in SHJ solar cells [49, 50, 154]. A passivation test structure consists of a symmetric μc-SiO$_x$:H(n)/a-SiO$_x$:H(i)/c-Si(p)/a-SiO$_x$:H(i)/μc-SiO$_x$:H(n) stack depite the different i-layer thicknesses, so that a deterioration of the passivation quality during the HWCVD process can be related to the μc-SiO$_x$:H(n)/a-SiO$_x$:H(i)/c-Si

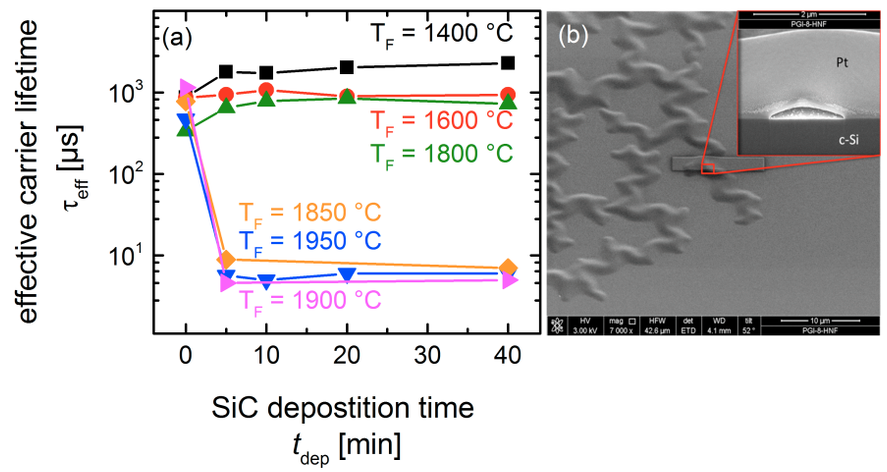

Figure 5.2.: *Influence of filament temperature T_f during HWCVD process on effective carrier lifetime τ_{eff} of test structure presented in Fig. 5.1(a): (a) τ_{eff} versus accumulated deposition time t_{depo} and (b) SEM images of blistering in top and cross-section view. The values for τ_{eff} correspond to τ_{eff} at a photo-carrier density of 10^{15} cm^{-3}. Reproduced from Ref. [155], with the permission of Thin Solid Films.*

layer stack. The test structure for investigating the passivation quality and the corresponding solar cell structure are illustrated in Fig. 5.1. Flat Si wafers were used for this entire section of the thesis. As the lateral conductance of the μc-SiC:H(n)/μc-SiO_x:H(n)/a-SiO_x:H(i) layer stack is insufficient, a 70 nm thick indium tin oxide (ITO) layer is used to collect the generated charge carriers at the front contacts.

By measuring the thickness of μc-SiO_x:H(n) on glass substrate before and after 40 min of μc-SiC:H(n) deposition at a filament temperature (T_f) of 2100 °C, it was found that the thickness of μc-SiO_x:H(n) remained almost unchanged during the HWCVD process. This demonstrates that μc-SiO_x:H(n) persists the H etching. After this pre-experiment the passivation quality of the test structure which is illustrated in Fig. 5.1(a) was tested. The effective carrier lifetime (τ_{eff}) correspond to the value at a photo-carrier density of 10^{15} cm^{-3} and was measured after different accumulated μc-SiC:H(n) deposition times (t_{depo}). The first value of τ_{eff} was always measured

after 5 min of t_{depo} and the last value after 40 min of t_{depo}, which would correspond to the deposition time of a nominal 30 nm thick μc-SiC:H(n) layer. The experiment was performed for T_{f} ranging from 1400 °C to 1950 °C. The τ_{eff} remained at a high level of about 1 ms after 5 min of t_{depo} for T_{f} of 1400-1800 °C, but τ_{eff} dropped to below 10 μs for T_{f} of 1850-1950 °C in Fig. 5.2(a). Prolonging the deposition did not change τ_{eff} anymore for both temperature ranges. A strong blistering could be observed by eye for some of the test structures with τ_{eff} below 10 μs. The repetition of the experiment with 1800 °C and 1850 °C confirmed the previous results that a narrow transition region between 1800 °C and 1850 °C exists where 5 min of HWCVD are sufficient to degrade the passivation of the wafer surface severely, even though the passivation layer was protected against H etching by the 15 nm thick μc-SiO$_x$:H(n) layer.

The heat sources during the HWCVD process are the heater and the hot filaments. In order to investigate their influence on τ_{eff}, the T_{f} as well as of the heater temperature (T_{H}) were varied. The results are presented in Fig. 5.3, where the τ_{eff} is plotted as a function of accumulated annealing duration (t_{anneal}) for different configurations of temperatures and passivation test structures. The shortest t_{anneal} was 1 min and longest was 40 min. In Fig. 5.3(a) a-SiO$_x$:H(i)/c-Si and a-Si:H(i)/c-Si passivation test structures without μc-SiO$_x$:H(n) layer were exposed to the heat of the filaments with T_{f} of 1200 °C and of the heater with T_{H} of 250 °C, by leaving out all the process gases. The τ_{eff} decreased slightly, but remained in the millisecond range for both passivation layers. In Fig. 5.3(b-c) the same sample structures were also exposed to T_{f} of 2100 °C. In this case, the τ_{eff} of the a-Si:H(i)/c-Si structure decreased to 100 μs whereas for a-SiO$_x$:H(i)/c-Si the τ_{eff} remained at 2 ms after 40 min. These results are in agreement with Ref. [153], where Einsele et al. observed a critical substrate temperature of 400 °C for the used a-SiO$_x$:H(i) passivation and 250 °C for a-Si:H(i). The experiment with T_{f} of 2100 °C was repeated with additional μc-SiO$_x$:H(n) cover layer on top of the passivation layer. The resulting trace of τ_{eff} is similar to the values without capping layer. In the case of a-SiO$_x$:H(i) passivated samples, the τ_{eff} first decreased within the first 5 min of t_{anneal} and then increased up to about the initial value for τ_{eff}. The origin of this phenomenon is not yet understood. Up to this point none of the presented results show that an

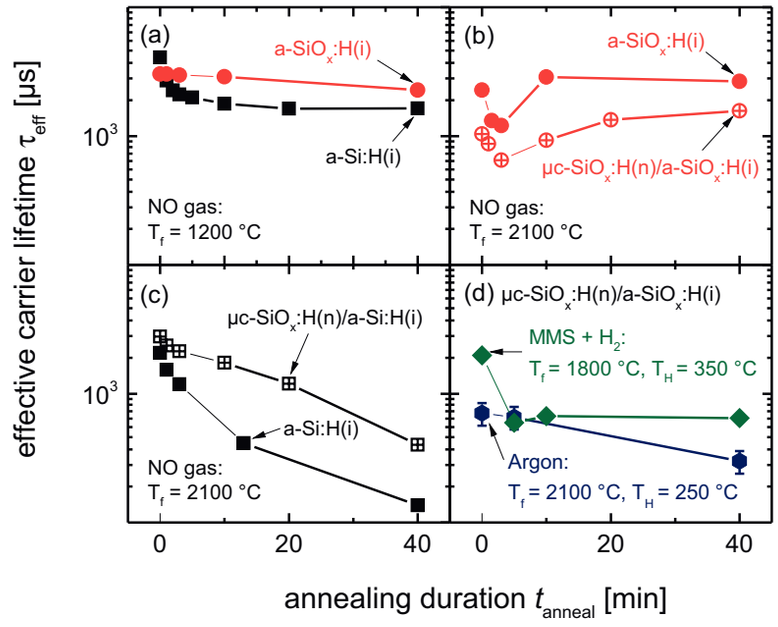

Figure 5.3.: *Effect of thermal radiation in ultra-high vacuum on the symmetric test structures (μc-SiO$_x$:H(n)/)a-SiO$_x$:H(i)/c-Si(p) and (μc-SiO$_x$:H(n)/)a-Si:H(i)/c-Si(n) test structure: (a) filament temperatures T_f of 1200 °C and (b-c) T_f of 2100 °C. In (b) a μc-SiO$_x$:H(n)/a-SiO$_x$:H(i)/c-Si(p) test structure was exhibited to 2100 °C of T_f using argon instead of the process gases. In (d) the μc-SiO$_x$:H(n)/a-SiO$_x$:H(i)/c-Si(p) test structure was processed with process gases (MMS+H$_2$) at a heater temperature T_H of 350 °C and T_f of 1800 °C. The T_H in (a-c) was 250 °C. Partially reproduced from Ref. [155], with the permission of Thin Solid Films.*

overheating of the passivation layer could be responsible for the severe degradation of τ_{eff} in Fig. 5.2(a) within 5 min. In order to take also convective heat transfer into account, the μc-SiO$_x$:H(n)/a-SiO$_x$:H(i)/c-Si structure was heated by T_{f} of 2100 °C, but this time with Argon gas in the chamber at a pressure of 75 Pa as for the experiment presented in Fig. 5.2. The τ_{eff} is shown in Fig. 5.3(d) and decreased slightly this time, but it does not reproduce the drop below 10 μs that was observed in Fig. 5.2(a) before. In total, it is difficult to estimate the real substrate tempera-

ture. Therefore, knowing that an increase of 50 °C of T_f lead to a drop of τ_{eff} from millisecond range to microsecond range, the experiment was repeated with process gases and T_f of 1800 °C, but with T_H increased by 100 °C from 250 °C to 350 °C using the μc-SiO$_x$:H(n)/a-SiO$_x$:H(i)/c-Si test structure. The resulting τ_{eff} dropped from 2 ms to 0.6 ms within the first 5 min, but remained in the range of 0.6-0.7 ms for longer deposition durations. Hence, none of the experiments introducing higher heat exposures of the test structures could reproduce the drop in τ_{eff} below 10 μs within 5 min. Consequently, no indication could be found that the passivation is severely deteriorated by an overheating of the test structure which would lead to effusion of H from the interface passivation.

After having excluded H etching from high H radical density and H effusion due to high substrate temperature as origin of the severe deterioration of the passivation (Fig. 5.2(a)), another mechanism must be responsible. In the SEM image in Fig. 5.2(b) the blistering is shown in top view and cross section view which was exclusively observed for samples where $T_f > 1800$ °C lead to $\tau_{eff} < 10$ μs. It might be that the blistering is induced by agglomeration of atomic H from the gas phase. The H radical concentration in the gas phase increases with a power law of T_f [117, 156] which leads to an increased etching of the surface and should also lead to an increased in-diffusion of H atoms through the layers towards the c-Si interface. The amount of H, that reaches the c-Si interface, is defined by the diffusion coefficients and the thicknesses of the layers, and also by the initial amount of H atoms that are adsorbed at the surface of the top most layer. Beyer et al. reported in Ref. [157, 158] on an agglomeration of H at the c-Si interface due to a low diffusion coefficient for H in c-Si (10^{-15} - 10^{-12} cm^2/s [159]). As the amount of H at the surface strongly depends on T_f, a narrow transition region of only 50 °C, as observed in this work, seems to be reasonable. In addition, Beyer [157, 158] showed that whenever atomic H diffuses into micro-voids molecular hydrogen (H_2) is formed. Due to the larger geometric size, H_2 is trapped in the micro-void and even accumulates. It might be possible that also additional H-related species, e.g., SiH_4, are formed. As a consequence, blisters can form if a critical amount of hydrogen accumulates at the interface, as it was observed in Fig. 5.2(b). The μc-SiO$_x$:H(n) and the a-SiO$_x$:H(i) layer are only 20 nm thick in total, so that it seems probable that not more than

5 min are enough for the H to accumulate at the interface and deteriorate the passivation. Although, the H diffusion should continue with increasing t_{depo}, the τ_{eff} of the test structures with $T_{\mathrm{f}} \leq 1800$ °C was not affected which can be explained by the growing μc-SiC:H(n) film which itself represents an additional, growing H diffusion barrier. Reducing the thickness of μc-SiO_x:H(n) to half (not shown) resulted in the same strong deterioration of the passivation ($\tau_{\mathrm{eff}} < 10$ μs) even at T_{f} of 1800 °C which is similar to the previous results for T_{f} of 1850 °C. Hence, the reduction of τ_{eff} with reduced thickness supports the idea of an destructive H diffusion mechanism.

Filament temperatures of 1900-2000 °C are beneficial to grow electrically more conductive μc-SiC:H(n) layers as it was shown in Fig. 4.7(b). From the previous results this range of T_{f} seems to be out of the process window, but the H diffusion process also depends on the material properties of the material where H has to diffuse through. The carbon dioxide gas flow rate ratio (f_{CO2}) during the PECVD growth of μc-SiO_x:H(n) has a major impact on material properties. Up to this point the symmetric passivation test structures for the results in Fig. 5.2 were produced with f_{CO2} of 20 %. An increase in f_{CO2} leads to a decrease in the Raman crystallinity (I_{c}) and to an increase of the oxygen content as shown in Fig. 5.4(a-b) and as reported in Ref. [50, 160]. Moreover, increasing f_{CO2} leads to a decrease in electrical conductivity (σ) and an increase in optical bandgap (E_{04}), as shown in Fig. 5.4(c-d). To investigate the protection ability of μc-SiO_x:H(n) against H in-diffusion, the f_{CO2} was varied from 0 % to 40 % in symmetric passivation samples, where the most sensitive a-Si:H(i) was used as passivation layer. In Fig. 5.4(e-g), the τ_{eff} is presented as a function of f_{CO2} during the PECVD growth of μc-SiO_x:H(n) and as a function of T_{f} during the HWCVD growth of μc-SiC:H(n). The T_{f} were 1800 °C, 1900 °C, and 2000 °C and the μc-SiC:H(n) deposition time was 40 min. Considering only the samples with f_{CO2} of 20 %, the τ_{eff} drops drastically for $T_{\mathrm{f}} > 1800$ °C which is similar to the a-SiO_x:H(i) passivated samples from Fig. 5.2(a), where f_{CO2} for the μc-SiO_x:H(n) layer was also 20 %. In Fig. 5.4(e) it can be observed that with 1800 °C the τ_{eff} remained in the millisecond range for f_{CO2}. With 1900 °C and 2000 °C, where the H radical density in the gas phase is strongly increased, the τ_{eff} dropped below 10 μs for f_{CO2} of 10-25 %, but remained above 1 ms for f_{CO2} of 0 % and 30-40 %.

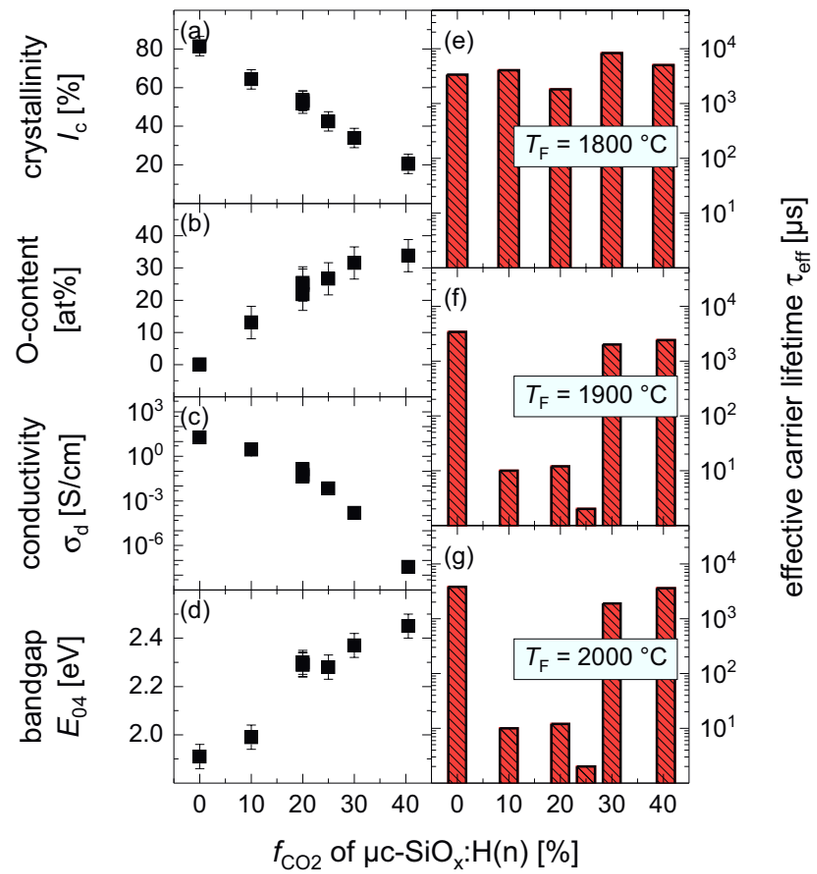

Figure 5.4.: *(a) Raman crystallinity I_c, (b) oxygen content measured by RBS, (c) lateral electrical conductivity σ, and (d) optical bandgap E_{04} of µc-SiO$_x$:H(n) as a function of CO_2 gas ratio f_{CO2}. (e-g) Influence of filament temperature T_f, ranging from 1800-2000 °C, on effective carrier lifetime τ_{eff} of µc-SiO$_x$:H(n)/a-Si:H(i)/c-Si(n)/a-Si:H(i)/µc-SiO$_x$:H(n) passivation test structure where the µc-SiO$_x$:H(n) was deposited using a CO_2 gas ratio f_{CO2} between 0-40 %.*

The microstructure of the oxygen-free (f_{CO2} = 0 %) and the oxygen-rich (f_{CO2} = 30-40 %) µc-SiO$_x$:H(n) films are illustrated schematically in Fig. 5.5(b-c) which is based on the model suggested by Richter et al. [160]. While the oxygen-free µc-

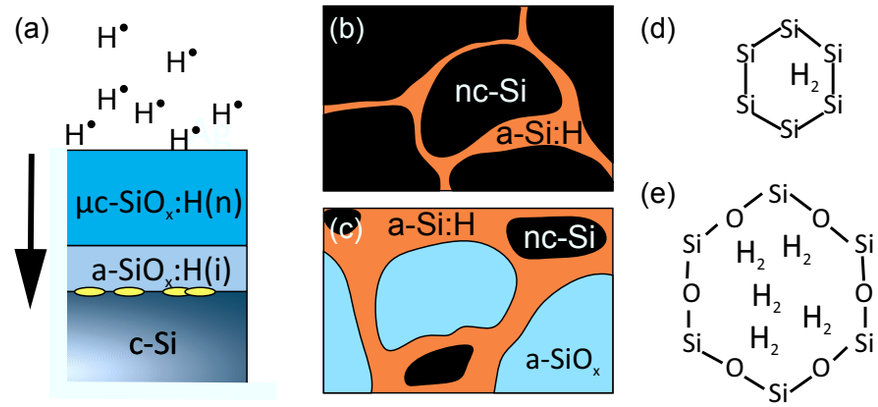

Figure 5.5.: *(a) Schematic illustration of atomic hydrogen from the HWCVD gas phase diffusing through µc-SiO$_x$:H(n)/a-SiO$_x$:H(i) to deteriorate the passivation at the c-Si interface, which can lead to blistering. Schmatic microstructure of µc-SiO$_x$:H(n) with (b) f_{CO2} = 0 % and (c) f_{CO2} >> 0 %, based on findings of Richter et al. [160]. Molecular hydrogen (H$_2$) trapped in void formed by (d) Si-Si or (e) Si-O bonds.*

Si:H(n) consists of an a-Si:H and a nc-Si phase, a-SiO$_x$:H appears as third phase in the μc-SiO$_x$:H(n) material. The grain size of nc-Si decreases with increasing f_{CO2} and the a-SiO$_x$:H phase becomes more dominant. The results of τ_{eff} in Fig. 5.4(e-g) reveal that in-diffusion of atomic H seems to be inhibited by a large grain size of nc-Si which might be explained by the low solubility of H in crystalline silicon [157]. Since higher f_{CO2} gives smaller grain size, the H may in-diffuse more easily through grain boundaries, vacancies, or interstitials of the a-Si:H phase. At the c-Si interface a further diffusion of the H atoms is inhibited, due to very low diffusion coefficient for H in c-Si (10^{-15} - 10^{-12} cm^2/s [159])k. Thus, the atoms recombine and agglomerate in form of molecular H$_2$. The agglomeration of H$_2$ easily leads to a bubble formation, as it was observed in Fig. 5.2(b) and which severely deteriorates the passivation at the interface. These processes are summarized in Fig. 5.5(a). However, this diffusion model only holds for the oxygen-free μc-Si:H(n) protection layers, because τ_{eff} is in the millisecond range for f_{CO2} of 30-40 % although the low Raman crystallinity indicates small grain sizes or the absence of crystallites. According to Sopori et al. [26] atomic H will diffuse slower in oxygen-rich material because the presence

of O lowers the propensity for generation of vacancies which are important for a high diffusivity and solubility of H. Additionally, Einsele et al. [161] reported that increasing f_{CO2} leads to an increase in number of voids. It might be that atomic H recombines to H_2 and is trapped inside the SiO lattice. Material consisting of Si-O bonds (Fig. 5.5(e)) are larger in volume and lower in density than those consisting of Si-Si (Fig. 5.5(d)) and therefore can collect more H_2. This might be an additional reason why for f_{CO2} of 30-40 %, where the oxygen content is highest (Fig. 5.4(e)), the H diffusion seems to be inhibited. In other words, the diffusivity of atomic H might be decreased in the a-SiO_x phase, so that in-diffused H does not reach the c-Si interface but remains in the oxygen rich μc-SiO_x:H(n) layer.

5.1.2. SHJ solar cells with silicon carbide n-doped layer and a-SiO_x:H(i) passivation layer

After having investigated the deterioration of the passivation during the HWCVD process for the growth of μc-SiC:H(n), the performance of corresponding solar cells are studied in the following. As illustrated in Fig. 5.1(b) a 15 nm thick μc-SiC:H(n) layer was deposited on top of a 15 nm thick μc-SiO_x:H(n) layer using a filament temperature of 1800 °C. For the μc-SiO_x:H(n) layer the CO_2 gas ratio was varied in the range of 0-40 %. The layers are labeled by μc-SiO_x:H(n)-X, where X stands for the corresponding f_{CO2}. In addition, reference cells without μc-SiC:H(n) layer but with a 20 nm thick μc-SiO_x:H(n) layer with f_{CO2} of 20 % were fabricated.

The solar cell parameters, i.e., V_{oc}, J_{sc}, FF, and η of the introduced solar cell stacks are shown in Fig. 5.6(a-d) and presented as a function of f_{CO2}. The V_{oc} and FF values are average values out of four solar cells of 2×2 cm^2 size. The J_{sc} values were derived from the EQE spectra in Fig. 5.6(e). The dashed lines serve as a guides to the eye.

The V_{oc} of the solar cells in Fig. 5.6(a) with μc-SiC:H(n) was 669 mV for f_{CO2} from 0 % to 20 % and then decreased for f_{CO2} = 30 % to 661 mV and further down to 648 mV for f_{CO2} = 40 %. The V_{oc} is about 670 mV for the reference cells which were produced with 20 nm of μc-SiO_x:H(n)-20. The V_{oc} value of the reference cell is

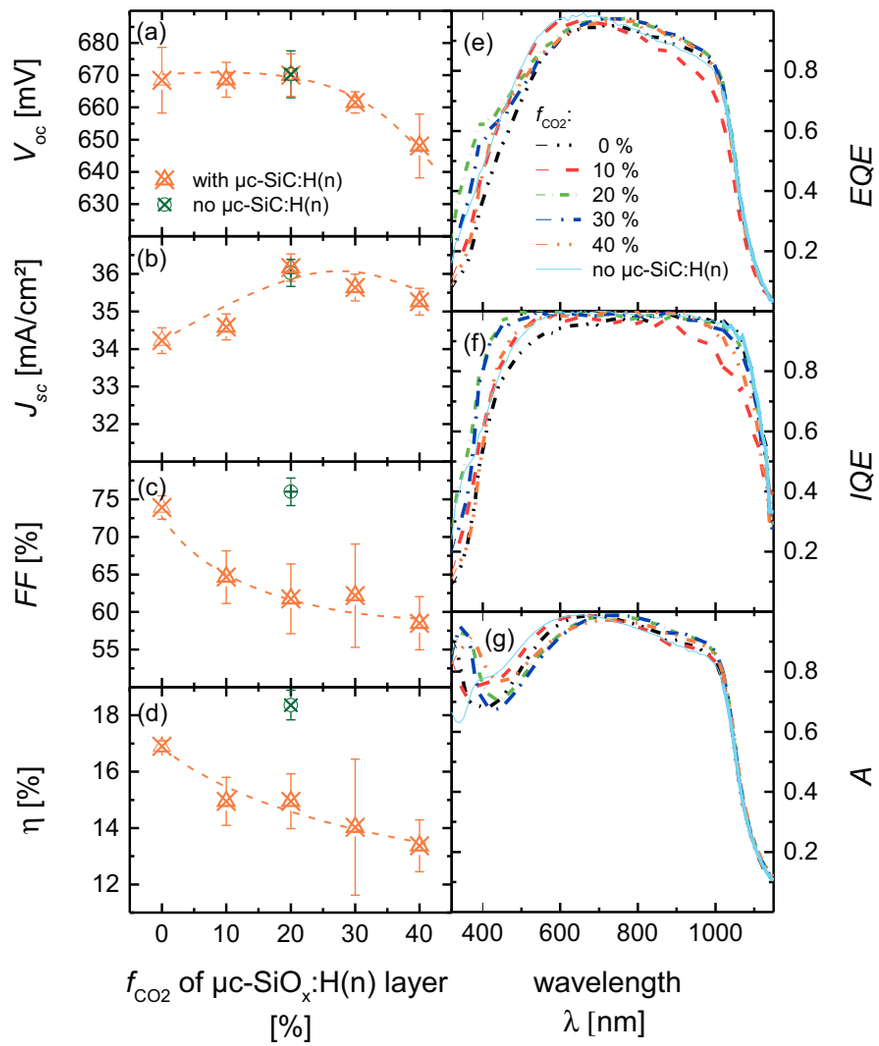

Figure 5.6.: *SHJ solar cell results for test structure illustrated in Fig. 5.1(b) with f_{CO2} between 0-40 % for the µc-SiO$_x$:H(n) protection layer: (a) open circuit voltage V_{oc}, (b) short circuit current density J_{sc}, (c) fill factor FF, and (d) solar energy conversion efficiency η versus f_{CO2}; (e) external quantum efficiency EQE, (f) internal quantum efficiency IQE, and (g) absorptance A versus wavelength λ. Reproduced from Ref. [150], with the permission of The Japan Society of Applied Physics.*

in good agreement with the 667 mV reported by Ding et al. for similar types of SHJ solar cells [50]. Ding et al. attributed the decrease in V_{oc} with increasing f_{CO2} of the μc-SiO$_x$:H(n) to a decrease of the field effect due to a reduction of the doping of the μc-SiO$_x$:H(n) window layer, which is also expected in the present case (Fig. 5.4(c)). In addition, it was observed that adding the μc-SiC:H(n) layer did not affect the V_{oc} as there was almost no difference between the V_{oc} of solar cells with and without μc-SiC:H(n) layer in Fig. 5.6(a). The highest V_{oc} that has been measured for a solar cell with a μc-SiC:H(n) layer is 679 $\pm$ 3 mV, which is comparable to the V_{oc} value reported by Irikawa et al. [11] who achieved 680 mV for V_{oc} by using an amorphous silicon carbide passivation layer.

The J_{sc} of the solar cells with μc-SiC:H(n) layers in Fig. 5.6(b) ranged between 34.2 $\pm$ 0.3 mA/cm^2 and 36.2 $\pm$ 0.4 mA/cm^2 whereas the highest J_{sc} value was found for f_{CO2} = 20 %. The J_{sc} was 36.0 $\pm$ 0.4 mA/cm^2 for the reference cell without μc-SiC:H(n), . Thus, the highest average J_{sc} for solar cells with a μc-SiC:H(n) layer was comparable to the average J_{sc} of the reference cells within the accuracy of the measurement, although in total the μc-SiC:H(n)/μc-SiO$_x$:H(n) double layer is 10 nm thicker than the μc-SiO$_x$:H(n) single layer.

In Fig. 5.6(e-f) the EQE, the IQE, and the A of all solar cells are shown as a function of λ, in order to discuss the J_{sc} values (Fig. 5.6(b)) in more detail. In the short λ range (320-460 nm) the EQE (Fig. 5.6(e)) of the solar cells with μc-SiC:H(n) layer first increased with increasing f_{CO2}, was largest for f_{CO2} = 20 %, and then decreased again for 30 % and 40 %. The EQE reached 0.62 at λ = 400 nm for f_{CO2} = 20 %. In comparison, the EQE for the reference cell without μc-SiC:H(n) only reached 0.48 at λ = 400 nm. The same trend can also be observed for the IQE (Fig. 5.6(f)) for short λ. Most probably the decrease in IQE with f_{CO2} = 30 % is related to electrical issues at the front side of the cell, which become even more severe for f_{CO2} of 40 %. This electrical issue may be explained by higher recombination rates at the front surface field of the μc-SiO$_x$:H(n)/a-SiO$_x$:H(i)/c-Si interface for f_{CO2} = 30-40 %, as is indicated by lower implied open circuit voltage (iV_{oc}) values of 610 $\pm$ 12 mV as compared to the iV_{oc} values of 665-690 mV for f_{CO2} = 0-20 % (not shown). A decrease in the IQE due to an increase in parasitic

absorption can be excluded the opposite is expected, since E_{04} of the μc-SiO_x:H(n) at the front increases with higher f_{CO2} (Fig. 2(a)). However for f_{CO2} = 0-20 %, a decrease in parasitic absorption with increasing f_{CO2} leads to an observable increase in the IQE. Compared to the reference, the IQE in the short λ range is higher for f_{CO2} = 20 %, which shows the desired reduction of parasitic absorption achieved by adding the μc-SiC:H(n) layer. In the long λ range (700-1000 nm) the EQE (Fig. 5(a)) of the solar cells with μc-SiC:H(n) layer is comparable for all f_{CO2}. It should be noted that the sample with f_{CO2} = 10 % probably suffers from a deteriorated back side passivation, which is indicated by the low IQE (Fig. 5.4(g)) in the λ range between 900 nm and 1100 nm. Although, in the short λ range (320-460 nm) the EQE of the reference is inferior compared to the solar cells with μc-SiC:H(n) and f_{CO2} of 20 % or 30 %, in the range of 460-700 nm the EQE of the reference is up to 0.1 higher, e.g., at 600 nm, where the photon flux of the sun spectrum is the highest, the EQE is 0.98 for the reference whereas with μc-SiC:H(n) and f_{CO2} = 20 % the EQE is only 0.92. The reason for these trends in the EQE can be explained by the shift of the absorption maxima shown in Fig. 5.4(g). The maximum of $A(\lambda)$ for the reference is shifted towards 650 nm whereas it is located around 730 nm for the other cells with μc-SiC:H(n), which leads to a higher A in the range of 460-700 nm for the reference solar cell. As explained above, the interference pattern strongly depends on the thickness and the refractive index of each layer. An optimization of the layer thicknesses could give rise to a further increase in A and hence improve J_{sc}.

The average FF values for solar cells with a μc-SiC:H(n) layer in Fig. 5.6(c) decreased continuously from 74 % to 59 % with increasing f_{CO2} which is strongly determined by an increase in R_s from 2.2 Ω/cm^2 to 5.8 Ω/cm^2, respectively. The increase in R_s can be explained by the decrease in σ of the μc-SiO_x:H(n) layer with increasing f_{CO2} (Fig. 5.4(f)). The low σ of 10^{-7} S/cm of the implemented μc-SiC:H(n) adds an additional series resistance to the stack. Furthermore, according to the TEM micrograph of the front side layer stack, presented in Fig. 5.7, the μc-SiC:H(n) layer is rather amorphous than microcrystalline. The reason for the layer to be amorphous is likely the extended nucleation zone of μc-SiC:H(n) as reported by Heidt et al. [113, 126]. According to Heidt et al. [113, 126], the nucleation takes

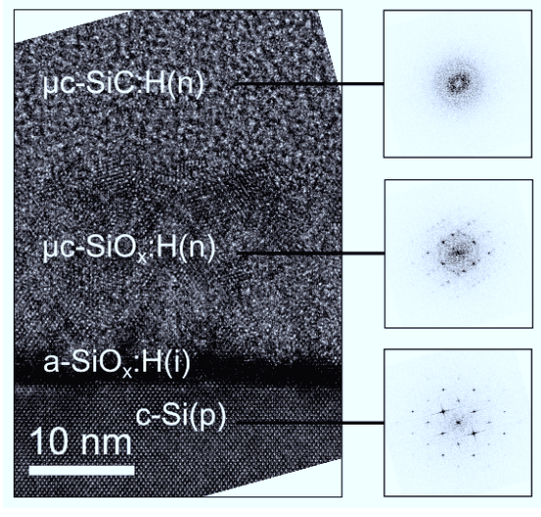

Figure 5.7.: *TEM bright field image of the solar cell cross section showing the μc-SiC:H(n), μc-SiO$_x$:H(n), and a-SiO$_x$:H(i) layers on p-type c-Si with (100) orientation. In addition the corresponding electron difraction patterns are also presented. Reproduced from Ref. [150], with the permission of The Japan Society of Applied Physics.*

place in the first 30 nm, but the layer in the cells is only 15 nm thick, whereas the material properties of μc-SiC:H(n) presented in this work were measured on 150 nm thick films. Consequently, the conductivity of the μc-SiC:H(n) layer should be even lower than 10^{-7} S/cm, because the amorphous character of the layer limits the electrical transport (Sec. 4.1). Hence, minimizing the thickness of the nucleation phase is a key point for future optimizations on μc-SiC:H(n) in SHJ solar cells, in order to decrease R_s and increase FF.

As a result of the trends of V_{oc}, J_{sc}, and FF as a function of f_{CO2}, the η in Fig. 5.6(d) of the cells with μc-SiC:H(n) layer decreased continuously from 16.9 ± 0.2 % to 13.4 ± 0.9 % whereas the η of the reference without μc-SiC:H(n) is 18.37 ± 0.5 %. The difference clearly arises from the difference in FF (Fig. 5.6(c)). To increase the J_{sc} of the best cell (f_{CO2} = 0 %) of the cell series, an nanoimprint was applied as it is described by Meier et al. [162]. In Fig. 5.8 the corresponding current-voltage curve as well as the EQE, IQE, and R spectra are shown. The J_{sc}

improved from 34.2 ± 0.3 mA/cm^2 to 37.6 ± 0.3 mA/cm^2 which is an improvement of 3.4 mA/cm^2 and in combination with a FF of 74.2 ± 1.5 % and V_{oc} of 0.677 ± 0.003 V leads to an η of 18.9 ± 0.3 %.

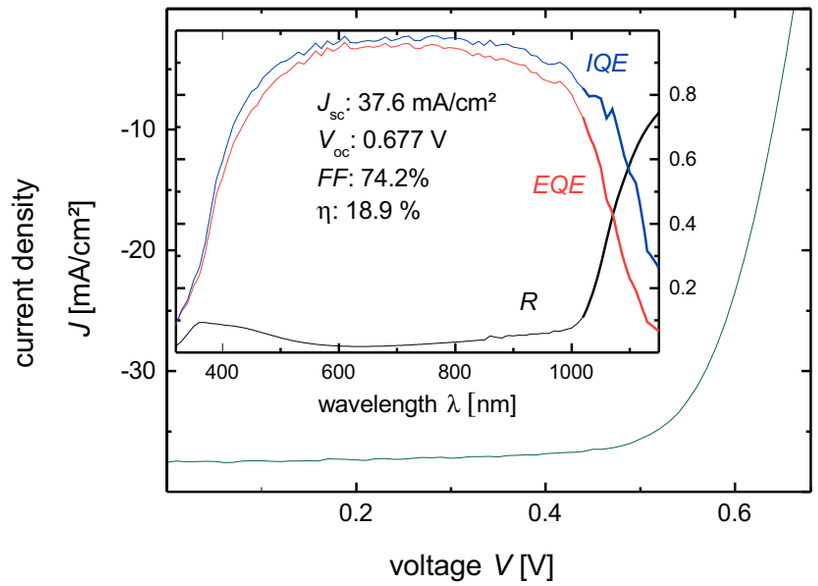

Figure 5.8.: *Current-voltage characteristics of the best SHJ solar cell of this work and the corresponding quantum efficiencies (EQE and IQE) and reflectance R. In addition to the cell structure, that is illustrated in Fig. 5.1(b), a nanoimprint was applied as described in [162]. Reproduced from Ref. [150], with the permission of The Japan Society of Applied Physics.*

In this section, it was shown that it is possible to implement μc-SiC:H(n) using HWCVD without deteriorating the a-SiO$_x$:H(i) passivation and that working SHJ solar cell using the μc-SiC:H(n)/μc-SiO$_x$:H(n)/a-SiO$_x$:H(i) front stack can be produced. The IQE showed that the parasitic absorption could be decreased by using the μc-SiC:H(n)/μc-SiO$_x$:H(n)/a-SiOx:H(i) front stack, although the microcrystalline films had a total thickness of 30 nm as compared to the 20 nm of the reference cell without μc-SiC:H(n). The FF must be increased for future improve-

ments of SHJ solar cells with μc-SiC:H(n), which can be done by increasing the σ of μc-SiC:H(n). For this purpose, increasing the order in microstructure of the μc-SiC:H(n) film seems to be ideal, because E_{04} would increase too, as it was shown in Fig. 4.12(b) and Fig. 4.24(c). Another possibility would be to actively dope the μc-SiC:H(n) film, but this would lead to a decrease in E_{04} (Fig. 4.24(c)), due to an increased defect density [8]. The optimization of the FF should be performed on μc-SiO$_x$:H(n) with higher f_{CO2} (e.g., 20 %), in order to benefit from the wide E_{04} and hence keep parasitic absorption low. A further increase of J_{sc} in future is feasible by using textured wafers instead of flat wafers, due to reduced reflection losses and light trapping.

5.2. Silicon carbide in SiO$_2$ passivated SHJ solar cells

In the previous section, it was shown that several requirements have to be fulfilled to obtain τ_{eff} values in the millisecond range which correspond to implied open circuit voltage (iV_{oc}) values above 700 mV for implementing HWCVD grown μc-SiC:H(n) in a SHJ passivated by a-Si:H(i) or a-SiO$_x$:H(i). Using a μc-SiO$_x$:H(n) protection layer against H etching during the HWCVD and a very narrow process window for the HWCVD process that prevents H in-diffusion on the front side are necessary to prevent the deterioration of the passivation. Silicon dioxide (SiO$_2$) represents an attractive alternative passivation layer. Theoretically, it should withstand H etching more easily [123], it should give rise to τ_{eff} values above 1 ms [42], and it posses a large optical bandgap of more than 8 eV [34]. However, the electrically insulating nature of SiO$_2$ might limit the performance of the solar cell due to increased series resistance. Therefore, SiO$_2$ could be a suitable passivation layer for solar cell application in combination with HWCVD grown μc-SiC:H(n), if the SiO$_2$ thickness is kept to a minimum. In fact, a thickness below 2 nm should be targeted, since it becomes possible for the charge carriers to tunnel through the SiO$_2$ layer. This ultra-thin oxide is also called tunnel oxide in the following.

It is possible to produce SiO_2 by thermal oxidation [163–165], film deposition [166,167], or by wet-chemical oxidation [168–170]. So far, the fabrication of a tunnel oxide for solar cell application was most successful by wet chemical oxidation which gave rise to a solar energy conversion efficiency of up to 25.1 % and V_{oc} of 718 mV [42]. Most commonly the wet chemical tunnel oxide is grown by dipping the c-Si wafer in 69.5% HNO_3 solution, where the reported oxide thicknesses, obtained by ellipsometry or TEM, varied between 1.1-1.4 nm [40, 170]. The use of a HNO_3 solution leads to a low defect density at the interface (D_{it}) which was investigated in several works [168, 170–175] and which was introduced by Kobayashi et al. [168] as NAOS (nitric acid oxidation of Si) method. Other wet-chemical oxidation methods were intensively investigated by Angermann et al. [165, 169, 176–179] for the last twelve years. Nevertheless, the NAOS method attracted the vast attention through the TOPCon (tunnel oxide passivated contact) concept for passivated rear contacts, as reported in Ref. [33, 37, 39–41, 170, 173, 175, 180, 181] due to the excellent solar energy conversion efficiency exceeding 25 % [42, 182] that was reached by Fraunhofer ISE and ISFH.

5.2.1. Effect of silicon carbide deposition on SiO_2 passivation

In this work, μc-SiC:H(n)/SiO_2 test structures were produced as sketched in Fig. 5.9(a) by using HWCVD and HNO_3, respectively, in order to investigate the influence of the HWCVD process parameters on the passivation quality. In Fig. 5.9(b) the corresponding targeted solar cell structure is illustrated. In contrast to the TOPCon concept, the passivated contact is placed on the front side of the solar cell in this work, due to the high transparency of the μc-SiC:H(n)/SiO_2 layer stack. In pre-experiments (not shown), it was found that the best passivation quality is achieved with a concentration of 69.5% HNO_3 and that the temperature of the solution did not have a significant impact on iV_{oc} (< 2 mV) which is in agreement with Ref. [34]. Therefore, all results that are shown in the following of this work were produced with a 69.5% HNO_3 solution at room temperature. As the lateral conductance of the μc-SiC:H(n)/SiO_2 layer stack is insufficient, a 70 nm thick indium tin oxide (ITO) layer is used to collect the generated charge carriers at the front contacts.

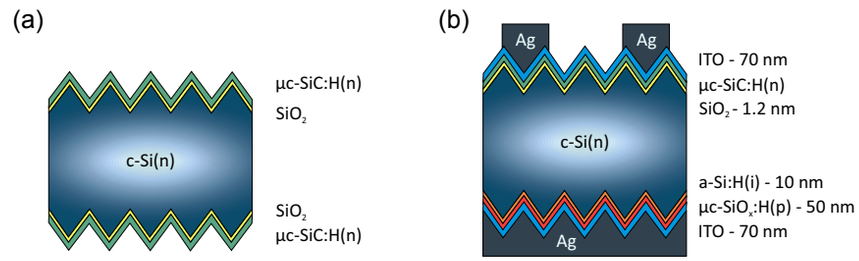

Figure 5.9.: *Schematic illustrations of (a) passivation test structure and (b) SHJ solar cell structure on textured n-type silicon wafer using µc-SiC:H(n)/SiO_2 for passivation.*

The effective lifetime of SiO_2/c-Si/SiO_2 test structures without μc-SiC:H(n) was always below 1 μs when it was measured directly after the oxidation. An annealing at 850 °C in a nitrogen atmosphere increased τ_{eff} to 20 μs. In Fig. 5.10(a,c) and Fig. 5.12(a,c), it can be observed that it is possible to achieve values for iV_{oc} above 700 mV with the μc-SiC:H(n)/SiO_2 layer stack which correspond to τ_{eff} in the millisecond range. It can also be observed that the values strongly depend on the HWCVD parameters during the μc-SiC:H(n) growth. It should be noticed that c-Si surfaces were flat for Fig. 5.10(a) and textured for Fig. 5.10(c), but no significant difference of iV_{oc} could be observed. In Fig. 5.10(a), iV_{oc} is presented as a function of the filament-substrate distance ($d_{\text{f-s}}$) used during the μc-SiC:H(n) deposition. The iV_{oc} values rise linearly from 665 mV to 701 mV with increasing $d_{\text{f-s}}$, so that iV_{oc} increases in average by 0.5 mV per millimeter of increasing $d_{\text{f-s}}$. Simultaneously, the σ of μc-SiC:H(n) decreases by 3 orders of magnitude from 5×10^{-4} S/cm to 4×10^{-7} S/cm by increasing $d_{\text{f-s}}$ from 40 mm to 97 mm. The decrease in σ implies a decrease in field effect passivation that contributes to the total passivation of the SiO_2/c-Si interface. However, the increase of iV_{oc} shows an improvement of the passivation quality. The field effect does not seem to have a major influence, which was also confirmed by the iV_{oc} (= 690 mV) which had not increased after increasing the σ of μc-SiC:H(n) to 10^{-1} S/cm with N_2 doping (F_{N2} = 10 sccm). Hence, the passivation quality must have improved in terms of chemical passivation when the $d_{\text{f-s}}$ was increased. The chemical passivation quality might have improved by H atoms from the gas phase that saturated the defects at the c-Si interface. More details

about the impact of $d_{\text{f-s}}$ on the μc-SiC:H(n) material may be found in Sec. 4.1.

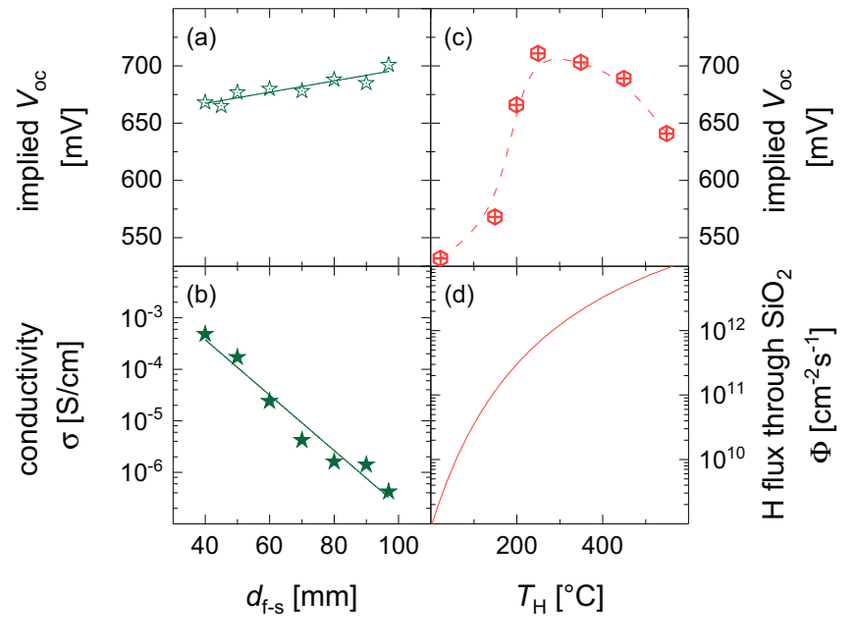

Figure 5.10.: *Influence of the filament-substrate distance $d_{f\text{-}s}$ on (a) iV_{oc} of the passivation test structure, presented Fig. 5.9(a), and on (b) the lateral electrical conductivity σ of the deposited μc-SiC:H(n) film. Influence of the heater temperature T_H on (c) iV_{oc} and on (d) H flux through SiO_2, based on the work of Nickel et al. [123].*

In Fig. 5.10(c) iV_{oc} is plotted as a function of the heater temperature (T_{H}). In this case, the iV_{oc} varies between 532-711 mV over a T_{H} range of 23-550 °C. For $T_{\text{H}} < 250$ °C, the iV_{oc} increases strongly with increasing T_{H} and for $T_{\text{H}} > 250$ °C the iV_{oc} decreases again. Nickel et al. investigated H diffusion through SiO_2/c-Si interfaces [123]. By analyzing monoatomic deuterium content profiles and varying the substrate temperature from 70-310 °C, the activation energy of deuterium flux through the oxide (Φ) was derived to be 0.31-0.36 eV. In Fig. 5.10(d) the Φ is calculated as a function of T_{H}, in order to reproduce the fit from Nickel et al. [123].

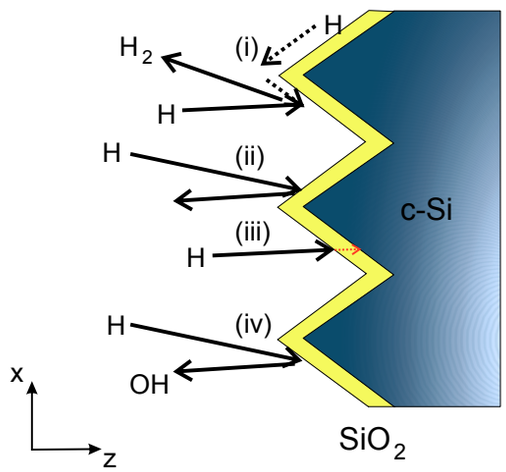

Figure 5.11.: *Schematic description of processes at the oxide surface during the exposure to atomic hydrogen (H) of the HWCVD process: (i) H migrates at the surface and eventually recombines to molecular H_2, (ii) atomic H bounces off the oxide surface, (iii) H penetrates the oxide surface and diffuses through the oxide to the c-Si surface, (iv) H chemically reduces the oxide layer.*

The following function was used for the calculation

$$\Phi(T_{\mathrm{H}}) = \Phi_0 \exp\left(\frac{-E_{\mathrm{A}}}{k_{\mathrm{B}} T_{\mathrm{H}}}\right), \tag{5.1}$$

where Φ_0 is 10^{15} $\mathrm{cm^{-2}s^{-1}}$, E_{A} is 0.31 eV, and $\mathrm{k_B}$ is the Boltzmann constant. The Φ increases by 3 orders of magnitude over the whole T_{H} range. The H diffusion is only one of several processes that take place in parallel during the exposure to atomic H during the HWCVD process. There exist four main processes at the oxide surface: (i) H migrates at the surface and eventually recombines to molecular H_2, (ii) atomic H bounces off the oxide surface, (iii) H penetrates the oxide surface and diffuses through the oxide to the c-Si surface, (iv) H etches the oxide layer by forming a bond with an O atom. If T_{H} is small, e.g., smaller than 250 °C, it is unlikely for H to diffuse through the SiO_2 (Φ is smallest). Therefore, the H etching of the oxide layer is enhanced. This leads to a deterioration of the surface passivation, as it is

indicated by the extremely low iV_{oc} values down to 532 mV. In a second temperature regime with moderate T_H between 250-450 °C it is probable for the H atoms to diffuse through the SiO_2 (Φ is moderate). At the c-Si interface the H atoms might terminate the defects that act as recombination centers. At this point it is worth to mention, that the passivation quality of the μc-SiC:H(n)/SiO_2/c-Si passivation is at a high level even though the wet-chemical oxide was not exposed to any high temperature that is usually needed to increase the passivation quality of the SiO_2 passivation. It might be that indeed in parallel to the μc-SiC:H(n) deposition a H treatment also takes place. Interestingly, for T_H of 550 °C a drop of iV_{oc} down to 641 mV can be observed which might be caused by an effusion of H (Φ is highest). A very similar dependence of the passivation quality on the temperature was already reported by Nagayoshi et al. [183] in 1996 who used a microwave hydrogen afterglow to create H radicals. As mentioned earlier in this chapter, the solubility of H in c-Si is very low [157], so that H atoms are hindered to diffuse further inside the c-Si bulk. Consequently, for very high Φ the effective diffusion direction might more and more change towards the outside, so that at the end effusion takes over in-diffusion and the defects at the interface are not passivated by H.

The H treatment takes place simultaneously with the μc-SiC:H(n) growth, but with increasing film thickness the μc-SiC:H(n) itself forms an additional growing diffusion barrier for H and the in-diffusion of H is continuously decreased over deposition time. Therefore, beside the H etching and the H flux in SiO_2 also the deposition rate (r_{depo}) of μc-SiC:H(n) should be taken into account. In Fig. 5.12(a-b), iV_{oc} and r_{depo} are plotted as a function of MMS gas flow rate (F_{MMS}) for textured c-Si wafers from the same batch as for Fig. 5.10(c). The iV_{oc} values exceed 700 mV for the F_{MMS} range of 4-8 sccm, but for smaller F_{MMS} as well as for larger F_{MMS} the iV_{oc} is decreased. On the one hand, for F_{MMS} 10-30 sccm the values of iV_{oc} decrease continuously down to 553 mV with increasing F_{MMS}. Simultaneously, the r_{depo} increases strongly with increasing F_{MMS} and is 6-14 times higher than for F_{MMS} of 4-8 sccm. These results support the assumption of μc-SiC:H(n) being itself a growing H diffusion barrier that inhibits H to reach and passivate the defects at the c-Si interface. On the other hand, a F_{MMS} of 2 sccm leads to only 661 mV of iV_{oc}, due to a r_{depo} which is 2-6 times smaller than for F_{MMS} of 4-8 sccm which indicates higher

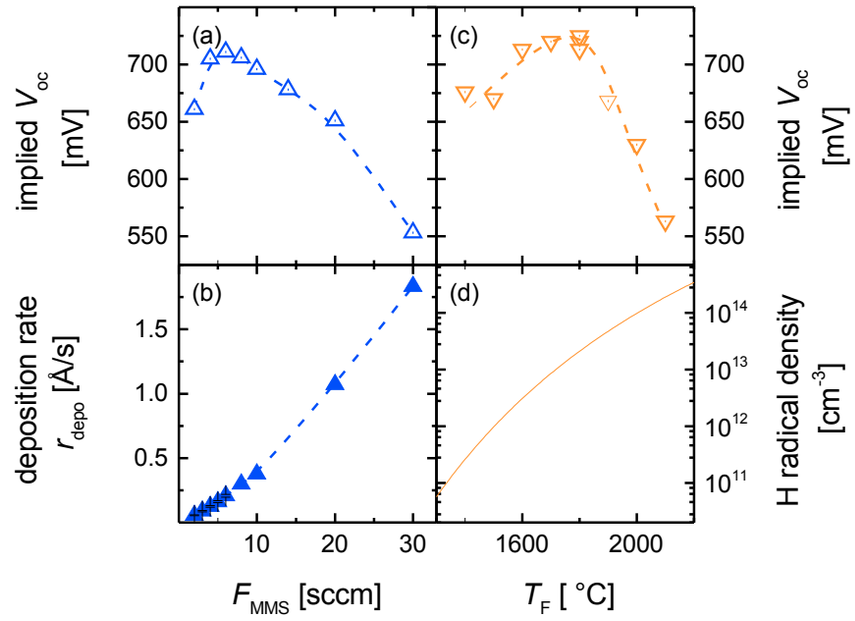

Figure 5.12.: *Influence of the MMS gas flow rate F_{MMS} on (a) iV_{oc} of the passivation test structure, presented Fig. 5.9(a), and on (b) the deposition rate r_{depo} of μc-SiC:H(n). The H gas flow rate was kept constant at 94 sccm. In (c), iV_{oc} is plotted as a function of the filament temperature T_f and in (d) the qualitative behavior of the H radical density is plotted versus T_f, based on the H radical measurements of Umemoto [117].*

etching rates. Thus, for too low F_{MMS} the SiO_2/c-Si passivation is probably deteriorated through H etching of SiO_2, because of inceased dilution of the gas mixture with H_2.

The influence of the filament temperature (T_{f}) on the passivation quality is investigated in the following, because of its strong influence on the opto-electronic properties of μc-SiC:H(n) (see Sec. 4.1). In addition, the results in Sec. 5.1 have shown that too high T_{f} may deteriorate the passivation quality, due to a too high H radical density in the gas phase. In Fig. 5.12(c) the iV_{oc} is presented as a function of T_{f}, where flat c-Si wafers were used, which were from another wafer batch than

for Fig. 5.10(a). The values for iV_{oc} first increased from 670 mV to 725 mV with increasing T_f up to 1800 °C and then decreased strongly down to 563 mV for higher T_f. In this case, several effects might influence iV_{oc} simultaneously. The variation in iV_{oc} cannot be explained simply by too high or too low r_{depo}, because r_{depo} decreases only very slightly with increasing T_f (see Fig. 4.3(b)). The substrate temperature and the H radical density in the gas might rather play an important role. As the T_f was varied from 1400 °C to 2100 °C, the heating of the substrate through thermal radiation from the filaments is very different. Three temperature ranges might be distinguished in Fig. 5.12(c): (i) $T_f < 1600$ °C, where the substrate temperature might be too low which leads to a low Φ and then to a low iV_{oc} of 670-676 mV; (ii) T_f is 1600-1800 °C, where iV_{oc} is highest with 691-725 mV; (iii) $T_f > 1800$ °C, where the increase in substrate temperature leads to H effusion as it was observed in Fig. 5.10(c) which decreases iV_{oc} continuously. For (iii), however, a more detailed comparison between the T_H series (Fig. 5.10(c)) and the T_f series (Fig. 5.12(c)) shows that H effusion might not be the only mechanism. In Fig. 5.10(c) iV_{oc} drops below 650 mV after increasing T_H by 300 °C from 250 °C to 550 °C, while in Fig. 5.12(c) for an increase of T_f by 300 °C from 1800 °C to 2100 °C it even drops down to 560 mV. According to Umemoto et al. [117] the H density in the gas phase increases by several orders of magnitude with increasing T_f, where an effective enthalpy for the H atom formation from H_2 on the filament surfaces was determined to be 239 kJ mol^{-1}. Based on their measurements, the H radical density is redrawn as a function of T_f in Fig. 5.12(d). Thus, for T_f above 1800 °C it might be that increased H etching of the SiO_2 layer might deteriorate the passivation quality, although the slight decrease in r_{depo} does not give a direct indication for higher H etching rates. Hence, it can only be speculated that the combination of H effusion from high substrate temperature and H etching of the surface from a high H radical density in the gas phase might be responsible for the strong deterioration of the passivation quality. Interestingly, T_f is again restricted to 1800 °C or lower in order to achieve high iV_{oc} as it was already observed for a-SiO_x:H(i) and a-Si:H(i) passivated c-Si surfaces in Sec. 5.1.

Before the discussion of the performance of solar cells with μc-SiC:H(n)/SiO_2/c-Si(n) front side, it is worth to discuss the electrical transport of the charge carriers

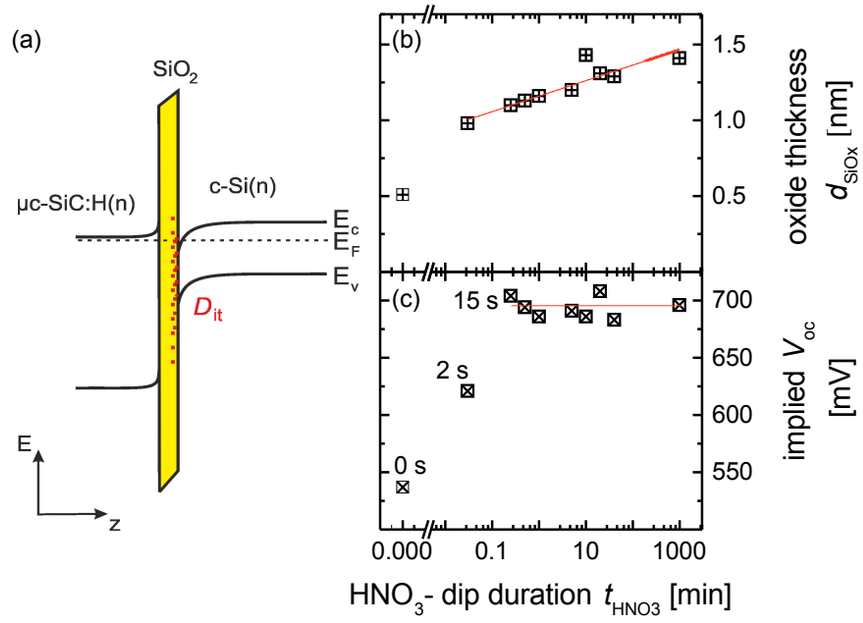

Figure 5.13.: *(a) Schematic energy band diagram of µc-SiC:H(n)/SiO_2/c-Si(n) interface, where the defect density at the interface to c-Si is denoted by D_{it}. (b) Oxide thickness SiO_2, derived from ellipsometer measurement. (c) iV_{oc} as a function of the duration that the c-Si wafer was dipped in 69 % nitric acid solution t_{HNO3}.*

through the tunnel oxide. The energy band diagram of the interface is sketched in Fig. 5.13(a). Generally, the tunnel oxide can be treated like a potential barrier, where according to Ref. [40] the transmission probability of electrons to tunnel through can be expressed as

$$T_{\mathrm{e}} \propto \exp\left[-d_{\mathrm{SiO2}}\sqrt{\frac{4\pi m_{\mathrm{e}}}{\mathrm{h}}\Delta E_{\mathrm{c}}}\right] \tag{5.2}$$

and for holes as

$$T_{\mathrm{h}} \propto \exp\left[-d_{\mathrm{SiO2}}\sqrt{\frac{4\pi m_{\mathrm{h}}}{\mathrm{h}}\Delta E_{\mathrm{v}}}\right], \tag{5.3}$$

where d_{SiO2} denotes the oxide thickness, m_{e} (m_{h}) the tunneling mass for electrons (holes), h the Planck's constant, and ΔE_{c} (ΔE_{v}) the conduction (valence) band offset. It becomes clear that d_{SiO2} has a significant influence on the transmission

probability: the smaller d_{SiO2} the exponentially higher the transmission probability. In order to find the minimum d_{SiO2}, the HNO_3 dip duration (t_{HNO3}) was varied from 2 s to 17 h. In Fig. 5.13(b-c) the results of d_{SiO2} and iV_{oc} are plotted as a function of t_{HNO3}. To determine d_{SiO2} by ellipsometry double side polished c-Si wafers with (111) orientation were used as substrate while for iV_{oc} double side textured c-Si wafers were used like for all other iV_{oc} studies of this section. The surface of the textured c-Si is orientated in (111) direction, so that the d_{SiO2} values measured on flat (111) c-Si surface should provide similar values as for the textured surfaces. It can be observed that the d_{SiO2} increased with increasing t_{HNO3} and can be fitted by $d_{\mathrm{SiO2}}(t_{\mathrm{HNO3}}) = 0.1 \times \log(t_{\mathrm{HNO3}}) + 1.2$. At 0 min of t_{HNO3}, the HNO_3 dip was omitted and the d_{SiO2} was determined directly after the HF dip. The obtained d_{SiO2} was 0.5 nm which corresponds to the thickness of the native oxide. The corresponding iV_{oc} value was 537 mV which is in the typical range of unpassivated c-Si surfaces or completely deteriorated passivation. Therefore, it can be excluded that the SiC layer acts itself as a passivation layer as it was reported in Ref. [11, 184, 185]. The iV_{oc} increased to 621 mV for the shortest HNO_3 dip of 2 s. The values further increased and saturated around an average value of 694 ± 9 mV for t_{HNO3} of 15 s or longer.

The classical TOPCon concept includes not only the deposition of a doped Si thin film layer, but also annealing or crystallization step, which is followed by a forming gas anneal [33, 173, 175, 180]. According to Feldmann et al. [175] the high temperature anneal at 850-900 °C is needed to improve the iV_{oc} from below 700 mV to about 715 mV. This improvement seems to arise from an in-diffusion of phosphorus or boron doping atoms [38, 180, 186] from the doped film into the c-Si bulk that induces energy band bending in first 100 nm of the c-Si bulk. This mechanisms is not present in the test structures of this work, because no phosphorus was used to dope μc-SiC:H(n) - it was *unintentionally* doped (see Sec. 4.1). Although it was shown that it is possible to achieve iV_{oc} values up to 725 mV on flat and up to 711 mV on textured c-Si wafers with unintentionally n-doped μc-SiC:H only, future investigations should focus on implementing a stronger energy band bending in the c-Si bulk. A promising way could be to apply Cat-doping [151] before the μc-SiC:H(n) deposition. Cat-doping is used to in-diffuse phosphorus or boron atoms and has already demonstrated to improve a-Si:H(i) passivation by bending the energy

bands near the c-Si surface [151]. In addition, a H treatment before or after the μc-SiC:H(n) deposition may also further improve the saturation of the defects by H atoms, because the H treatment, that takes place in parallel to the μc-SiC:H(n) growth, is restricted to the growth conditions for the μc-SiC:H(n) layer. Details about H treatment using HWCVD for a-Si:H(i) and SiO_2 passivation may be found in Ref. [122, 183].

5.2.2. SHJ solar cells with silicon carbide n-doped layer and SiO_2 passivation layer

Two-side contacted design After the development of a second concept with SiO_2 where the implementation of μc-SiC:H(n) gave rise to iV_{oc} values up to 725 mV on flat and up to 711 mV on textured c-Si wafers, the performance of SHJ solar cells with this design, as introduced in Fig. 5.9(b), will be analyzed in the following. As the thickness of a window layer influences many parameters, e.g., electrical resistance, parasitic absorption, and reflection, the thickness of the μc-SiC:H(n) layer (d_{SiC}) was varied from 7-60 nm in the solar cell. The resulting performance of the devices are summarized in Fig. 5.14 in form of η, V_{oc}, J_{sc}, FF, EQE, R and IQE.

In Fig. 5.14(a), it can be observed that for smaller d_{SiC} of 7-15 nm the best values of η were 10.5-11.0 % and for larger d_{SiC} of 30-60 nm 16.8-17.5 %. Similarly, in Fig. 5.14(b) the V_{oc} values of the best solar cells were below 650 mV for small d_{SiC} of 7-15 nm and above 650 mV for larger d_{SiC}. The iV_{oc} values in Fig. 5.14(b) were obtained using the μc-SiC:H(n)/SiO_2/c-Si(n)/a-Si:H(i)/μc-SiO_x:H(p) stack before the metalization. The iV_{oc} was below 650 mV only for the sample with d_{SiC} of 7 nm. All other samples revealed iV_{oc} values between 690-702 mV. The reason for the big difference between iV_{oc} and V_{oc} is not yet understood. The drop in iV_{oc} below 650 mV for d_{SiC} of 7 nm might indicate a lower saturation of the interface defects by H, due to a shorter treatment duration. The iV_{oc} values seem to saturate for longer deposition times.

In Fig. 5.14(c), the J_{sc} of the best cells increased with increasing d_{SiC} from 7 nm to 30 nm. J_{sc} reached 40.1-40.9 mA/cm^2 for d_{SiC} of $\geq$ 30 nm. It is worth to

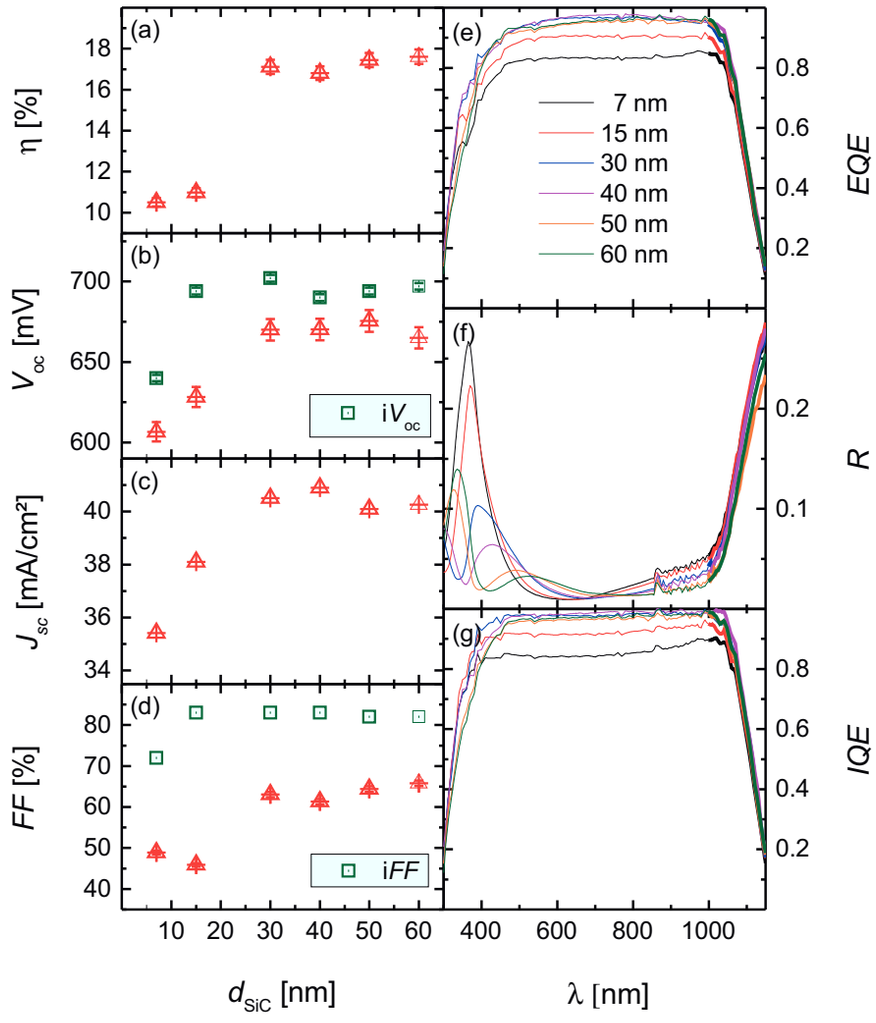

Figure 5.14.: *Resulting performance parameters of solar cell test structures illustrated in Fig. 5.9(b) with different μc-SiC:H(n) layer thicknesses ranging from 7-60 nm: (a) η, (b) V_{oc}, (c) J_{sc}, and (d) FF versus d_{SiC}. (e) EQE, (f) R, and (g) IQE versus wavelength λ.*

relate the J_{sc} data to the EQE, R, and IQE curves in Fig. 5.14(e-g) for a better interpretation of the data. Due to reduced EQE and IQE over almost the whole λ range for small d_{SiC} of 7-15 nm, an electrical issue seems to decrease the extraction of photogenerated charge carriers. Further, the R changed with increasing d_{SiC}, since the interference pattern strongly depends on the layer thickness. The reflection maximum shifted from 350 nm to 500 nm and its intensity decreased for increasing d_{SiC}. Even a second R maximum could be observed for d_{SiC} of 50-60 nm which lead to a decrease in EQE for λ below 400 nm. In addition, the IQE at λ below 450 nm was also decreased for d_{SiC} of 50-60 nm which indicates that current was lost through parasitic absorption in the μc-SiC:H(n) layer. Future optical optimizations of the solar cell front side using μc-SiC:H(n) must focus on minimizing the total reflection and solving the electrical issue for such thin films.

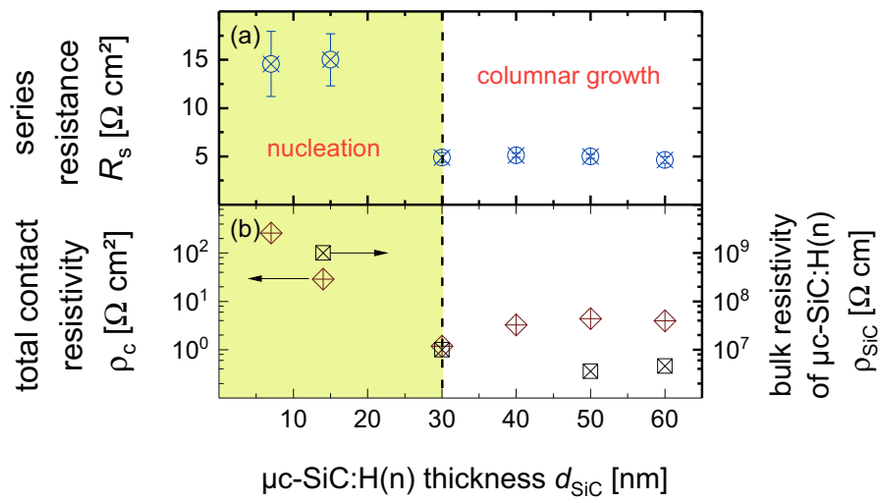

Figure 5.15.: *(a) Series resistance R_s, (b) total contact resistivity ρ_c and bulk resistivity of µc-SiC:H(n) ρ_{SiC} as a function of the µc-SiC:H(n) film thickness d_{SiC}.*

Due to FF values below 70 % in Fig. 5.14(d), it can be derived that a strong electrical loss was present for all d_{SiC}. The FF did not exceed 50 % for 7-15 nm,

which indicates that the electrical loss is more severe for these thicknesses. Much higher implied FF (iFF) values, that ranged from 72-83 %, show that the FF was not limited by recombination. Also the shunt resistance was not responsible for the low FF, as the shunt resistance was in the kΩcm^2 range for all d_{SiC}. The series resistance (R_{s}) in Fig. 5.15(a), however, was high for the entire d_{SiC} range: 11-12 Ωcm^2 for 7-15 nm and 4-5 Ωcm^2 for 30-60 nm. From the Eq. 2.3 it can be derived that R_{s} has to be decreased below 1 Ωcm^2 in future, in order to reach FF larger than 75 %. The total contact resistivity (ρ_{c}) of the Ag/ITO/μc-SiC:H(n)/SiO_2/c-Si stack is the sum of the contact resistances of the neighboring layers of the stack as well as of the bulk resistances of each layer:

$$\rho_{\mathrm{c}} = \rho_{\mathrm{Ag/ITO}} + \rho_{\mathrm{ITO/SiC}} + \rho_{\mathrm{SiC/SiO2}} + \rho_{\mathrm{SiO2/Si}} + \rho_{\mathrm{Ag}} + \rho_{\mathrm{ITO}} + \rho_{\mathrm{SiC}} + \rho_{\mathrm{SiO2}} \tag{5.4}$$

Therefore, it is difficult to identify reliably the cause of the high R_{s}. However, it can be excluded that either the Ag/ITO contact resistance, the ITO sheet resistance, or the ITO/μc-SiC:H(n) contact resistance are responsible for the high values of R_{s}, because the layer stack of Ag/ITO/μc-SiC:H(n) was already used in Sect. 5.1.2, where it gave rise to values of only 2-3 Ωcm^2. The contact resistivity of the entire layer stack correlates with the bulk resistivity of μc-SiC:H(n) (ρ_{SiC}) in Fig. 5.15(b) for cells with d_{SiC} of 7-30 nm. Both types of resistivities decrease by 2 orders of magnitude, which indicates that ρ_{c} is determined by ρ_{SiC} for small film thicknesses of μc-SiC:H(n). The size of SiC crystallites is small within the first 30 nm [126], where the nucleation of the SiC crystallites takes place. Due to the decrease in electrical conductivity with decreasing SiC crystallite size (see Sect. 4.1.3), the high values for ρ_{SiC} originate from the small size of the SiC crystallites in the nucleation phase. Therefore, the electrical conductivity of μc-SiC:H(n) layers thinner than 30 nm should be increased by increasing the size of the SiC crystallites. Another possibility would be to increase the doping of the μc-SiC:H(n) films as it has been proposed in Chap. 4. Both measures might also be beneficial to reduce ρ_{c} and R_{s} for solar cells with $d_{\mathrm{SiC}} > 30$ nm. Furthermore, the SiO_2 layer certainly adds an additional series resistance to the solar cells, because SiO_2 is an insulator. From Eq. 5.2 it can be derived that the transmission probability of electrons to tunnel through the oxide increases exponentially, if the oxide thickness is reduced. Hence, a reduction of the oxide thickness in future should also contribute to a reduction of

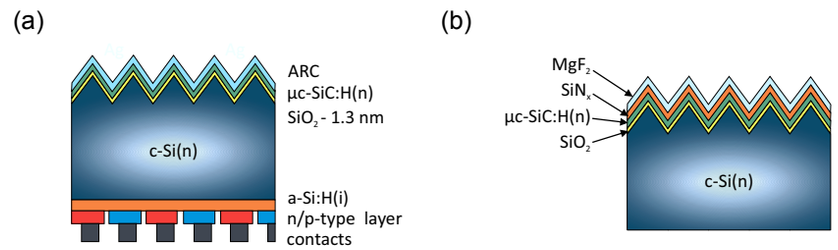

Figure 5.16.: *(a) Interdigitated back contacted (IBC) solar cell test structure with µc-SiC:H(n)/SiO_2 passivation and anti-reflection coating (ARC). (b) Schematic illustration of triple layer ARC consisting of MgF_2/SiN_x/µc-SiC:H(n) for the front side of textured c-Si(n) wafer.*

R_s. In this thesis, the oxide thickness could only be reduced to 1 nm by minimizing the HNO_3-dip duration to 15 s as it is presented in Fig. 5.13. Other chemical solutions might give rise to lower oxide thicknesses and lower R_s while maintaining a high passivation quality.

Interdigitated back contact design Alternatively to the two-side contacted design, the interdigitated back contact (IBC) design, that is presented in Fig. 5.16(a) offers a high potential to implement μc-SiC:H(n) even more gainfully. All contacts are placed on the back side, in order to avoid current losses from contact shadowing. Consequently, the μc-SiC:H(n) layer, used as front surface field on the front side of the solar cell, is not part of the electrical circuit, so that for the IBC design the FF should not depend on the resistance of the μc-SiC:H(n) layer and it should be possible to fully benefit from the large optical bandgap to further reduce parasitic absorption. The second important optical loss is caused by reflection of the sun light at the surface of the solar cell that a portion of the photons do not reach the c-Si where they should be absorbed to contribute to the electrical current. In the following both optical losses are discussed and related to the μc-SiC:H(n) layer. Currently, the front side of IBC-SHJ solar cells usually consists of a-Si:H(n)/a-Si:H(i) as for two-side contacted design and an ARC, e.g., SiN_x. More details may be found in Ref. [187–189].

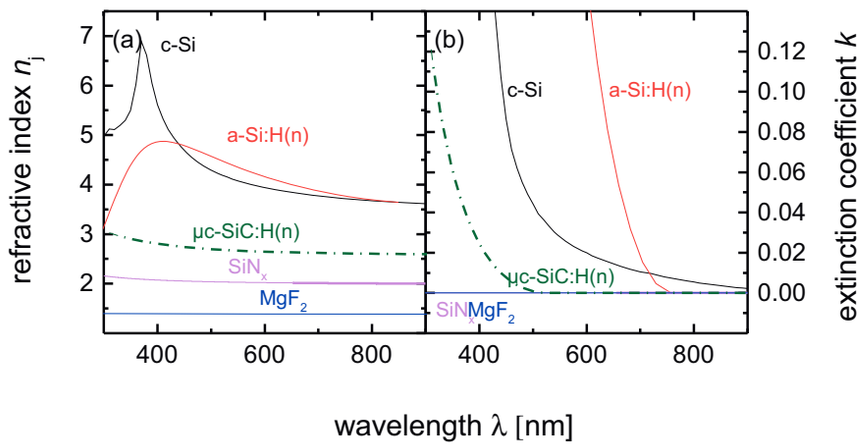

Figure 5.17.: *(a) Real part of complex refractive index n_j and (b) extinction coefficient k as function of wavelength λ.*

To reduce reflection losses an anti-reflection coating is needed. The thickness and the refractive index of the ARC have to be chosen carefully, so that the in coming light wave and the out going light wave interfere destructively with one another which results in zero reflectance (R). The optimum thickness (d_j) for a minimum R can be calculated with a given refractive index (n_j) and a given wavelength (λ) by using $d_\mathrm{j} = \frac{\lambda}{4n_\mathrm{j}}$ for a single layer ARC. Also the optimum n_j can easily be determined by the geometric mean of the refractive indices of the two neighboring materials. However the reflection of a single layer ARC will always represent a compromise in d_j and n_j, thus, an increase in number of ARC layers is preferable to minimize the total reflection. By increasing the number of ARC layers it is possible to implement a fine index grading from air to c-Si and to optimize all thicknesses precisely. An index grading is needed due to the R at the interface of two materials which is defined by $R = |n_\mathrm{j} - n_{\mathrm{j}+1}|^2/|n_\mathrm{j} + n_{\mathrm{j}+1}|^2$.

A triple layer ARC is presented in Fig. 5.16(b) which consists of $\mathrm{MgF_2}/\mathrm{SiN}_x/\mu$c-SiC:H(n). As it can be seen in Fig. 5.17(a) the n_j of the materials align in the right order: ≈ 1.0 for air, ≈ 1.4 for $\mathrm{MgF_2}$, 2.0-2.2 for SiN_x, 2.6-3.0 for μc-SiC:H(n), and

3.6-7.0 for c-Si. The n_j of SiO_2 was assumed to be 1.4-1.5 [190] which does not fit the index grading. However, the SiO_2 does not have to be taken into account, because with less than 2 nm of layer thickness it does not play a role in terms of diffraction of wavelengths in the range that is relevant for solar cells. The typical refractive index of a-Si:H(n) as a function of λ is also plotted for comparison and and shows that a-Si:H(n) is not suitable for index grading. In Fig. 5.17(b) the extinction coefficient (k) of the different materials is also shown as a function of λ. The k is related to the absorption coefficient (α) by $\alpha = \frac{4\pi k}{\lambda}$. In Fig. 5.17(b) it can be seen that for MgF_2 and SiN_x k is zero over the whole λ range and that for μc-SiC:H(n) k becomes larger than zero only for λ below 500 nm. The k becomes larger than zero already for λ of 750 nm for a-Si:H(n), which leads to high parasitic absorption and emphasizes the need to replace the commonly used a-Si:H(n) window layer in order to increase J_{sc}.

To maximize the absorbed sun light in the c-Si, it is necessary to find the optimum combination of all three thicknesses of the triple layer ARC. Therefore, the front stack was simulated with OPAL2 [107]. As input parameters the n_j and k values from Fig. 5.17 were used. In order to minimize the difference between simulated R and measured R of the textured c-Si surface without any film on top of it, the input parameters for OPAL2 of the c-Si surface morphology, the incident illumination, and the light trapping model were adjusted. The result is shown in Fig. 5.18(a) and the details can be found in the experimental part (see Chap. 3). The simulated R shows a good agreement with the measured R. Only for the short wavelength range below 400 nm there exists a mismatch. As the OPAL2 simulation does not take reflection at the back side of the wafer into account (light travels out), the simulated R for λ above 1000 nm cannot be used for further calculations of optical losses. For this reason, the R of the λ range of 300-855 nm was used for the quantification of the electrical current loss from the front side design. In Fig. 5.18(b-d), SEM images of a test structure are shown that was used to relate measured layer thicknesses to simulated layer thicknesses, in order to adjust the corresponding deposition times accordingly.

With all these pre-adjustments it was possible to produce, measure, and simulate the $MgF_2/SiN_x/\mu$c-SiC:H(n)/c-Si stack for μc-SiC:H(n) thicknesses (d_{SiC}) ranging

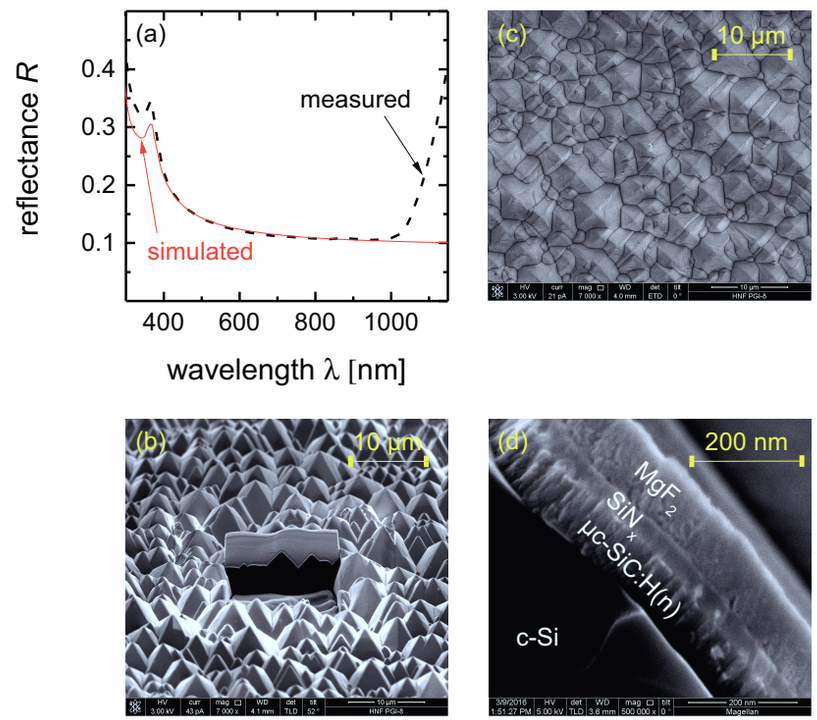

Figure 5.18.: *(a) Simulated and measured reflectance R of c-Si wafer surface which is textured by randomly distributed upside pyramids. The textured surface is pictured in (b) in side view and in (c) in top view. (d) cross section of $MgF_2/SiN_x/\mu c$-SiC:H(n)/c-Si stack.*

from 0-60 nm. The resulting simulated R and the measured R in Fig. 5.19(a-b) are in good agreement with one another, as the positions of local maxima and minima are similar. The measured R seem to be higher by an offset value of 0.01 for the absolute values. The reflection losses were quantified in form of current density loss for all results by integrating over the AM1.5 sun spectrum from 300-800 nm of wavelength. The simulated current density loss ($J_{\mathrm{sim}}^{\mathrm{ref}}$) as well as the measured reflection current density loss ($J_{\mathrm{mes}}^{\mathrm{ref}}$) are plotted for d_{SiC} of 0-60 nm in Fig. 5.19(c-d). Moreover the current density lost by parasitic absorption ($J_{\mathrm{sim}}^{\mathrm{abs}}$) is also calculated based on the extinction coefficient from Fig. 5.17(b) for the corresponding

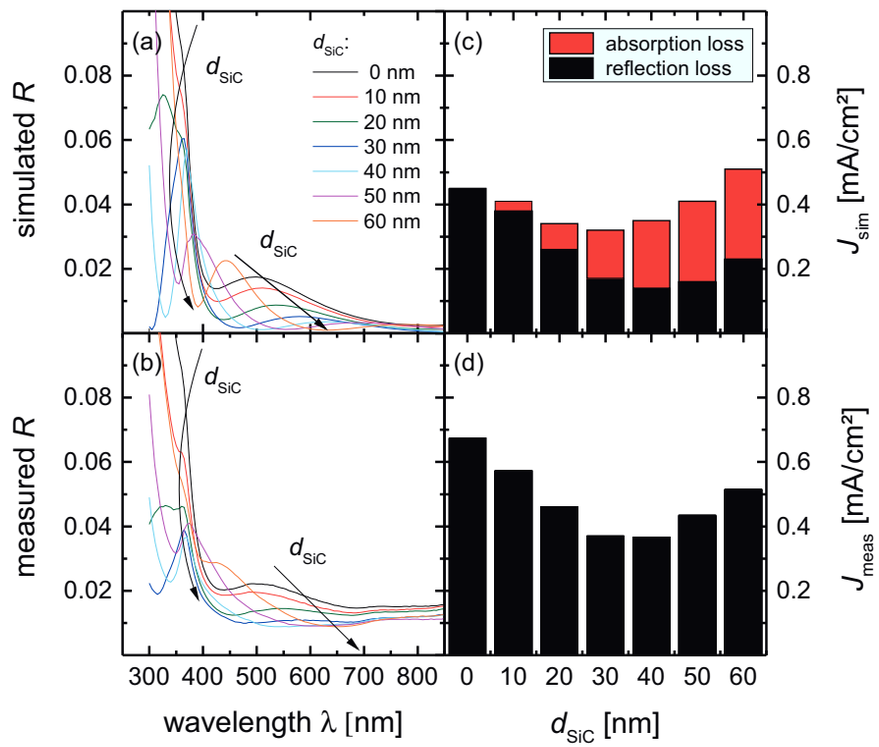

Figure 5.19.: *(a) Simulated and (b) measured reflectance R as a function of wavelength λ. (c) simulated current density loss J_{sim} and (d) measured current density loss J_{mes} as a function of the μc-SiC:H(n) film thickness d_{SiC}.*

d_{SiC} and added to Fig. 5.19(c). It can be observed that $J_{\mathrm{sim}}^{\mathrm{ref}}$ and $J_{\mathrm{mes}}^{\mathrm{ref}}$ decrease with increasing d_{SiC} up to 40 nm and that for larger d_{SiC} the densities increase again. The lowest value for $J_{\mathrm{sim}}^{\mathrm{ref}}$ is 0.14 mA/cm^2 and for $J_{\mathrm{mes}}^{\mathrm{ref}}$ is 0.37 mA/cm^2. Of course the $J_{\mathrm{sim}}^{\mathrm{abs}}$ increases with increasing d_{SiC}, but nevertheless the sum $J_{\mathrm{sim}}^{\mathrm{ref}}$ and $J_{\mathrm{sim}}^{\mathrm{abs}}$ is only 0.32 mA/cm^2 for d_{SiC} of 30 nm, whereas the lost total current density is 0.45 mA/cm^2 without μc-SiC:H(n) layer. To passivate the c-Si surface by SiN_x a different - not fully transparent - SiN_x material would need to be used. According to Aberle et al. [191] the nitrogen content in the SiN_x layer has to be increased to achieve high passivation quality which is accompanied by an increase of the n_{j} and

k values. Thus, parasitic absorption is increased and the refractive index matching is less favorable to minimize reflection. To estimate the J_{sc} for the introduced triple layer ARC for IBC-SHJ solar cells, a maximum current density of 43.57 mA/cm^2 is assumed which would be achieved if the entire AM1.5 sun spectrum is absorbed in 170 μm of c-Si. Consequently, using the total measured current density loss from the front side, i.e. within the wavelength range of 300-800 nm, a theoretical upper limit for J_{sc} is 43.05 mA/cm^2 with 30 nm for the μc-SiC:H(n) layer. This value represents the ideal case where charge carrier collection losses, recombination losses, as well as optical losses at the back side are zero in the IBC-SHJ solar cell. For comparison, the J_{sc} of the currently best silicon based solar cells are: 42.1 mA/cm^2 for Fraunhofer TOPCon [42], 42.3 mA/cm^2 for Kaneka [192], and 42.7 mA/cm^2 for UNSW PERL [163]. The comparison of these J_{sc} values emphasizes the high potential of the here presented $MgF_2/SiN_x/\mu$c-SiC:H(n)/c-Si front side design for IBC-SHJ solar cells which simultaneously provides high passivation quality of iV_{oc} above 710 mV.

6. Conclusion and Outlook

In this thesis, the material properties and process parameters of μc-SiC:H(n) materials were studied, in order to implement them as a window layer in SHJ solar cells. HWCVD and PECVD grown μc-SiC:H(n) materials offer very promising opto-electrical properties which are superior to the properties of the commonly used a-Si:H(n) and μc-SiO$_x$:H(n) materials. However, it was not fully understood how the structural properties are related to opto-electrical properties. Especially, for unintentionally doped μc-SiC:H(n) films, where no doping gas was added during the deposition, a large scattering of structural, electrical, and optical data had been observed in the past. Additionally, due to a high hydrogen radical density in the gas phase during the μc-SiC:H(n) growth common a-Si:H(i) passivation layers are strongly deteriorated. However, the high hydrogen radical density is needed to grow μc-SiC:H(n) material that fulfills the opto-electrical requirements for excellent window layer. Therefore, a successful implementation of μc-SiC:H(n) in SHJ solar cells was not possible so far. These issues concerning material and device are addressed in this thesis. In this last chapter, the main conclusions of this thesis are summarized and recommendations for future works are provided.

Microstructure of μc-SiC:H(n) Concerning the μc-SiC:H(n) material, the influence of the film microstructure on electrical and on the optical properties were investigated in detail. It was possible to increase the 3C-SiC grain size to 49 nm. Strong indications were found that the grain surfaces are terminated by Si-H. Thus, an increase in the 3C-SiC grain size lowers the the total hydrogen content as well as the silicon excess in the films, due to a reduced surface-volume fraction. An increase of the grain size was accompanied by an increase in electrical conductivity by 10 orders of magnitude. In accordance to the Seto model for polycrystalline silicon, larger

grain sizes reduce the average activation energy for the charge carrier density. As a consequence the increase in electrical conductivity is predominated by the increase in charge carrier density. Equally, the increase in charge carrier density can also be explained by a reduced passivation of donors by hydrogen atoms, due to a decreasing hydrogen content. Larger average grain sizes induce larger optical bandgaps, which were increased to 3.0 eV. Hence, an increase of the grain size is beneficial for high electrical conductivity and at the same time also for high transparency, which is an ideal combination for window layer material in solar cells.

Oxygen in μc-SiC:H(n) It was shown in this work that the large scattering in the past of the material data of unintentionally doped μc-SiC:H(n) was caused by different chamber conditions depending on the pre-history of the chamber. By increasing the base pressure of the vacuum chamber the oxygen content in the films increases significantly. The electrical conductivity rises strongly with increasing oxygen content. Oxygen, which might be located at the grain boundaries due to a low solubility in crystalline SiC, primarily lowers the potential barrier height at the grain boundaries. Consequently, the charge carrier mobility increases strongly whereas the increase in charge carrier density is limited with increasing oxygen content. The optical absorption coefficient increases strongly with increasing oxygen content over the entire photon energy range, due to the increased charge carrier density and the decreased order in microstructure. It was further demonstrated that is possible to increase the electrical conductivity in a controlled way by adding vaporized water. Using oxygen gas increased the electrical conductivity only very slightly and adding molecular carbon dioxide gas even decreased the electrical conductivity drastically. In both cases, the silicon carbide material transformed into oxycarbide material.

Nitrogen in μc-SiC:H(n) By adding pure nitrogen gas to the HWCVD process it was possible to increase the nitrogen content in the films. As compared to oxygen, nitrogen is very soluble in crystalline SiC so that a significant amount should also be located inside the SiC grains. With increasing nitrogen content the electrical conductivity increased strongly, due to an increase in charge carrier density as well as in charge carrier mobility. Increasing the grain size and the nitrogen content simultaneously lead to a conductivity of 10^1 S/cm which is the highest value for μc-

SiC:H(n) reported so far in literature. The optical absorption coefficient increased strongly with increasing nitrogen content over the entire photon energy range, as it was also the case with increasing oxygen content, due to the increased charge carrier density and the decreased order in microstructure.

μc-SiC:H(n) in a-SiO$_x$:H(i) passivated SHJ solar cells In order to implement μc-SiC:H(n) as window layer in SHJ solar cells, an a-SiO$_x$:H(i) passivation layer was protected by a μc-SiO$_x$:H(n) layer from hydrogen etching during the HWCVD growth of μc-SiC:H(n). Despite the etch-resistance, it was found that it is only possible to maintain a high passivation quality after μc-SiC:H(n) deposition if the filament temperature does not exceed 1800 °C. Otherwise strong blistering at the a-SiO$_x$:H(i)/c-Si interface deteriorated the passivation severely. This phenomenon can be attributed to the unfavorable expansion of micro-voids at the c-Si interface due to the in-diffusion of hydrogen atoms through the layer stack and the subsequent accumulation of molecular hydrogen in micro-voids at the a-SiO$_x$:H(i)/c-Si interface. Higher filament temperatures, i.e., 1900 °C and 2000 °C, are only possible to be used if either the crystalline volume fraction or the oxygen content of the μc-SiO$_x$:H(n) protection layer is high. A maximum active area efficiency of 18.9 % on a double side polished float zone p-type wafer was achieved with V_{oc} of 677 mV, J_{sc} of 37.6 mA/cm^2, and FF of 74.2 %.

μc-SiC:H(n) in SiO$_2$ passivated SHJ solar cells A tunnel oxide layer of about 1.3 nm was developed as alternative concept, in order to protect and at the same time passivate the c-Si surface. The SiO$_2$ layer combines a certain hydrogen etch resistivity and thermal resistivity which are process relevant advantages. The highest implied open circuit voltage value was 725 mV on double side polished float zone wafer and 711 mV on double side textured Czochralski wafer. Neither additional high temperature annealing treatment nor additional forming gas treatment was needed. Subsequently, two-side contacted SHJ solar cells with the μc-SiC:H(n)/SiO$_2$ layer combination at the illuminated side were produced by using double side textured Czochralski n-type wafers. A maximum active area efficiency of 17.6 % was achieved with V_{oc} of 665 mV, J_{sc} of 40.3 mA/cm^2, and FF of 65.8 %. The highest J_{sc} reached 40.9 mA/cm^2, which is an excellent value that underlines the potential

of highly transparent μc-SiC:H(n) as window layer in two-side contacted SHJ solar cells. Even higher J_{sc} are possible by using an IBC cell structure, as the front side does not participate in the electrical circuit anymore which provides more freedom to maximize the transparency of μc-SiC:H(n) as window layer. A $MgF_2/SiN_x/\mu$c-SiC:H(n) triple layer ARC was developed in this thesis which gave rise to very low optical losses of only 0.5 mA/cm^2 in the wavelength range of 300-800 nm. The resulting J_{sc} would correspond to an excellent value of 43.0 mA/cm^2 which can compete with the currently best single-junction, non-concentrator SHJ solar cells.

Outlook This work delivered a substantial basis for future optimizations of SHJ solar cells involving highly transparent μc-SiC:H(n) window layers and opened several paths for future investigations. The most important improvement is the implementation of an electrically more conductive μc-SiC:H(n) layer, no matter which front side structure concept is continued. For this purpose, increasing the grain size in 30-40 nm thick μc-SiC:H(n) layers is very important, because it increases the electrical conductivity but does not increases the parasitic absorption in the μc-SiC:H(n) layer. The parasitic absorption would increase if the electrical conductivity is increased by higher filament temperatures or higher doping (oxygen or nitrogen). Further investigations of controlled oxygen doping, e.g., by water vapor, in HWCVD grown μc-SiC:H(n) are rather of limited interest, because no optical advantage could be found as compared to nitrogen doped μc-SiC:H(n) films. It is probable, that once the electrical conductivity of μc-SiC:H(n) is not limiting the FF anymore, the tunnel probability through SiO_2 needs to be increased. This should be possible by decreasing the oxide thickness further, or by decreasing the offset between conduction band and Fermi level energy, e.g., by applying Cat-Doping [151] using HWCVD. Interestingly, Cat-Doping should simultaneously also improve the passivation quality by favorably increasing band bending at c-Si surface as reported by Matsumura et al. [151], so that larger open circuit voltages are expected. Further improvement of the chemical passivation may be realized by including an additional hydrogen treatment step using HWCVD. Finally, all these future improvements are equally attractive for two-side contacted as well as for IBC SHJ solar cells.

A. Abbreviations and Symbols

Variables and physical constants

α	optical absorption coefficient
$\alpha_{\mathbf{1eV}}$	sub-bandgap absorption at the photon energy of 1.0 eV
$\Delta E_{\mathbf{c}}$	conduction band offset
$\Delta E_{\mathbf{v}}$	valence band offset
Δn	n-type minority charge carriers
$d_{\mathbf{SiO2}}$	thickness of silicon dioxide layer
η	solar cell efficiency
λ	wavelength
μ	charge carrier mobility
ν	wavenumber
$\rho_{\mathbf{c}}$	contact resistivity
$\rho_{\mathbf{SiC}}$	resistivity of μc-SiC:H(n) film
Φ	hydrogen flux through SiO_2
σ	lateral electrical conductivity
$\tau_{\mathbf{eff}}$	effective carrier lifetime
$\tau_{\mathbf{bulk}}$	carrier lifetime in the bulk
$\tau_{\mathbf{surface}}$	carrier lifetime at the surface
A	absorptance
$c_{\mathbf{MMS}}$	monomethylsilane concentration
D	c-SiC density ($9.68 \cdot 10^{22}$ at/cm^3)
$D_{\mathbf{diff}}$	diffusion coefficient of hydrogen
$d_{\mathbf{f\text{-}s}}$	distance between filament and substrate
$D_{\mathbf{it}}$	defect density at the c-Si interface
$d_{\mathbf{j}}$	thickness of layer j

$d_{\mathbf{SiC}}$	film thickness measured by profilometer
E_{04}	optical bandgap
E_{μ}	activation energy of charge carrier mobility
$E_{\mathbf{A}}$	activation energy
$E_{\mathbf{B}}$	effective potential barrier height
$E_{\mathbf{C}}$	conduction band edge
$E_{\mathbf{F}}$	Fermi level
$E_{\mathbf{g}}$	bandgap energy
$E_{\mathbf{n}}$	activation energy of charge carrier density
EQE	external quantum efficiency
$E_{\mathbf{V}}$	valence band edge
$f_{\mathbf{CO2}}$	gas ratio of carbon dioxide
$F_{\mathbf{CO2}}$	flow rate carbon dioxide gas
FF	fill factor
$F_{\mathbf{H}}$	flow rate of hydrogen gas
$F_{\mathbf{MMS}}$	flow rate of monomethylsilane gas
$F_{\mathbf{N2}}$	flow rate of nitrogen gas
$\mathbf{h}$	Planck's constant
IQE	internal quantum efficiency
$I_{\mathbf{c}}$	crystallinity of silicon phase measured by Raman spectroscopy
$I_{\mathbf{sc}}$	short circuit current density
$I_{\mathbf{Si\text{-}C}}$	intensity of Si-C mode in FTIR spectroscopy
$\mathbf{i}FF$	implied fill factor
$\mathbf{i}V_{\mathbf{oc}}$	implied open circuit voltage
J	electrical current density
$J_{\mathbf{0}}$	saturation current density
$J_{\mathbf{R}}$	reflection loss in form of current density
$J_{\mathbf{ph}}$	photo-current density
$J_{\mathbf{sc}}$	short circuit current density
$J_{\mathbf{sim}}^{\mathbf{abs}}$	current density loss of parasitic absorption obtained by simulation
$J_{\mathbf{sim}}^{\mathbf{ref}}$	current density loss of parasitic reflection obtained by simulation
$J_{\mathbf{mes}}^{\mathbf{ref}}$	current density loss obtained from measured reflectance
k	extinction coefficient or imaginary part of complex refractive index

	from ellipsometer
$\mathbf{k_B}$	Boltzmann constant ($\approx 8.6 \cdot 10^{-5}$ eV)
L	hypothetical cubic grain size
$L_{\mathbf{SiC}}$	average 3C-SiC grain size
$m_{\mathbf{e}}$	tunneling mass of electrons
$m_{\mathbf{h}}$	tunneling mass of holes
n	charge carrier density
$N_{\mathbf{A}}$	acceptor doping concentration
$n_{\mathbf{i}}$	intrinsic charge carrier concentration
$n_{\mathbf{j}}$	refractive index of material j
p	deposition pressure
$P_{\mathbf{f}}$	forward power
p_{base}	base pressure in vacuum chamber
p_{leak}	leak pressure
$P_{\mathbf{max}}$	maximum generated power
$P_{\mathbf{sun}}$	sun power
$\mathbf{q}$	elementary charge
$r_{\mathbf{depo}}$	deposition rate
R	reflectance
$R_{\mathbf{s}}$	series resistance
$R_{\mathbf{sh}}$	shunt resistance
S	thermopower
T	temperature
$t_{\mathbf{anneal}}$	accumulated annealing time
$t_{\mathbf{acc}}$	accumulated deposition time of several depositions
$t_{\mathbf{depo}}$	deposition time
$t_{\mathbf{HNO3}}$	duration of dipping in 69 % nitric acid solution
$T_{\mathbf{f}}$	filament temperature
$T_{\mathbf{H}}$	heater temperature
V	voltage potential
$V_{\mathbf{oc}}$	open circuit voltage
$V_{\mathbf{s}}$	volume of surface layer of c-SiC grain
X	carbon fraction of μc-$Si_{1-x}C_x$:H

Material and elements

:H	hydrogenated
μc-	microcrystalline
a-	amorphous
Al	aluminum
Ag	silver
B	boron
c-	crystalline
C	carbon
H	hydrogen
[H]	hydrogen concentration in μc-SiC:H film
N	nitrogen
[N]	nitrogen concentration in μc-SiC:H film
O	Oxygen
[O]	oxygen concentration in μc-SiC:H film
CO_2	carbon dioxide
H_2	molecular hydrogen
H_2O	water
HNO_3	nitric acid solution
H_3SiCH_3	monomethylsilane
(i)	intrinsic
(n)	n-type doped
N_2	molecular nitrogen
O_2	molecular oxygen
(p)	p-type doped
P	phosphorus
PH_3	phosphine
Si	silicon
SiC	silicon carbide
SiH	mono-hydride
SiH_2	dihydride
SiH_4	silane
SiN_x	sub-stoichiometric silicon nitride

SiO_2	silicon dioxide
SiO_x	sub-stoichiometric silicon oxide

Abbreviations

AM	air-mass
ARC	anti-reflection coating
BSF	back surface field
Cz	Czochralski
DB	dangling bond
FGA	forming gas annealing
FWHM	full width at half maximum
FTIR	Fourier transform infrared spectroscopy
Fz	float zone
HF	hydrofluoric acid (1% diluted)
HWCVD	hot wire chemical vapor deposition
IBC	interdigitated back contact
ITO	indium tin oxide
IV	current-voltage
MMS	monomethylsilane (CH_3SiH_3)
NAOS	nitric acid oxidation of Si
NGA	nitrogen gas annealing
PDS	photothermal deflection spectroscopy
PECVD	plasma enhanced chemical vapor deposition
PERL	passivated emitter and rear locally diffused
PL	photoluminescence
PV	photovoltaics
PVD	physical vapor deposition
QSSPC	quasi steady-state photo conductance
RBS	Rutherford back-scattering spectrometry
RCA	standard cleaning process developed at Radio Corporation of America
RT	room temperature
SEM	scanning electron microscopy

SHJ	silicon heterojunction
SIMS	secondary ion mass spectrometry
SRH	Shockley-Read-Hall
TCO	transparent conducting oxide
TEM	transmission electron microscopy
TLM	transfer length method
TOPCon	tunnel oxide passivated contact
VHF	very high frequency
XRD	X-Ray diffraction

B. List of publications

Publications related to this work

1. M. Pomaska, W. Beyer, E. Neumann, F. Finger, and K. Ding, *Impact of microcrystalline silicon carbide growth using hot-wire chemical vapor deposition on crystalline silicon surface passivation*, Thin Solid Films **595**, Part B, 217 – 220 (2015)
2. M. Pomaska, F. Köhler, U. Zastrow, J. Mock, F. Pennartz, S. Muthmann, O. Astakhov, R. Carius, F. Finger, and K. Ding, *New insight into the microstructure and doping of unintentionally n-type microcrystalline silicon carbide*, Journal of Applied Physics **119**, 17, 175303 (2016)
3. M. Pomaska, J. Mock, F. Köhler, U. Zastrow, M. Perani, O. Astakhov, D. Cavalcoli, R. Carius, F. Finger, and K. Ding, *Role of oxygen and nitrogen in n-type microcrystalline silicon carbide grown by hot wire chemical vapor deposition*, Journal of Applied Physics **120**, 22, 225105 (2016)
4. M. Pomaska, A. Richter, F. Lentz, F. Niermann, F. Finger, U. Rau, and K. Ding, *Wide Gap Microcrystalline Silicon Carbide Emitter for a-SiOx:H/c-Si Heterojunction Solar Cells*, Japanese Journal of Applied Physics **56**, 2, 022302 (2017)

Other publications

1. K. Ding, M. Pomaska, A. Singh, F. Lentz, F. Finger, and U. Rau, *Mechanism for crystalline Si surface passivation by the combination of SiO2 tunnel oxide and μc-SiC:H thin film*, physica status solidi - Rapid Research Letters **10**, No. 3, 233 – 236 (2016)

2. M. Smeets, M. Ermes, M. Pomaska, K. Ding, U.W. Paetzold, and K. Bittkau, *Nanophotonic Light Management for Silicon Heterojunction Solar Cells with Planar Passivation Layers - Implementation and Material Perspective*, Optical Nanostructures and Advanced Materials for Photovoltaics - Conference paper (2016)

C. Curriculum Vitae

Personal details

Name	Manuel Bernhard Pomaska
Date of birth	April 5th, 1989
Place of birth	Berlin, Germany
Citizenship	German/ Portuguese

Education

1995-1999	Grundschule Am Königsgraben, Berlin
1999-2007	Französisches Gymnasium, Berlin
2007-2010	Bachelor of Science in Physics at the Freie Universität Berlin
	Bachelor thesis at Institute of Physics
	Title: *Dynamic magnetic domains*
2010-2013	Master of Science in Physics at the Freie Universität Berlin
	Main subject: solid state physics and photovoltaics
	Master thesis at Helmholtz Zentrum Berlin,
	Institute for Heterogeneous Materialsystems
	Title: *Impact of Indium precursor solutions*
	on ILGAR-In2S3 buffer layers
	and the resulting Cu(In,Ga)(S,Se)2 solar cells
2014-2017	PhD thesis at the Forschungszentrum Jülich GmbH,
	IEK5-Photovoltaics

References

[1] H. Wirth, Aktuelle Fakten zur Photovoltaik in Deutschland - Fraunhofer ISE, 2017.

[2] F. M. for Economic Affairs and Energy of Germany, First "Energy Transition" Progress Report - Summary, 2014.

[3] D. M. Chapin, C. S. Fuller, and G. L. Pearson, Journal of Applied Physics **25**, 676 (1954).

[4] W. Shockley and H. J. Queisser, Journal of Applied Physics **32**, 510 (1961).

[5] F. Roca, J. Cárabe, and A. Jäger-Waldau, Silicon heterojunction cells R&D in Europe, in *Proceedings of the 19th EU-PVSEC*, 2004.

[6] pv.energytrend.com (2016).

[7] M. A. Green et al., Prog. Photovolt: Res. Appl. **25**, 3 (2017).

[8] S. Miyajima, A. Yamada, and M. Konagai, Jpn. J. Appl. Phys. **46**, 1415 (2007).

[9] F. Finger et al., Thin Solid Films **517**, 3507 (2009).

[10] S. Miyajima, Heterojunction crystalline silicon solar cells using nanocrystalline cubic silicon carbide emitter, in *2014 21st International Workshop on Active-Matrix Flatpanel Displays and Devices (AM-FPD)*, pages 65–68, 2014.

[11] J. Irikawa, S. Miyajima, T. Watahiki, and M. Konagai, Appl. Phys. Express **4**, 092301 (2011).

[12] S. Miyajima, M. Sawamura, A. Yamada, and M. Konagai, Journal of Non-Crystalline Solids **354**, 2350 (2008).

[13] A. Einstein, Analen der Physik **17**, 17 (1905).

[14] The Nobel Prize in Physics 1921.

[15] C. Kittel, *Introduction to Solid State Physics*, Wiley, 8th edition, 2005.

[16] P. Würfel, Photons, in *Physics of Solar Cells*, pages 9–35, Wiley-VCH Verlag GmbH, 2005.

[17] U. Würfel, A. Cuevas, and P. Würfel, IEEE Journal of Photovoltaics **5**, 461 (2015).

[18] M. Green, *Third Generation Photovoltaics: Advanced Solar Energy Conversion*, Springer Science & Business Media, 2006.

[19] C. Gueymard, SMARTS2, A Simple Model of the Atmospheric Radiative Transfer of Sunshine: Algorithms and performance assessment, Technical report, Florida Solar Energy Center, 1679 Clearlake Road Cocoa, Florida 32922-5703, 1995.

[20] M. A. Green, *Solar Cells - Operating Principles, Technology and System Applications*, The University of New South Wales, New South Wales, 1st edition, 1992.

[21] M. A. Green, *Silicon Solar Cells: Advanced Principles & Practice*, Centre for Photovoltaic Devices and Systems, University of New South Wales, 1995.

[22] A. Cuevas et al., Skin care for healthy silicon solar cells, in *2015 IEEE 42nd Photovoltaic Specialist Conference (PVSC)*, pages 1–6, 2015.

[23] J. Schmidt, M. Kerr, and A. Cuevas, Semicond. Sci. Technol. **16**, 164 (2001).

[24] J. Schmidt et al., Energy Procedia **15**, 30 (2012).

[25] A. G. Aberle, Prog. Photovolt: Res. Appl. **8**, 473 (2000).

[26] B. L. Sopori et al., Solar Energy Materials and Solar Cells **41–42**, 159 (1996).

[27] B. Sopori, M. I. Symko, R. Reedy, K. Jones, and R. Matson, Mechanism(s) of hydrogen diffusion in silicon solar cells during forming gas anneal, in *Conference Record of the Twenty Sixth IEEE Photovoltaic Specialists Conference - 1997*, pages 25–30, 1997.

[28] W. G. J. H. M. van Sark, L. Korte, and F. Roca, *Physics and Technology of Amorphous-Crystalline Heterostructure Silicon Solar Cells*, Springer, 2012.

[29] J. Zhao, A. Wang, and M. A. Green, Solar Energy Materials and Solar Cells **65**, 429 (2001).

[30] M. A. Green, K. Emery, Y. Hishikawa, W. Warta, and E. D. Dunlop, Progress in Photovoltaics: Research and Applications - Wiley Online Library **22**, 1 (2013).

[31] D. Adachi, J. L. Hernández, and K. Yamamoto, Applied Physics Letters **107**, 233506 (2015).

[32] M. Taguchi et al., IEEE Journal of Photovoltaics **4**, 96 (2014).

[33] F. Feldmann et al., Solar Energy Materials and Solar Cells **131**, 46 (2014).

[34] P. Stradins, A. Rohatgi, and S. Glunz, Passivated tunneling contacts to n-type wafer and their implementation into high performance solar cells, in *Proceedings of 6th World Conference on Photovoltaic Energy Conversion*, Kyoto, Japan, 2014.

[35] B. G. Lee, Achieving Ultra-High Efficiency Silicon Solar Cells: Passivated Contacts and Advanced Optics, in *Presentaion given in Jülich*, 2014.

[36] R. Peibst et al., 32nd European Photovoltaic Solar Energy Conference and Exhibition , 323 (2016).

[37] G. Yang, A. Ingenito, O. Isabella, and M. Zeman, Solar Energy Materials and Solar Cells **158, Part 1**, 84 (2016).

[38] F. Feldmann, C. Reichel, R. Müller, and M. Hermle, Solar Energy Materials and Solar Cells **159**, 265 (2017).

[39] C. Reichel et al., Journal of Applied Physics **118**, 205701 (2015).

[40] R. Peibst et al., Solar Energy Materials and Solar Cells **158, Part 1**, 60 (2016).

[41] H. Steinkemper, F. Feldmann, M. Bivour, and M. Hermle, Energy Procedia **77**, 195 (2015).

[42] S. Glunz et al., Proceedings of the 31h European Photovoltaic Solar Energy Conference, Hamburg, Germany, September 14 - 18, 2015 (2015).

[43] D. D. Smith et al., Silicon solar cells with total area efficiency above 25 %, in *2016 IEEE 43rd Photovoltaic Specialists Conference (PVSC)*, pages 3351–3355, 2016.

[44] C. Schinke et al., AIP Advances **5**, 067168 (2015).

[45] Z. C. Holman et al., IEEE Journal of Photovoltaics **2**, 7 (2012).

[46] J. Hotovy et al., Applied Surface Science **269**, 81 (2013).

[47] Y. Hishikawa, S. Tsuda, K. Wakisaka, and Y. Kuwano, Journal of Applied Physics **73**, 4227 (1993).

[48] R. A. Street, 5 Substitutional doping, in *Hydrogenated amorphous silicon*, Cambridge solid state science series., pages 224–275, Cambridge University Press, Cambridge, 1991.

[49] A. Richter, F. Lentz, M. Meier, F. Finger, and K. Ding, Phys. Status Solidi A **213**, 1976 (2016).

[50] K. Ding et al., Japanese Journal of Applied Physics **52**, 122304 (2013).

[51] A. Lambertz et al., Solar Energy Materials and Solar Cells **119**, 134 (2013).

[52] A. Lambertz, F. Finger, B. Holländer, J. K. Rath, and R. E. I. Schropp, Journal of Non-Crystalline Solids **358**, 1962 (2012).

[53] H. Tan, P. Babal, M. Zeman, and A. H. M. Smets, Solar Energy Materials and Solar Cells **132**, 597 (2015).

[54] P. Cuony et al., Appl. Phys. Lett. **97**, 213502 (2010).

[55] S. Miyajima, M. Sawamura, A. Yamada, and M. Konagai, Japanese Journal of Applied Physics **46**, L693 (2007).

[56] S. Kirner, *Development of wide band gap materials for thin film silicon solar cells*, PhD thesis, TU Berlin, Berlin, 2013.

[57] T. Rajagopalan et al., Journal of Applied Physics **94**, 5252 (2003).

[58] D. Hamashita, Y. Kurokawa, and M. Konagai, Energy Procedia **10**, 14 (2011).

[59] D. Hamashita, Y. Kurokawa, and M. Konagai, MRS Online Proceedings Library Archive **1426**, 347 (2012).

[60] D. Hamashita, S. Miyajima, and M. Konagai, Solar Energy Materials and Solar Cells **107**, 46 (2012).

[61] T. Chen, F. Köhler, A. Heidt, R. Carius, and F. Finger, Jpn. J. Appl. Phys. **53**, 05FM04 (2014).

[62] F. S. Tehrani and S. A. Rahman, J Mater Sci: Mater Electron **25**, 2366 (2014).

[63] T. Chen, Y. Huang, D. Yang, R. Carius, and F. Finger, phys. stat. sol. (RRL) **2**, 160 (2008).

[64] E. G. Acheson, Chem. News **68** (1893).

[65] H. R. Philipp, Phys. Rev. **111**, 440 (1958).

[66] L. Patrick and W. J. Choyke, Phys. Rev. **186**, 775 (1969).

[67] H. Morkoç et al., Journal of Applied Physics **76**, 1363 (1994).

[68] D. Bimberg, M. Altarelli, and N. O. Lipari, Solid State Communications **40**, 437 (1981).

[69] A. R. Verma and P. Krishna, *Polymorphism and Polytypism in Crystals*, Wiley, N. Y., 1966.

[70] H. Matsunami and T. Kimoto, Materials Science and Engineering: R: Reports **20**, 125 (1997).

[71] W. J. Choyke, H. Matsunami, and G. Pensl, *Silicon Carbide - Recent Major Advances*, Springer Berlin Heidelberg, 2014.

[72] S. Klein, A. Dasgupta, F. Finger, R. Carius, and T. Bronger, Thin Solid Films **516**, 630 (2008).

[73] F. Köhler et al., Journal of Non-Crystalline Solids **358**, 2011 (2012).

[74] F. Köhler, *Zur Mikrostruktur siliziumbasierter Dünnschichten für die Photovoltaik*, PhD thesis, Publikationsserver der RWTH Aachen University, Jülich, 2012.

[75] A. A. Lebedev, Semiconductors **33**, 107 (1999).

[76] S. Miyajima, K. Haga, A. Yamada, and M. Konagai, Japanese Journal of Applied Physics **45**, L432 (2006).

[77] N. Yoshida et al., Phys. Status Solidi (c) **7**, 790 (2010).

[78] Y. Hoshide, A. Tabata, A. Kitagawa, and A. Kondo, Thin Solid Films **517**, 3524 (2009).

[79] T. Chen et al., Thin Solid Films **519**, 4511 (2011).

[80] T. Chen, *Microcrystalline Silicon Carbide Thin Films Prepared by Hot-Wire Chemical Vapor Deposition and Their Application in Silicon Thin Film Solar*

Cells, PhD thesis, IEK5 - Forschungszentrum Juelich GmbH, Jülich, 2013.

[81] C. Sellmer, T. Bronger, W. Beyer, and R. Carius, Phys. Status Solidi (c) **7**, 670 (2010).

[82] P. Torres et al., Applied Physics Letters **69**, 1373 (1996).

[83] C. Banerjee et al., Japanese Journal of Applied Physics **46**, 1 (2007).

[84] S. Miyajima, J. Irikawa, A. Yamada, and M. Konagai, Applied Physics Letters **97**, 023504 (2010).

[85] W. Kern, 1 - Overview and Evolution of Silicon Wafer Cleaning Technology, in *Handbook of Silicon Wafer Cleaning Technology (Second Edition)*, pages 3–92, William Andrew Publishing, Norwich, NY, 2008.

[86] B. C. Smith, *Fundamentals of Fourier Transform Infrared Spectroscopy, Second Edition*, CRC Press, 2011.

[87] L. Calcagno, F. Giorgis, A. Makthari, P. Musumeci, and F. Pirri, Philosophical Magazine Part B **79**, 1685 (1999).

[88] M. Cardona, phys. stat. sol. (b) **118**, 463 (1983).

[89] S. W. King, J. Bielefeld, M. French, and W. A. Lanford, Journal of Non-Crystalline Solids **357**, 3602 (2011).

[90] F. Demichelis and C. F. Pirri, Solid State Phenomena **44-46**, 385 (1995).

[91] A. A. Langford, M. L. Fleet, B. P. Nelson, W. A. Lanford, and N. Maley, Phys. Rev. B **45**, 13367 (1992).

[92] P. Zalm, Vacuum **45**, 753 (1994).

[93] R. G. Wilson, F. A. Stevie, and C. W. Magee, Secondary Ion Mass Spectrometry - A practical Handbook for Depth Profiling and Bulk Impurity Analysis, pages 3.1–1, John Wiley & Sons, 1989.

[94] Y. Gao, Journal of Applied Physics **64**, 3760 (1988).

[95] H. Gnaser, Journal of Vacuum Science & Technology A **12**, 452 (1994).

[96] F. Caccavale, G. Brusatin, and I. Kleps, Applied Surface Science **81**, 443 (1994).

[97] J. I. Langford and A. J. C. Wilson, J. Appl. Cryst. **11**, 102 (1978).

[98] W. Beyer and H. Overhof, Chapter 8 Doping Effects in a-Si: H, in *Semiconductors and Semimetals*, edited by J. I. Pankove, volume 21, Part C of *Hydrogenated Amorphous SiliconElectronic and Transport Properties*, pages 257–307, Elsevier, 1984.

[99] C. Sellmer, *Untersuchung der Ladungsträgerkonzentration und -beweglichkeit in mikrokristallinen Siliziumlegierungen mit Hall-Effekt und Thermokraft 2011-09-27*, PhD thesis, Publikationsserver der RWTH Aachen University, Jülich, 2011.

[100] R. A. Street, 7 Electronic transport, in *Hydrogenated amorphous silicon*, Cambridge solid state science series., pages 224–275, Cambridge University Press, Cambridge, 1991.

[101] J. Mock, *Fehlstellendotierung von Eisenoxid- und Bismutsulfid-Nanopartikeln*, PhD thesis, RWTH Aachen University, Jülich, 2017.

[102] W. B. Jackson, N. M. Amer, A. C. Boccara, and D. Fournier, Applied Optics **20**, 1333 (1981).

[103] H. Fujiwara, *Spectroscopic Ellipsometry: Principles and Applications*, John Wiley & Sons, 2007.

[104] R. A. Sinton and A. Cuevas, Applied Physics Letters **69**, 2510 (1996).

[105] W. Reetz, H. Stiebig, and T. Brammer, Spectral responce of stacked solar cells based on a-Si:H, in *Proceedings of the 2nd ISEC-Europe Solar Congress*, pages V.1.5–1, 1999.

[106] B. Turan, *Laser processing for the integrated series connection of thin-film silicon solar cells*, PhD thesis, RWTH Aachen University, Jülich, 2016.

[107] S. C. Baker-Finch and K. R. McIntosh, A freeware program for precise optical analysis of the front surface of a solar cell, in *2010 35th IEEE Photovoltaic Specialists Conference (PVSC)*, pages 002184–002187, 2010.

[108] S. Kerdiles, F. Berthelot, F. Gourbilleau, and R. Rizk, Appl. Phys. Lett. **76**, 2373 (2000).

[109] T. Chen et al., Thin Solid Films **517**, 3513 (2009).

[110] S. Miyajima, A. Yamada, and M. Konagai, Japanese Journal of Applied

Physics **43**, L1190 (2004).

[111] A. Dasgupta et al., Thin Solid Films **516**, 618 (2008).

[112] S. Klein, L. Houben, R. Carius, F. Finger, and W. Fischer, Journal of Non-Crystalline Solids **352**, 1376 (2006).

[113] A. Heidt et al., J. Phys.: Conf. Ser. **326**, 012019 (2011).

[114] O. Vetterl et al., Solar Energy Materials and Solar Cells **62**, 97 (2000).

[115] M. Pomaska et al., Journal of Applied Physics **119**, 175303 (2016).

[116] N. W. Ashcroft and N. D. Mermin, *Solid state physics*, Saunders College, 1976.

[117] H. Umemoto et al., Journal of Applied Physics **91**, 1650 (2002).

[118] H. Matsumura and K. Ohdaira, ECS Trans. **25**, 53 (2009).

[119] E. V. Johnson, S. Pouliquen, P. A. Delattre, and J. P. Booth, Journal of Non-Crystalline Solids **358**, 1974 (2012).

[120] A. Dasgupta et al., Thin Solid Films **516**, 622 (2008).

[121] J. Geissbühler et al., Applied Physics Letters **102**, 231604 (2013).

[122] H. N. Wanka and M. B. Schubert, J. Phys. D: Appl. Phys. **30**, L28 (1997).

[123] N. H. Nickel, Journal of Vacuum Science & Technology B **18**, 1770 (2000).

[124] H. Umemoto, Thin Solid Films **575**, 3 (2015).

[125] R. A. Causey, J. D. Fowler, C. Ravanbakht, T. S. Elleman, and K. Verghese, Journal of the American Ceramic Society **61**, 221 (1978).

[126] A. Heidt, *Lokale strukturelle und elektronische Eigenschaften mikrokristalliner Siliziumkarbidverbindungen für die Dünnschichtphotovoltaik*, PhD thesis, Publikationsserver der RWTH Aachen University, Jülich, 2013.

[127] R. G. Wilson, F. A. Stevie, and C. W. Magee, Appendix, in *Secondary Ion Mass Spectrometry*, page App. C.3, John Wiley & Sons, USA, 1989.

[128] H. Iwata, U. Lindefelt, S. Öberg, and P. R. Briddon, Microelectronics Journal **34**, 371 (2003).

[129] F. Gendron, L. M. Porter, C. Porte, and E. Bringuier, Applied Physics Letters **67**, 1253 (1995).

[130] A. Gali, P. Deák, N. T. Son, and E. Janzén, Applied Physics Letters **83**, 1385 (2003).

[131] P. Deák, A. Gali, and B. Araadi, Hydrogen in SiC, in *Silicon carbide Recent Major Advances*, pages 57–88, Springer, 2004.

[132] J. Y. W. Seto, Journal of Applied Physics **46**, 5247 (1975).

[133] T. Chen, D. Yang, R. Carius, and F. Finger, Thin Solid Films **519**, 4516 (2011).

[134] J. W. Orton and M. J. Powell, Rep. Prog. Phys. **43**, 1263 (1980).

[135] J. W. Orton, Thin Solid Films **86**, 351 (1981).

[136] L. L. Kazmerski, 3 - Electrical Properties of Polycrystalline Semiconductor Thin Films, in *Polycrystalline and Amorphous Thin Films and Devices*, pages 59–133, Academic Press, 1980.

[137] N. Sommer, J. Hüpkes, and U. Rau, Phys. Rev. Applied **5**, 024009 (2016).

[138] R. A. Smith, *Semiconductors*, University Press, 1961.

[139] D. K. Schroder, R. N. Thomas, and J. C. Swartz, IEEE Journal of Solid-State Circuits **13**, 180 (1978).

[140] H.-J. Rost, D. Schulz, and D. Siche, High Nitrogen Doping During Bulk Growth, in *Silicon carbide Recent Major Advances*, pages 163–178, Springer, 2004.

[141] T. Dalibor et al., Materials Science and Engineering: B **61-62**, 454 (1999).

[142] T. Kinoshita, M. Isomura, Y. Hishikawa, and S. Tsuda, Japanese Journal of Applied Physics **35**, 3819 (1996).

[143] T. Kamei and T. Wada, Journal of Applied Physics **96**, 2087 (2004).

[144] T. Kamei, M. Kondo, and A. Matsuda, Japanese Journal of Applied Physics **37**, L265 (1998).

[145] T. Kilper et al., Journal of Applied Physics **105**, 074509 (2009).

[146] M. Pomaska et al., Journal of Applied Physics **120**, 225105 (2016).

[147] A. Tabata, Y. Hoshide, and A. Kondo, Materials Science and Engineering: B **175**, 201 (2010).

[148] M. d. Ventra and S. T. Pantelides, Journal of Elec Materi **29**, 353 (2000).

[149] A. Kozlovskyi, A. Semenov, and S. Skorik, Superlattices and Microstructures **100**, 596 (2016).

[150] M. Pomaska et al., Jpn. J. Appl. Phys. **56**, 022302 (2017).

[151] H. Matsumura et al., Journal of Applied Physics **116**, 114502 (2014).

[152] T. Sato, T. Sugiura, M. Ohtsubo, S. Matsuno, and M. Konagai, Jpn. J. Appl. Phys. **46**, 6796 (2007).

[153] F. Einsele, W. Beyer, and U. Rau, Phys. Status Solidi (c) **7**, 1021 (2010).

[154] K. Ding, U. Aeberhard, F. Finger, and U. Rau, Phys. Status Solidi RRL **6**, 193 (2012).

[155] M. Pomaska, W. Beyer, E. Neumann, F. Finger, and K. Ding, Thin Solid Films **595, Part B**, 217 (2015).

[156] K. Tonokura, K. Inoue, and M. Koshi, Journal of Non-Crystalline Solids **299-302, Part 1**, 25 (2002).

[157] W. Beyer, Solar Energy Materials and Solar Cells **78**, 235 (2003).

[158] W. Beyer, Phys. Status Solidi A **213**, 1661 (2016).

[159] R. Rizk, P. de Mierry, D. Ballutaud, M. Aucouturier, and D. Mathiot, Phys. Rev. B **44**, 6141 (1991).

[160] A. Richter, L. Zhao, F. Finger, and K. Ding, Surface and Coatings Technology **295**, 119 (2016).

[161] F. Einsele, *Amorphe Siliziumoxidschichten zur Oberflächenpassivierung und Kontaktierung von Heterostruktur-Solarzellen aus amorphem und kristallinem Silizium*, PhD thesis, RWTH Aachen University, Jülich, 2010.

[162] M. Meier et al., Prog. Photovolt: Res. Appl. **22**, 1226 (2014).

[163] J. Zhao, A. Wang, M. A. Green, and F. Ferrazza, Applied Physics Letters **73**, 1991 (1998).

[164] Y. Lee, W. Oh, V. A. Dao, S. Q. Hussain, and J. Yi, International Journal of Photoenergy **2012**, e753456 (2012).

[165] B. Stegemann et al., Applied Surface Science **395**, 78 (2017).

[166] P. Panek, K. Drabczyk, A. Focsa, and A. Slaoui, Materials Science and Engineering: B **165**, 64 (2009).

[167] M. R. Amirzada, A. Tatzel, V. Viereck, and H. Hillmer, Appl Nanosci **6**, 215 (2016).

[168] O. M. Hikaru Kobayashi Asuha, Journal of Applied Physics **94**, 7328 (2003).

[169] H. Angermann, W. Henrion, M. Rebien, and A. Röseler, Solar Energy Materials and Solar Cells **83**, 331 (2004).

[170] A. Moldovan et al., Solar Energy Materials and Solar Cells **142**, 123 (2015).

[171] T. Oikawa, K. Ohdaira, K. Higashimine, and H. Matsumura, Current Applied Physics **15**, 1168 (2015).

[172] S. Bordihn et al., Energy Procedia **8**, 654 (2011).

[173] Y. Tao et al., Prog. Photovolt: Res. Appl. **24**, 830 (2016).

[174] T. Matsumoto et al., Solar Energy Materials and Solar Cells **134**, 298 (2015).

[175] F. Feldmann, M. Bivour, C. Reichel, M. Hermle, and S. W. Glunz, Solar Energy Materials and Solar Cells **120, Part A**, 270 (2014).

[176] H. Angermann et al., Applied Surface Science **254**, 3615 (2008).

[177] H. Angermann, J. Rappich, and C. Klimm, Centr. Eur. J. Phys. **7**, 363 (2009).

[178] H. Angermann, Applied Surface Science **312**, 3 (2014).

[179] H. Angermann et al., Solid State Phenomena **255**, 331 (2016).

[180] A. D. Upadhyaya et al., IEEE Journal of Photovoltaics **6**, 153 (2016).

[181] K. Ding et al., Phys. Status Solidi RRL **10**, 233 (2016).

[182] I. Pressemitteilungen, Siliziumsolarzelle des ISFH erzielt 25% Wirkungsgrad mit passivierenden POLO Kontakten Institut für Solarenergieforschung, 2016.

[183] H. Nagayoshi et al., Jpn. J. Appl. Phys. **35**, L1047 (1996).

[184] S. Janz, S. Riepe, M. Hofmann, S. Reber, and S. Glunz, Applied Physics Letters **88**, 133516 (2006).

[185] M. Boccard and Z. C. Holman, Journal of Applied Physics **118**, 065704 (2015).

[186] J. Stuckelberger et al., Solar Energy Materials and Solar Cells **158, Part 1**, 2 (2016).

[187] A. Tomasi et al., IEEE Journal of Photovoltaics **4**, 1046 (2014).

[188] K. Yoshikawa et al., 6 inch High efficiency back contact crystalline Si solar cell applying heterojunction and thinfilm technology, in *2016 IEEE 43rd Photovoltaic Specialists Conference (PVSC)*, pages 3366–3369, 2016.

[189] M. Lu, S. Bowden, U. Das, and R. Birkmire, Appl. Phys. Lett. **91**, 063507 (2007).

[190] E. Palik, *Handbook of Optical Constants of Solids - 1st Edition*, Academic Press, 2012.

[191] A. Aberle et al., Energy Procedia **15**, 78 (2012).

[192] K. Yoshikawa et al., Nature Energy **2**, 17032 (2017).

Acknowledgments

I would like to express my deep gratitude to all those who made this work possible. Special thanks go to:

- Prof. Dr. Uwe Rau for the supervision and examination of this thesis, for providing the opportunity to work at his institution and for his constant confidence in me.
- Prof. Dr. Hideki Matsumura for the external mentoring and examination of this thesis and the wonderful time in Kanazawa.
- Dr. Kaining Ding for being an excellent supervisor.
- Dr. Friedhelm Finger and Prof. Dr. Reinhard Carius for participating to the regular silicon carbide meetings and contributing to this thesis with skeptical questions.
- Dr. Wolfhard Beyer for many fruitful and enlightening discussions.
- Dr. Oleksandr Astakhov, Dr. Florian Köhler, and Uwe Zastrow for sharing their knowledge of microcrystalline silicon carbide, discussing the data, and contributing to the publications related to this work.
- Dr. Stefan Muthmann for being a professional example.
- Jan Mock who supervised all thermopower measurements, was a open-minded discussion partner during, and became a good friend to me.
- Aryak Singh who initially helped me to develop the tunnel oxide for this thesis and who became an amazing friend to me.
- Dr. Alexandre Zamchiy and Malte Köhler for helping me with the development of tunnel oxide at its later stage.
- Manuela Meyer and Silke Lynen for their loyal, permanently reliable, and

excellent help.

- Johannes Wolff, Andreas Schmalen, Frank Pennartz and Sven Schiffer for fruitful discussions and technical support.
- Josef Klomfaß and Oliver Thimm for their effort of determining the optical absorption coefficient for me with PDS.
- For the IEK-5 football team, Photonensturm, who played an unforgettable season finishing third.
- My office mates Florian Lentz, Florian Staub and Alexei Richter for the amazing time inside as well as outside our office and their friendship.
- My beloved girlfriend for the mental support during the PhD.
- My family who built the educational basis which brought me to where I am now.

Band / Volume 379
Charakterisierung und Modifizierung von Kupferoxid- und Kupfersulfid-Nanopartikeln für Dünnschichtsolarzellen
J. Flohre (2017), 141, iii pp
ISBN: 978-3-95806-241-2

Band / Volume 380
Einzelfaserkomposite aus Pulvermetallurgischem Wolfram-faserverstärktem Wolfram
B. Jasper (2017), v, 92, XVIII pp
ISBN: 978-3-95806-248-1

Band / Volume 381
Untersuchungen zur Deckschichtbildung auf $LiNi_{0,5}Mn_{1,5}O_4$-Hochvoltkathoden
Die Kathoden/Elektrolyt-Grenzfläche in Hochvolt-Lithium-Ionen-Batterien
K. Wedlich (2017), xvi, 157, xvii-xxvi pp
ISBN: 978-3-95806-249-8

Band / Volume 382
Charakterisierung gradierter Eisen/Wolfram-Schichten für die erste Wand von Fusionsreaktoren
S. Heuer (2017), x, 234 pp
ISBN: 978-3-95806-252-8

Band / Volume 383
High resolution imaging and modeling of aquifer structure
N. Güting (2017), viii, 107 pp
ISBN: 978-3-95806-253-5

Band / Volume 384
IEK-3 Report 2017
Sektorkopplung –
Forschung für ein integriertes Energiesystem
(2017), 182 pp
ISBN: 978-3-95806-256-6

Band / Volume 385
Bestimmung der Wolframerosion mittels optischer Spektroskopie unter ITER-relevanten Plasmabedingungen
M. Laengner (2017), vi, 184, XI pp
ISBN: 978-3-95806-257-3

Band / Volume 386
IEK-3 Report 2017
Sector Coupling –
Research for an Integrated Energy System
(2017), 175 pp
ISBN: 978-3-95806-258-0

Band / Volume 387
Photochemistry of Highly Oxidized Multifunctional Organic Molecules: a Chamber Study
L. I. M. Pullinen (2017), II, 96, xviii pp
ISBN: 978-3-95806-260-3

Band / Volume 388
Poröse Transportschichten für die Polymerelektrolytmembran-Wasserelektrolyse
M. Höh (2017), VI, 186 pp
ISBN: 978-3-95806-262-7

Band / Volume 389
Modelling of High Temperature Polymer Electrolyte Fuel Cells
Q. Cao (2017), 173 pp
ISBN: 978-3-95806-263-4

Band / Volume 390
Potential use of nitrification inhibitors for mitigating N_2O emission from soils
D. Wu (2017), 206 pp
ISBN: 978-3-95806-264-1

Band / Volume 391
Mechanical Characterization of Solid Oxide Fuel Cells and Sealants
J. Wei (2017), II, 151 pp
ISBN: 978-3-95806-266-5

Band / Volume 392
Microcrystalline Silicon Carbide for Silicon Heterojunction Solar Cells
M. B. Pomaska (2017), 150 pp
ISBN: 978-3-95806-267-2

Weitere ***Schriften des Verlags im Forschungszentrum Jülich*** unter
http://wwwzb1.fz-juelich.de/verlagextern1/index.asp

Energie & Umwelt
Energy & Environment

392

µc-SiC:H(n) for Silicon Heterojunction Solar Cells

Manuel Bernhard Pomaska

Member of the Helmholtz Association

JÜLICH FORSCHUNGSZENTRUM

Energie & Umwelt /
Energy & Environment
Band / Volume 392
ISBN 978-3-95806-267-2

JÜLICH
FORSCHUNGSZENTRUM

Microcrystalline Silicon Carbide for Silicon Heterojunction Solar Cells

Manuel Bernhard Pomaska

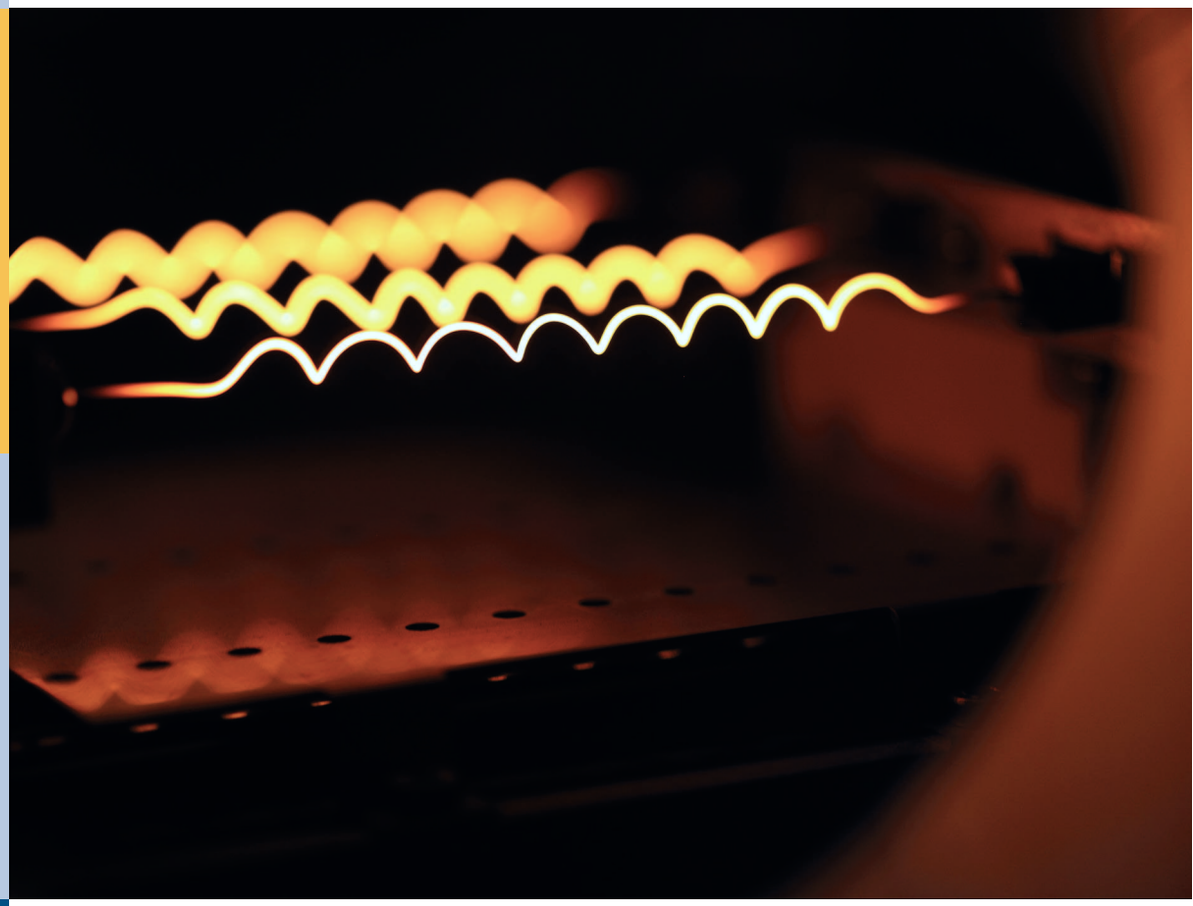

Energie & Umwelt /
Energy & Environment
Band / Volume 392
ISBN 978-3-95806-267-2

JÜLICH
FORSCHUNGSZENTRUM